Apparatus for the measurement of physical properties of cryogenic fluid mixtures

Zur Erlangung des akademischen Grades eines

DOKTORS DER INGENIEURWISSENSCHAFTEN (Dr.-Ing.)

von der KIT-Fakultät für Chemieingenieurwesen und Verfahrenstechnik
des Karlsruher Instituts für Technologie (KIT)

genehmigte

DISSERTATION

von

M. Sc. Jens Tamson

aus Essen

L'enfer, c'est les autres.
Huis clos, Jean-Paul Sartre

Abstract

Cryogenic fluid mixtures are an option to increase the efficiency of various cryogenic applications compared to operation with the few pure fluids available at low temperature. The design of these cryogenic mixed refrigerant cycles is based on the manipulation of the refrigerant properties optimised for the specific application. These properties are calculated using suitable equations of state, i.e. mostly cubic equations of state due to computational effort in the detail design of cycle components. The parameters of the equations of state are fitted to phase equilibrium, density and caloric data, which is unavailable for cryogenic fluid mixtures boiling below 50 K. This lack of data motivates the development of a new apparatus for the measurement of physical properties of cryogenic fluid mixtures. Within the scope of this work, the measurement of precise phase equilibrium data is realised with consideration of future upgrades of the test stand with measurement methods for the heat capacity and transport properties.

At first, the thermodynamic fundamentals, which are required for the calculation of phase equilibria, are laid out with a focus on the treatment of experimental data. The state of the art of equations of state is presented, showing that there are recent developments in the modeling of cryogenic fluid mixtures. Nevertheless, none of the presented equations of state is able to fully describe the fluid mixtures. In particular, the lack of caloric data impedes correct modeling.

Based on state-of-the-art methods, the concept of the cryogenic phase equilibrium test stand CryoPHAEQTS is derived. An equilibrium cell, whose temperature is set by the second stage of a pulse-tube cryocooler with compensation heating, is placed into a high-vacuum cryostat. The first stage of the cryocooler is used to cool a thermal radiation shield. The vapor phase from the equilibrium cell is re-circulated using a gas circulator at ambient temperature and led back to the cell through two tube-in-tube heat exchangers and a pre-cooler connected to the second stage of the cryocooler. Samples are taken through capillaries, which are installed at three different heights in the cell. A fourth capillary is used for differential pressure measurement to a secondary reference system. The temperature is measured by two CERNOX® sensors directly immersed into the fluid. Moreover, the test stand has optical access into the cell. It allows the operation with all non-toxic refrigerants, including oxidising or flammable substances. The operation temperature ranges from 15 K to 300 K at pressures up to 150 bar. The composition of the samples are analysed in a gas chromatograph. Typical uncertainties are ±20 mK for the temperature measurement, ±0.1 % for the pressure measurement and ±1 % for the composition analysis.

CryoPHAEQTS is commissioned by measurement of the vapor-liquid equilibrium of the well-studied argon-nitrogen system yielding excellent agreement with the respective reference equation of state. Furthermore, the vapor pressure curve of neon is investigated. The new data agrees close to the triple point, which is a fix point of the ITS-90 temperature

scale, and shows small, yet thermodynamically consistent deviations at temperatures between the triple and critical point.

First measurement data is presented for the vapor-liquid equilibrium of the neon-helium system at 32.9 K and 35.9 K. The sampling and composition analysis are identified as major error sources. The experimental methods behind the available literature data is reviewed, but the new data cannot reconcile the discrepancies between the literature data. The complete determination of the vapor-liquid equilibrium of helium-neon mixtures is beyond the scope of this work, but will be the focus of future endeavours before the implementation of the measurement methods for the heat capacity and the transport properties.

Zusammenfassung

Verglichen mit den wenigen verfügbaren Kältemitteln bei Temperaturen unter 50 K können kryogene Kältemittelgemische die Effizienz verschiedener kryogener Anwendungen erhöhen. Die Auslegung kryogener Gemischkältekreiläufe basiert auf der geschickten Mischung reiner Kältemittel zu einem Kältemittelgemisch, das sich für die Kühlanwendung optimal verhält. Die Stoffdaten dieser Kältemittelgemische werden mittels geeigneter Zustandsgleichungen berechnet. Aufgrund ihres geringen Rechenaufwands werden hauptsächlich kubische Zustandsgleichungen für die Auslegung der Kreislaufkomponenten verwendet. Die Parameter der Zustandsgleichung werden an Phasengleichgewichts-, Dichte- und kalorischen Daten angepasst. Für viele kryogene Gemische sind diese Daten jedoch nicht verfügbar. Daher wird eine neue Anlage zur Messung der Stoffeigenschaften kryogener Gemische entwickelt. Im Rahmen dieser Arbeit wird die Messung von Phasengleichgewichten umgesetzt, wobei zukünftige Ausrüstungen der Anlage mit Messmethoden für die Wärmekapazität sowie Transportgrößen eingeplant werden.

Zunächst werden die thermodynamischen Grundlagen erläutert, die für die Berechnung von Phasengleichgewichten benötigt werden. Der Fokus liegt dabei auf der Aufbereitung experimenteller Daten. Diverse Zustandsgleichungen werden eingeführt und deren Weiterentwicklungen in Hinsicht auf die Modellierung kryogener Fluidgemische wird diskutiert. Keine dieser Zustandsgleichungen ist jedoch in der Lage, alle relevanten thermodynamischen Zustandsgrößen präzise zu beschreiben. Vor Allem neue experimentelle kalorische Daten könnten zu thermodynamisch korrekten Modellen führen.

Die Konzeptionierung des kryogenen Phasengleichgewichtsprüfstands CryoPHAEQTS basiert auf einem Literaturüberblick der bisherigen Prüfstände, die unter kryogenen Bedingungen betrieben wurden. Eine Messzelle, deren Temperatur über die zweite Stufe eine Pulsrohrkleinkühlers mit Kompensationsheizung geregelt wird, ist in einem Hochvakuumbehälter aufgehangen. Die erste Stufe des Pulsrohrkleinkühlers dient zur Kühlung eines thermischen Strahlungsschilds. Die Dampfphase aus der Messzelle kann über einen Gaszirkulator, der sich außerhalb des Kryostaten befindet, zwei Rohr-in-Rohr Wärmeübertrager und eine an den Pulsrohrkleinkühler geschraubten Vorkühlblock zurück in die Flüssigphase der Messzelle geleitet werden. Über drei Kapillaren, die sich auf verschiedenen Höhen in der Messzelle befinden, werden Proben aus den jeweiligen Phasen gezogen. Eine vierte Kapillare dient der Druckmessung über die Messung der Druckdifferenz zu einem sekundären Referenzsystems. Die Temperatur wird über zwei CERNOX®-Sensoren gemessen, die sich in Dampf- und Flüssigphase in der Messzelle befinden. Zusätzlich bietet der Prüfstand einen optischen Zugang in die Messzelle. Er kann mit allen nicht-toxischen Kältemitteln, inklusive oxidierender oder hochentzündlicher Stoffe, betrieben werden. Dabei können Betriebstemperaturen von 15 K bis 300 K bei Drücken bis zu 150 bar erreicht werden. Die Zusammensetzung der Proben wird in einem Gaschromatographen analysiert.

Typische Unsicherheiten liegen bei ±20 mK für die Temperaturmessung, ±0.1 % für die Druckmessung und ±1 % für die Messung der Zusammensetzung.

Die Inbetriebnahme und Validierung von CryoPHAEQTS erfolgte mittels des sehr gut vermessen Gleichgewichts des Argon-Stickstoff Systems. Dabei konnte eine hervorragende Übereinstimmung mit der Referenzzustandsgleichung erzielt werden. Im Anschluss wird die Dampfdruckkurve von Neon untersucht. Die neuen Messdaten stimmen in der Nähe des Tripelpunkts, welcher ein Fixpunkt der ITS-90 Temperaturskala ist, überein und weichen im weiteren Verlauf leicht ab. Die Abweichungen sind jedoch thermodynamisch konsistent.

Erste Messdaten für das Phasengleichgewicht von Neon-Helium Gemisches werden bei 32.9 K und 35.9 K ermittelt. Die Probenahme und die Analyse der Zusammensetzung im Gaschromatographen werden als Hauptfehlerquellen identifiziert. Daher werden die experimentellen Methoden der beiden verfügbaren Literaturdaten verglichen; jedoch können die neuen Messdaten keinen der beiden Datensätze definitiv bestätigen oder verwerfen. Eine vollständige Messung des Phasengleichgewichts dieses Fluidgemischs ist im Rahmen dieser Arbeit nicht mehr möglich gewesen. Zusammen mit den Aufrüstungen für die Messung der Wärmekapazität und der Transportgrößen wird das Neon-Helium Gemisch in Folgeprojekten behandelt werden.

Contents

List of Figures

List of Tables

List of Symbols and Abbreviations

Greek symbols

Symbol	Description	Unit
α	α-function of cubic EoS	
α	Reduced molar Helmholtz energy	
β	Cubic quantum correction function	
β_i	Parameter in multiparameter EoS	
Γ	Stefan-Boltzmann constant	$5.67 \times 10^{-8}\,\mathrm{W\,m^{-2}\,K^{-4}}$
γ	Activity coefficient	
γ_i	Parameter in multiparameter EoS	
$\gamma_{i,\mathrm{gbs}}$	Parameter in multiparameter EoS	
Δ	Difference operator	
δ	Reduced density	
δ	Diffusion coefficient	$\mathrm{m^2\,s^{-1}}$
ϵ_i	Parameter in multiparameter EoS	
ε	Emissivity	
ε	Well depth in pair potentials	J
η	Viscosity	Pa s
η	Packing fraction	
η_i	Parameter in multiparameter EoS	
Θ	Debye-Temperature	K
θ	Parameter in multiparameter EoS	
λ	Well width in pair potentials	m
λ	Thermal conductivity	$\mathrm{W\,m^{-1}\,K^{-1}}$
$\lambda_{\mathrm{DeBroglie}}$	Thermal De Broglie wavelength	m
μ	Chemical potential	$\mathrm{J\,mol^{-1}}$
μ_{JT}	Joule-Thomson coefficient	$\mathrm{K\,Pa^{-1}}$
ν	Kinematic viscosity	$\mathrm{m^2\,s^{-1}}$
ρ	Molar density	$\mathrm{mol\,m^{-3}}$
σ	Particle size	m
τ	Reciprocal reduced temperature	
ϕ	Slope of GC calibration curve	
φ	Fugacity coefficient	
χ	Variable in temperature sensor calibration curve	
ω	Acentric factor in cubic EoS	

Latin symbols (A-M)

Symbol	Description	Unit
A	Area	m^2
A	Helmholtz energy	J
A_k	k^{th} Legendre-polynomial coefficient	
$a, \tilde{a}$	Molar and specific Helmholtz energy	J mol^{-1} and J mol^{-1}
a_i	Activity of the component i	
a_{crit}	Critical attractive parameter in cubic EoS	J mol^{-1}
B	Second virial coefficient	
b	Covolume	$\text{m}^3 \text{mol}^{-1}$
C	Third virial coefficient	
$c, \tilde{c}$	Molar and specific heat capacity	$\text{J mol}^{-1} \text{K}^{-1}$ and $\text{J kg}^{-1} \text{K}^{-1}$
$c_{\text{Péneloux}}$	Péneloux volume shift	$\text{m}^3 \text{mol}^{-1}$
D	Fourth virial coefficient	
d	Diameter	m
d_i	Parameter in multiparameter EoS	
F	Degrees of freedom	
F_{ij}	Departure function coefficient	
f	Fugacity	Pa
f	Frequency	Hz
G	Gibbs energy	J
$g, \tilde{g}$	Molar and specific Gibbs energy	J mol^{-1} and J kg^{-1}
g^{HS}	Radial distribution function	
H	Enthalpy	J
$H_{i,j}$	Henry-coefficient of solute i in solvent j	Pa
$h, \tilde{h}$	Molar and specific enthalpy	J mol^{-1} and J kg^{-1}
h	Planck's constant	$6.626 \times 10^{-34} \text{J s}$
I	Number of summation terms	
i	Loop variable	
$\dot{\jmath}$	Generic area-specific flow variable	
j	Loop variable	
K	Number of summation terms	
Kn	Knudsen number	
k	Loop variable	
k_{ij}	Binary interaction parameter	
k_{B}	Boltzmann's constant	$1.38 \times 10^{-23} \text{J K}^{-1}$
L	Length	m
L	Twu-parameter	
l_{ij}	Binary interaction parameter	
M	Twu-parameter	
$\dot{M}$	Mass flow	kg s^{-1}

Latin symbols (m-z)

Symbol	Description	Unit
m_i	Fluid-specific parameter in PR and PC-SAFT EoS	
m_k	Parameter in multiparameter EoS	
m_p	Molar mass of particle p	$\mathrm{g\,mol^{-1}}$
N	Particle number	
N	Twu-parameter	
n	Molar particle number	mol
n_i	Parameter in multiparameter EoS	
O	Generic measurand	
p	Pressure	Pa
P	Number of phases in Gibbs' phase rule	
$\dot{P}$	Power	W
$\dot{Q}$	Heat flow	W
$q, \tilde{q}$	Molar and specific heat flow	$\mathrm{J\,mol^{-1}}$ and $\mathrm{J\,kg^{-1}}$
q_i	Parameters distinguishing cubic EoS	
R	Universal gas constant	$8.314\,\mathrm{J\,mol^{-1}\,K^{-1}}$
R	Electrical and thermal resistance	Ω or $\mathrm{K\,W^{-1}}$
r	Radius	m
r_{cor}	Correlation coefficient	
$r_{\mathrm{Van\,Ness}}$	Van Ness residuals	
S	Entropy	$\mathrm{J\,K^{-1}}$
S	Dimensionless sensitivity	
$s, \tilde{s}$	Molar and specific entropy	$\mathrm{J\,mol^{-1}\,K^{-1}}$ and $\mathrm{J\,kg^{-1}\,K^{-1}}$
T	Temperature	K
t	Time	s
t_i	Parameter in multiparameter EoS	
U	Internal energy	J
$u, \tilde{u}$	Molar and specific internal energy	$\mathrm{J\,mol^{-1}}$ and $\mathrm{J\,kg^{-1}}$
$u(r)$	Pair potential	J
$u(O)$	Uncertainty of the measurand O	
V	Volume	$\mathrm{m^3}$
$v, \tilde{v}$	Molar and specific volume	$\mathrm{m^3\,mol^{-1}}$ and $\mathrm{m^3\,kg^{-1}}$
w	Velocity	$\mathrm{m\,s^{-1}}$
w_i	Weighing factor	
w_{sound}	Speed of sound	$\mathrm{m\,s^{-1}}$
X	Variable placeholder	
x	Mole fraction in the liquid phase	
y	Mole fraction in the vapor phase	
Z	Compressibility factor	
Z_{target}	Minimisation function for optimisation problems	
z	Mole fraction	

Abbreviations (A-L)

Abbreviation	Description
AAD	Average absolute deviation
AnT	Analytical isothermal method
ArbSchG	Arbeitsschutzgesetz
ArbStättV	Arbeitsstättenverordnung
ARD	Average relative deviation
ASR	Technische Regeln für Arbeitsstätten
ATEX	Regulation for potentially explosive atmospheres
AWG	American wire gauge
BImSchG	Bundes-Immisionsschutzgesetz
BetrSichV	Betriebssicherheitsverordnung
BG	Berufsgenossenschaft
BWR	Benedict-Webb-Rubin
BWRS	Benedict-Webb-Rubin EoS modified by Starling
Cap	Sampling through capillaries
CMRC	Cryogenic mixed refrigerant cycle
CryoPHAEQTS	Cryogenic phase equilibria test stand
CSvdW	vdW EoS modified with Carnahan-Starling term
DGUV	Deutsche gesetzliche Unfallversicherung
DLS	Dynamic light scattering
EoS	Equation of state
FCC	Future Circular Collider
Fr	Fredenslund consistency test
GC	Gas chromatograph(y)
GefStoffV	Gefahrstoffverordnung
GERG	Equation of state for natural gas mixtures
GUM	Guide to the expression of uncertainty in measurement
GGE	Gas-gas equilibrium
GWP	Global warming potential
HC	Hydrocarbons
HFC	(partially) fluorinated hydrocarbons
HS	Hard sphere
HT	High temperature
IDEALHY	EU project for efficient liquefaction of hydrogen
IPTS-68	International practical temperature scale of 1968
ITS-90	International temperature scale of 1990
LEL	Lower explosion limit
LHS	Left hand side
LJ	Lennard-Jones potential
LLE	Liquid-liquid equilibrium
LT	Low temperature

Abbreviations (M-Z)

Abbreviation	Description
MESG	Maximum experimental safe gap
MRC	Mixed refrigerant cycle
MS	Analysis by mass spectroscopy
NBS-55	Temperature scale of the National Bureau of Standards from 1955
NIST	National Institute of Standards and Technology
NTC	Negative temperature coefficient
ODP	Ozone depletion potential
PC-SAFT	Perturbed chain statistical association fluid theory
PE	Planck-Einstein
PFPE	Perfluoropolyether
PR	Peng-Robinson
PTC	Positive temperature coefficient
P&ID	Piping and instrumentation diagram
RDF	Radial distribution function
REFPROP	Reference fluid thermodynamic and transport properties database
RHS	Right hand side
RK	Redlich-Kister consistency test
RMS	Root mean square
RRMSE	Relative root mean square error
SAFT	Statistical association fluid theory
SAFT-VR	Statistical association fluid theory using a potential with variable range
SLE	Solid-liquid equilibrium
SRK	Soave-Redlich-Kwong
SW	Square well potential
SynNon	Synthetic non-visual method
SynVis	Synthetic visual method
TAO	Thermal acoustic oscillation
TCD	Thermal conductivity sensor/measurement
tc-PR	Translated consistent Peng Robinson
TDMS	Technical data management streaming file
TRBS	Technische Regeln für Betriebssicherheit
TRGS	Technische Regeln für Gefahrstoffe
TRLV	Technische Regeln zur Lärm- und Vibrations-Arbeitsschutzverordnung
UEL	Upper explosion limit
Val	Sampling using a special valve
Vcir	Vapor phase re-circulation
vdW	van der Waals
VLE	Vapor-liquid equilibrium
VLLE	Vapor-liquid-liquid equilibrium
VN	Van Ness consistency test

Subscripts

Subscript	Description
0	Pure component reference state
+	Arbitrary reference state
*	Unsymmetrical notation
∞	Infinite dilution
abs	Absolute
amb	Ambient
assoc	Association
att	Attractive
c	Critical
calc	Calculated
chain	Chain formation
char	Characteristic
class	Classical
crit	Critical
dil	Infinite dilution reference state
disp	Dispersion
E	Excess
eff	Effective
exp	Experimental
HS	Hard sphere
id	Ideal
irr	Irreversible
JT	Joule-Thomson
L	Liquid phase
LJ	Lennard-Jones potential
M	Mixture
Mie	Variable Mie-potential
mix	Mixture parameter
p	At constant pressure
r	Reduced
ref	Reference
rel	Relative
rep	Repulsive
res	Residual
rot	Rotational
sat	At saturation
SW	Square-well potential

Subscript	Description
th	Thermal
trans	Translational
trip	Triple point
v	At constant volume
vib	Vibrational

1. Introduction

Cryogenics is a key technology towards a sustainable economy as low temperatures are required for transport and storage of liquid hydrogen and for superconducting applications, such as electric motors with high power-densities or lossless power cables. In state-of-the-art cryogenic refrigerators, cooling power is offered by the evaporation of a pure refrigerant at constant cooling temperature. Depending on the required cooling power and temperature, the refrigeration systems are designed with high technical complexity using cascades, several heat exchangers, cold expanders, phase separators and additional pre-cooling in order to increase efficiency. For example, the recent hydrogen liquefier of Linde in Leuna is a modified Claude cycle using hydrogen as refrigerant, three turbines, eight main heat exchangers and liquid nitrogen for pre-cooling [1]. All these unit operations aim at reducing the entropy production introduced by compression, expansion, heat transfer and liquefaction. This technical complexity is feasible for large-scale plants only, as the capital expenditures exceed the benefits, that a thermodynamically efficient system has on the operational expenditures. An efficient and scalable refrigeration system must rely on a simple cycle with few components. Instead of adjusting the cycle to the properties of the refrigerant, the properties of the refrigerant itself can be manipulated by adding fluids to form a refrigerant mixture. Cycles which are operated in this manner are called mixed refrigerant cycles (MRC).

1.1. Mixed refrigerant cycles

The use of refrigerant mixtures at temperatures around $100\,\mathrm{K}$ is the state of the art in natural gas liquefaction [2]. Mixed refrigerant cycles are based on the Linde-Hampson cycle shown in Figure 1.1. The energy demand $\dot{P}$ of such a refrigeration cycle is related to the total specific entropy production $\tilde{s}_{\mathrm{irr,tot}}$ through the ambient temperature T_{amb} and the mass flow $\dot{M}$

$$\dot{P} = \dot{M} T_{\mathrm{amb}} \tilde{s}_{\mathrm{irr,tot}} = T_{\mathrm{amb}} \sum_i \dot{M}_i \tilde{s}_{\mathrm{irr},i}, \tag{1.1}$$

with $\dot{M}_i$ being the mass flow and $\tilde{s}_{\mathrm{irr},i}$ being the entropy production of process step i, respectively. Entropy is produced by any gradient in the system, i.e. pressure gradients in the compressor and the throttle, pressure drop in the cycle, temperature gradients in the heat exchangers and gradients of the chemical potential during phase changes. The entropy production induced by gradients of the chemical potential is independent of temperature, but the other two mechanisms depend on the absolute temperature of

1

the individual process part. The entropy production by pressure change scales with the inverse temperature through

$$\mathrm{d}\tilde{s}_{\text{irr, pressure}} = -\frac{\tilde{v}}{T}\mathrm{d}p, \tag{1.2}$$

with $\tilde{v}$ being the specific volume and p being the pressure. The entropy production by heat exchange scales with the temperature difference between the low- and high-pressure stream as well as with the product of the inversed absolute temperatures

$$\mathrm{d}\tilde{s}_{\text{irr, heat}} = \frac{T_{\text{high}} - T_{\text{low}}}{T_{\text{high}}T_{\text{low}}}\mathrm{d}\tilde{q}, \tag{1.3}$$

with $\tilde{q}$ being the specific heat transferred along the heat exchanger. Hence, low temperature gradients $T_{\text{high}} - T_{\text{low}}$ are of particular interest at cryogenic temperatures on the cold side of the internal heat exchanger. Figure 1.2 compares qualitative temperature profiles in the internal heat exchanger for a Linde-Hampson cycle operated with a pure refrigerant against operation with a refrigerant mixture. As shown in Figure 1.2a, the temperature difference of the high pressure stream in the heat exchanger is smaller than the temperature difference of the low pressure stream. Depending on which stream has a higher heat capacity, the minimal temperature difference between the two streams is located at the warm or the cold end of the heat exchanger. As the heat capacity of gases increases with pressure, the largest temperature gradient between the streams is located at the cold end of the internal heat exchanger, where it produces the most entropy. Figure 1.2b shows a qualitative temperature profile with an ideal refrigerant mixture, where the high and low pressure streams have similar heat capacities. Thereby, a nearly constant temperature gradient, which minimises entropy production, is obtained. Therefore, the heat capacity represents one of the main design parameters for the optimisation of an MRC.

A typical refrigerant mixture consists of 3–6 refrigerants, whose compositions are adjusted to yield a mixture with optimal properties for the particular application [3, 4]. Thermodynamic efficiency aside, these properties include thermodynamic state, thermal, caloric and transport properties, flammability, global warming potential (GWP), ozone depletion potential (ODP), toxicity as well as market availability and cost. For liquefaction of natural gas, nitrogen-hydrocarbon mixtures are used. Also, synthetic refrigerant mixtures (i.e. (partly)-fluorinated hydrocarbons) have been proposed to avoid safety issues due to the flammability of hydrocarbons [5, 6]. Their high GWP is a major drawback. Current legislation in the European Union allows the use of high-GWP refrigerants for low temperature applications, but it is likely that their application is further restricted [7]. Therefore, research focuses on low-GWP refrigerant mixtures. Several researchers have suggested to add the cryogens helium, hydrogen and neon to the nitrogen-hydrocarbon mixtures to decrease the cooling temperature below 77 K [8, 9, 10, 11, 12], i.e. the normal boiling point of nitrogen . The effects of cryogens addition on the cooling temperature are either determined on laboratory-scale test-benches, or by simulation using thermodynamic models. These models require an accurate predictive capability for the required physical properties, as experimental data is not widely available for mixtures containing more than
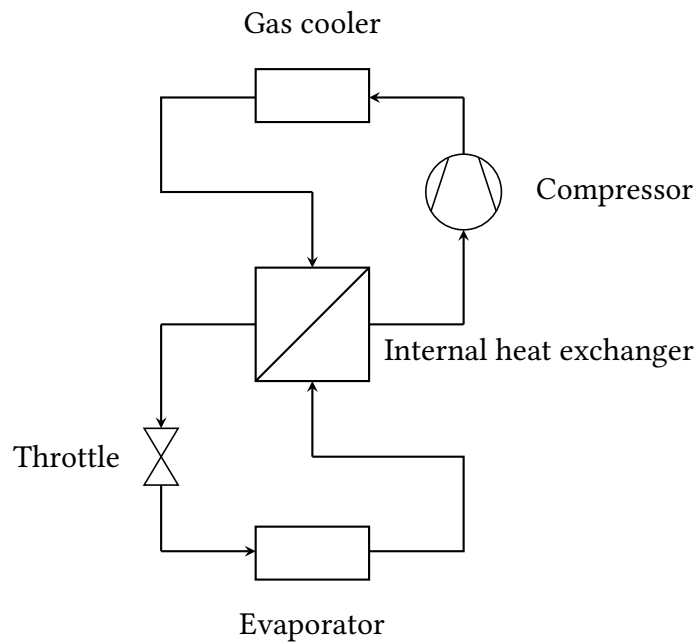
Figure 1.1.: Schematics of the Linde-Hampson cycle as cryocooler.

(a) Operation with a pure refrigerant.

(b) Operation with an optimal refrigerant mixture.
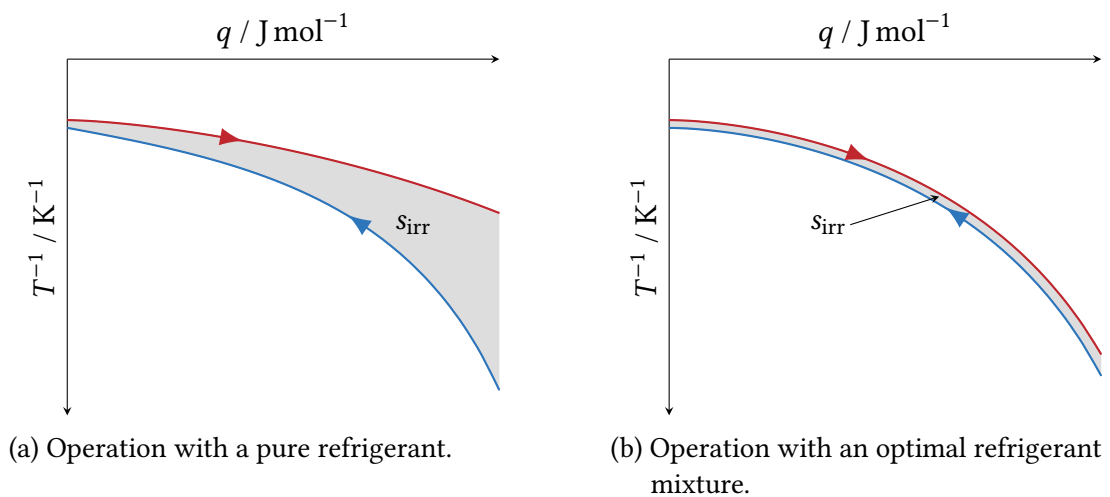
Figure 1.2.: Qualitative temperature profiles in the counter flow heat exchanger of a Linde-Hampson cycle. The red curve represents the high pressure stream and the blue curve the low pressure stream. The gray areas represent the respective entropy productions.

3 components. Due to the enormous amount of degrees of freedom for multi-component mixtures, the experimental data base is incomplete, requiring advanced predictive models.

Cryogenic mixed refrigerants cycles (CMRC) operating at cooling temperatures below 50 K are proposed to increase the efficiency of current hydrogen liquefaction plants [8, 12]. In this temperature range, the only refrigerant candidates are helium, hydrogen and neon as all other substances are below their triple points. Particularly, neon-helium mixtures have been suggested, e.g. in the EU project IDEALHY, aiming at doubling the efficiency of current plants [8]. In this project, the use of neon-helium mixtures as cooling agent accounts for more than 20 % of the envisioned reduction of operational expenditures. The neon-helium system has also been proposed in refrigerators for super-conducting applications in the Future Circular Collidor (FCC) at CERN [9, 10, 11]. Unfortunately, neither caloric nor transport properties have been measured for this system in the temperature range of interest. The available phase equilibria measurements [13, 14] are inconsistent with each other [15]. Therefore, the community requests such property measurements in the cryogenic domain [12, 16, 17].

In conclusion, there is a lack of physical property data of binary and ternary systems in the cryogenic domain below 50 K as well as for multi-component refrigerant mixtures requiring new experimental efforts.

1.2. Objective

This work aims at providing precise physical property data for refrigerant mixtures in the range of technical interest, i.e. at temperatures from 14 K to 300 K and pressures from 0 MPa to 15 MPa. The test bench to be developed has two goals:

- Property data measurement of multi-component mixtures above 77 K. Based on a prior mixture optimisation, the predictive performance of existing equations of state (EoS) can be evaluated by measurement of selected state points of interest, i.e. azeotropy, formation of liquid-liquid equilibria, probable points of operation.
- Property data measurement of binary and ternary mixtures below 77 K. Since the experimental data base at cryogenic conditions is scarce even for binary and ternary fluid mixtures, these systems can be investigated comprehensively.

The process design of refrigeration systems requires thermal properties, such as vapor pressure and density, caloric properties, such as heat capacity, and transport properties, such as thermal conductivity and viscosity. The test bench shall allow the determination of all three property types. In this work, the measurement of phase equilibria is achieved while making provisions for the measurement of caloric and transport properties. The phase equilibria test stand shall provide precise property data with envisioned uncertainties of ±50 mK for temperature, ±0.1 % for pressure and ±1 % for composition. As phase equilibria types might be unknown for some systems, vapor-liquid equilibria (VLE) as well as vapor-liquid-liquid equilibria (VLLE) shall be measureable. Operation with flammable substances must be possible, including hydrogen.

The thesis is structured as follows: First, the thermodynamic fundamentals regarding the modeling of physical property data are laid out in chapter 2 with a focus on the handling

of experimental phase equilibrium data. Different thermodynamic models are discussed concerning their suitability, complexity and accuracy with regard to fluid systems boiling below 50 K. Chapter 3 deals with state-of-the-art experimental methods, available for the measurement of physical properties at low temperatures. The test stand, which has been conceptualised, designed, constructed and commissioned within the framework of this thesis, is described in detail in chapter 4. Additional optimisations to the test stand have been derived from the commissioning results. They are discussed together with the first experimental results for neon and the neon-helium system in chapter 5. Finally, the work is summarised and an outlook is given in chapter 6.

2. Thermodynamics of fluid properties

An equation containing all information about a system in thermodynamic equilibrium is called thermodynamic potential. Thermodynamic potentials can be derived from the fundamental equation $U(S, V, N)$ by Legendre-transformation, where U is the internal energy, S the entropy, V the volume and N the number of particles. Convenient potentials are the Helmholtz energy $A(T, V, N)$ and the Gibbs energy $G(T, p, N)$, where p denotes the pressure and T the temperature, because they depend on measureable state variables. In phase equilibrium, the state variables are not independent but follow Gibbs' phase rule

$$F = K - P + 2, \tag{2.1}$$

where F is the number of degrees of freedom, K the number of components and P the number of coexisting phases. However, neither the Helmholtz energy nor the Gibbs energy are accessible through measurement. Therefore, models are needed, which connect experimentally observable state variables with the inaccessible ones. Such models enable calculation of all state variables by integration or differentiation. For the formulation of the Gibbs' energy of a pure substance $G(p, T)$ either the thermal equation of state $\tilde{v}(T, p)$ and one isobar of the caloric equation of state $\tilde{h}(p, T)$

$$\tilde{g}(p, T) = \frac{T}{T_0}\tilde{g}_0 + \int_{p_0}^{p} \tilde{v}(p, T)\, \mathrm{d}p - T \int_{T_0}^{T} \tilde{h}(p_0, T)\, \frac{\mathrm{d}T}{T^2} \tag{2.2}$$

or the caloric equation of state and one isotherm of the thermal equation of state is required

$$\tilde{g}(p, T) = \frac{T}{T_0}\tilde{g}_0 + \frac{T}{T_0}\int_{p_0}^{p} \tilde{v}(p, T_0)\, \mathrm{d}p - T \int_{T_0}^{T} \tilde{h}(p, T)\, \frac{\mathrm{d}T}{T^2}, \tag{2.3}$$

where $\tilde{g}$ is the specific Gibbs energy, $\tilde{v}$ the specific volume, $\tilde{h}$ the specific enthalpy and the index 0 denotes a reference state. In any case, a complete description of the thermodynamic behaviour by a thermodynamic potential requires thermal and caloric measurements. Usually, parameters of a thermal equation of state are fitted to phase equilibrium, saturated density and p, v, T-data, while the temperature-dependent isobaric heat capacity of the ideal gas is fitted to spectroscopic data [18]. The translational, rotational and vibrational degrees of freedom F of a molecule are a good estimate for the heat capacity in the high-temperature limit, i.e. the ideal gas reference state

$$c_v = \frac{F}{2}R. \tag{2.4}$$

In principle, arbitrary reference states can be chosen. For properties at cryogenic temperatures, the high-temperature limit is far away, considering the logarithmic nature of the thermodynamic temperature. Therefore, it would be desirable to define a reference state at very low temperatures, e.g. $T = 0\,\text{K}$. The Debye theory of phonon excitation is an approach to incorporate effects far from the ideal state into the model equations [19]. It is based on the treatment of liquids as lattices with variable density and it is the only theoretical background to model the cubic dependence of the heat capacity on temperature at cryogenic conditions. It builds on the interactions of a solid rather than introducing force fields to the ideal gas. A first effort has been made for helium-3, but the EoS is still not rigorous enough nor applicable to other fluids. Therefore, modern thermodynamic models still rely on modifications and perturbations of an ideal gas (mixture).

2.1. Thermodynamics of phase equilibria

A system of K components i separated into P phases is in thermodynamic equilibrium if all temperatures T, pressures p and chemical potentials μ_i among all phases are equal:

$$T' = T'' = \dots \tag{2.5}$$

$$p' = p'' = \dots \tag{2.6}$$

$$\mu_i' = \mu_i'' = \dots, \qquad\qquad\qquad i = 1 \dots K \tag{2.7}$$

Temperature and pressure are directly available through measurement; the chemical potential of a component in a mixture is calculated through

$$\mu_i\left(p, T, x_1 \dots x_{K-1}\right) = \mu_{0i}\left(p^+, T\right) + RT \ln \frac{f_i}{p^+}, \tag{2.8}$$

where the index 0 denotes the pure component, the index + an arbitrary reference state, R the universal gas constant and f_i the fugacity of the component in the mixture. Using Equation 2.8, Equation 2.7 is expressed as the isofugacity criterion:

$$f_i' = f_i'' = \dots \tag{2.9}$$

There are two ways to relate the fugacity to measureable compositions, i.e the mole fractions z_i. The φ-φ-method corrects the partial pressure p_i of the component in the mixture with a fugacity coefficient φ_i:

$$f_i = \varphi_i p_i = \varphi_i z_i p \tag{2.10}$$

Fugacity coefficients are available through EoS. Usually, vapor phases are well represented by Equation 2.10. Due to their higher densities, liquid phases may exhibit behaviour requiring more complex corrections to the ideal mixture, which is called activity

$$a_i = \frac{f_i^{\text{L}}}{f_{0i}^{\text{L}}} = \gamma_i x_i, \tag{2.11}$$

where the index L denotes the liquid phase and x_i the mole fraction of component i in the liquid phase. The activity coefficient γ_i is a function of temperature, pressure and composition. While the vapor phase fugacity is still expressed by Equation 2.10, the fugacity of component i in an ideal mixture of real liquids $f_i^{\mathrm{L,ideal}}$ is corrected with the activity coefficient γ_i

$$f_i^{\mathrm{V}} = \varphi_i^{\mathrm{V}} y_i p \tag{2.12}$$

$$f_i^{\mathrm{L}} = \gamma_i \underbrace{x_i f_{0i}^{\mathrm{L}}}_{f_i^{\mathrm{L,ideal}}} \tag{2.13}$$

where the index V denotes the vapor phase and y the vapor phase mole fraction. The activity coefficient is a strong function of temperature and composition, while its pressure-dependence can usually be neglected at low to moderate pressures. The fugacity of a pure liquid equals the fugacity of the vapor at saturation conditions. This fact is used to express the liquid fugacity in terms of the fugacity coefficient and pressure at saturation. For higher pressures, it is corrected by the Poynting correction factor:

$$f_{0i}^{\mathrm{L}} = \varphi_{0i}^{\mathrm{sat}} \cdot p_{0i}^{\mathrm{sat}} \cdot \underbrace{\exp\left(\int_{p_{0i}^{\mathrm{sat}}}^{p} \frac{v_{0i}^{\mathrm{L}}}{RT} \mathrm{d}p\right)}_{\text{Poynting correction}}, \tag{2.14}$$

where v_{0i}^{L} denotes the molar volume of the pure liquid i. Finally, the γ-φ-method is given by:

$$\varphi_i^{\mathrm{V}} \cdot y_i \cdot p = \gamma_i \cdot x_i \cdot \varphi_{0i}^{\mathrm{sat}} \cdot p_{0i}^{\mathrm{sat}} \cdot \exp\left(\int_{p_{0i}^{\mathrm{sat}}}^{p} \frac{v_{0i}^{\mathrm{L}}}{RT} \mathrm{d}p\right). \tag{2.15}$$

Activity coefficients can be derived from so-called g^{E}-models, where the index E denotes the excess of the Gibbs energy g from the ideal mixture $\Delta g_{\mathrm{M}}^{\mathrm{id}}$:

$$\Delta g_{\mathrm{M}} = g^{\mathrm{E}} + \underbrace{RT \sum_{i=1}^{K} x_i \ln x_i}_{\Delta g_{\mathrm{M}}^{\mathrm{id}}} \tag{2.16}$$

The excess Gibbs energy is linked to the activity coefficients through:

$$g^{\mathrm{E}} = \sum_{i=1}^{K} x_i \mu_i^{\mathrm{E}} = RT \sum_{i=1}^{K} x_i \ln \gamma_i \tag{2.17}$$

$$\left(\frac{\partial g^{\mathrm{E}}}{\partial x_i}\right)_{p,T,x_{j\neq i}} = RT \ln \gamma_i \tag{2.18}$$

EoS which are based on thermodynamic potentials allow direct calculations of the chemical potentials through derivation. The isofugacity criterion is beneficial, if pressure-explicit EoS, such as cubic EoS or the Virial equation, are used, since they provide simple analytical expressions for the fugacity coefficients. Systems with highly non-ideal behaviour of the liquid phase require modeling by the γ-φ-method and a suitable g^{E}-model.

For solute-solvent systems or mixtures with at least one super-critical component, the saturation properties in the liquid standard state used in Equation 2.14 are ill-defined. Instead of the pure real liquid, the infinite dilution of the super-critical component in the sub-critical component(s) serves as reference state:

$$f_{0i}^{\mathrm{L,dil}} = H_{i,j}\left(T, p^+\right) \exp\left(\int_{p^+}^{p} \frac{v_i^\infty}{RT} \mathrm{d}p\right),\tag{2.19}$$

with $H_{i,j}\left(T, p^+\right)$ being the Henry coefficient of component i in solvent j at reference pressure p^+ and v_i^∞ the partial molar volume of the solution at infinite dilution.

The fugacity of the super-critical component in the real mixture can be determined similar to Equation 2.13 by

$$f_i^{\mathrm{L,dil}} = x_i \gamma_i^* f_{0i}^{\mathrm{L,dil}},\tag{2.20}$$

where the asterisk denotes the different asymptotic behaviours of the activity coefficients resulting from this change of reference:

$$\lim_{x_i \to 0} \gamma_i = \gamma_i^\infty, \qquad\qquad \text{for pure component reference state,}\tag{2.21}$$

$$\lim_{x_i \to 0} \gamma_i^* = 1, \qquad\qquad \text{for infinite dilution reference state.}\tag{2.22}$$

The value of γ_i^* can be obtained by a parallel shift of γ_i^∞ in γ_i

$$\ln \gamma_i^* = \ln \gamma_i - \ln \gamma_i^\infty \qquad\qquad \text{or equivalently}\tag{2.23}$$

$$\gamma_i^* = \frac{\gamma_i}{\gamma_i^\infty},\tag{2.24}$$

where γ_i^∞ denotes the activity coefficient at infinite dilution. The use of different reference states when applying the γ-φ approach is called the unsymmetrical normalisation. This convention affects the calculation of the excess Gibbs energy

$$\frac{g^{\mathrm{E}}}{RT} = \underbrace{\sum x_i \ln \gamma_i^*}_{\text{super-critical}} + \underbrace{\sum x_j \ln \gamma_j}_{\text{sub-critical}}.\tag{2.25}$$

The γ-φ method with infinite dilution as reference state yields

$$\varphi_i^{\mathrm{V}} \cdot y_i \cdot p = \gamma_i^* \cdot x_i \cdot \underbrace{H_{i,j}\left(T, p^+\right) \cdot \exp\left(\int_{p^+}^{p} \frac{v_i^\infty}{RT}\mathrm{d}p\right)}_{H_{i,j}(T,p)}.\tag{2.26}$$

It should be noted that the Henry coefficient $H_{i,j}(T,p)$ asymptotically equals Henry's constant $H_{i,j}^\infty(T)$ in the infinite dilution limit:

$$\lim_{x_i \to 0} \frac{\varphi_i^V \cdot y_i \cdot p}{x_i} = \lim_{x_i \to 0} \gamma_i^* H_{i,j}(T,p) = H_{i,j}^\infty(T). \tag{2.27}$$

Equation 2.27 yields Henry's law

$$p_i = H_{i,j}^\infty x_i \tag{2.28}$$

assuming an ideal vapor phase.

2.2. Thermodynamic consistency at low pressure

The Gibbs-Duhem equation expressed with excess state variables is given by:

$$s^E dT - v^E dp + \sum_{i=1}^{K} x_i d\mu_i^E = 0. \tag{2.29}$$

For a binary vapor-liquid-equilibrium, Equation 2.29 simplifies to:

$$x_1 d(\ln \gamma_1) + x_2 d(\ln \gamma_2) = \underbrace{\frac{v^E}{RT} dp}_{=0,\text{ if isobaric}} - \underbrace{\frac{h^E}{RT^2} dT}_{=0,\text{ if isothermal}}. \tag{2.30}$$

Equation 2.30 shows that the activity coefficients are not independent from one another; hence, it removes a degree of freedom for the set of $\{T, p, x, y\}$. Having measured temperature, pressure and liquid phase compositions, Equation 2.30 combined with Equation 2.15 enables calculation of the vapor phase composition. If the vapor phase composition has been measured redundantly, the data set can be checked for thermodynamic consistency, since activity coefficients directly calculated from experimental data must obey the Gibbs-Duhem equation. The term *experimental activity coefficient* is misleading, since its calculation is based on assumptions, such as an ideal vapor phase or a negligible Poynting correction

$$\gamma_i^{exp} = \frac{y_i^{exp} \varphi_i^V p^{exp}}{x_i^{exp} p_{0i}^{sat} \varphi_{0i}^{sat} \exp\left(\int_{p_{0i}^{sat}}^{p} \frac{V_{0i}^L}{RT} dp\right)} \approx \frac{y_i^{exp} p^{exp}}{x_i^{exp} p_{0i}^{sat}}. \tag{2.31}$$

Even when considering real vapor phases, model assumptions affect the fugacity coefficient calculations, perturbing the experimental nature of the activity coefficient. *Calculated activity coefficients* are meant, if calculated by appropriate g^E-models without knowledge about the vapor phase behaviour.

The consideration of the right-hand-side (RHS) of Equation 2.30 depends on the data set. For isothermal data, the excess volume must be determined, although it is usually

negligible at low to moderate pressures and chemically similar mixture components. Isobaric data requires the excess enthalpy of the mixture, which can only be neglected for athermal mixtures. Generally, this fact favors experiments under isothermal rather than isobaric conditions. Furthermore, the fitting of parameters of g^{E}-models and the calculation of pure component vapor pressures is facilitated for isothermal data, since the temperature-dependence of the parameters does not have to be considered.

Based on Equation 2.29 many consistency tests have been developed [20]. They can be classified into area tests, which check for integral compliance with the Gibbs-Duhem equation, and point-to-point tests checking for differential compliance, i.e. the non-integrated from of the Gibbs-Duhem equation. Other tests check for compliance of the data with intrinsically consistent g^{E}-models. The latter test results are affected by the suitability of the selected model. Bad results can be caused by both, inappropriate models and data inconsistencies. On the contrary, good results clearly indicate consistent data. In the following, common consistency tests are described.

Area tests have been developed simultaneously by Redlich and Kister [21] and Herington [22]. Further on, an area test is referred to as Redlich-Kister test. It is based on the total differential of the excess Gibbs energy

$$dg^{\mathrm{E}} = \left(\frac{\partial g^{\mathrm{E}}}{\partial T}\right)_{p,x} dT + \left(\frac{\partial g^{\mathrm{E}}}{\partial p}\right)_{T,x} dp + \sum_{i=1}^{K} \left(\frac{\partial g^{\mathrm{E}}}{\partial x_i}\right)_{p,T,x_{j\neq i}} dx_i \tag{2.32}$$

yielding

$$\frac{dg^{\mathrm{E}}}{RT} = \frac{v^{\mathrm{E}}}{RT} dp + \ln\frac{\gamma_1}{\gamma_2} dx_1 \tag{2.33}$$

for an isothermal binary system. In case of a vapor-liquid-equilibrium, the excess volume at saturation is not well-defined. Therefore, it is estimated at a higher pressure, where both components are in a sub-cooled state. Then, the orders of magnitude of the integrals

$$\int_{p(x_1=1)}^{p(x_1=0)} \frac{v^{\mathrm{E}}}{RT} dp = \int_{x_1=0}^{x_1=1} \ln\frac{\gamma_1}{\gamma_2} dx_1 \tag{2.34}$$

have to be assessed to decide whether the left-hand-side (LHS) of Equation 2.34 is negligible. At low to moderate pressures, this is usually the case. The integral on the RHS is evaluated through Equation 2.31. The Redlich-Kister test is passed if the following criterion is met:

$$100 \cdot \frac{\left|\int_{x_1=0}^{x_1=1} \ln\frac{\gamma_1}{\gamma_2} dx_1\right|}{\int_{x_1=0}^{x_1=1} \left|\ln\frac{\gamma_1}{\gamma_2}\right| dx_1} \leqslant 2, \tag{2.35}$$
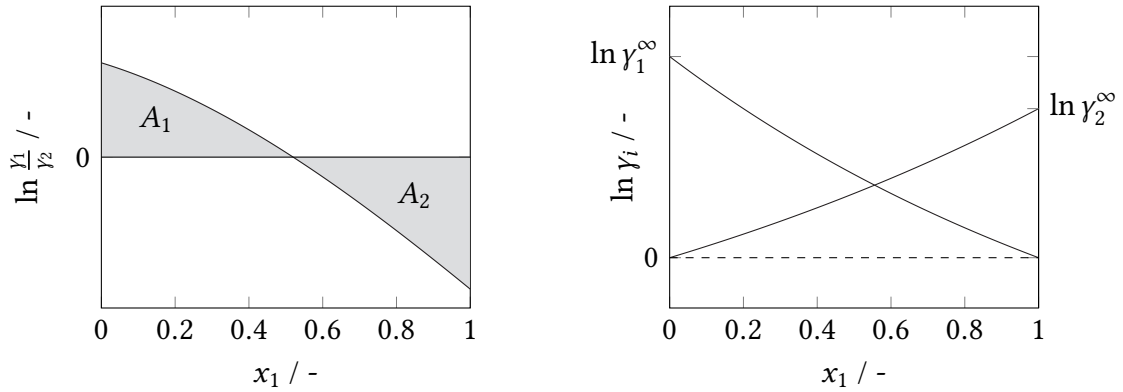
(a) Generic Redlich-Kister plot defining the areas above (A_1) and below (A_2) the horizontal axis.

(b) Generic plot of experimental activity coefficients indicating correct asymptotic behaviour and corresponding slopes. The dashed line represents the state of an ideal mixture with $\ln \gamma_i = 0$.

Figure 2.1.: Illustrations of the test criteria for an area test and a visual, model-independent point-to-point test.

with 2 being an empirical threshold. The expression in Equation 2.35 corresponds to the relative difference of the areas below and above the horizontal axis

$$\frac{\left| \int_{x_1=0}^{x_1=1} \ln \frac{\gamma_1}{\gamma_2} \mathrm{d}x_1 \right|}{\int_{x_1=0}^{x_1=1} \left| \ln \frac{\gamma_1}{\gamma_2} \right| \mathrm{d}x_1} = \frac{|A_1 + A_2|}{|A_1| + |A_2|}, \tag{2.36}$$

with A_1, A_2 being defined in Figure 2.1a. This method requires an appropriate EoS to calculate fugacity coefficients and the Poynting correction, instead of a g^{E}-model. Furthermore, experimental data points need to be interpolated in order to evaluate the integrals.

Integral compliance is a necessary but not sufficient consistency criterion. Equally large errors with different sign may cancel out. Looking at the ratio of the activity coefficients

$$\frac{\gamma_1}{\gamma_2} \approx \frac{y_1 x_2 \varphi_1^{\mathrm{V}} \varphi_2^{\mathrm{sat}} p_2^{\mathrm{sat}}}{y_2 x_1 \varphi_2^{\mathrm{V}} \varphi_1^{\mathrm{sat}} p_1^{\mathrm{sat}}}, \tag{2.37}$$

the measurement of the total pressure only affects the fugacity coefficients [23]. In principle, Equation 2.37 could be evaluated at arbitrary pressures and still yield consistent results. Therefore, Van Ness et al. have developed a point-to-point test, which looks at the residuals $\Delta \ln \frac{\gamma_1}{\gamma_2}$ [23]. By differentiation of Equation 2.17, they obtained

$$\Delta \ln \frac{\gamma_1}{\gamma_2} = x_1 \frac{\mathrm{d} \ln \gamma_1}{\mathrm{d}x_1} + x_2 \frac{\mathrm{d} \ln \gamma_2}{\mathrm{d}x_1} - \frac{v^{\mathrm{E}}}{RT} \frac{\mathrm{d}p}{\mathrm{d}x_1}, \tag{2.38}$$

which is valid for a binary VLE at constant temperature. For fully consistent data, the LHS of Equation 2.38 is always zero as stated by the Gibbs-Duhem equation. For negligible

excess volumes, Equation 2.38 implies a minimum of $\gamma_2(x_1)$ where $\gamma_1(x_1)$ has maximum and vice-versa. Moreover, at high dilutions $x_1 \to 0$, $\gamma_2(x_1)$ should smoothly approach unity. In the derivatives of the experimental activity coefficients, the total pressure does not cancel out. To evaluate the residuals for each data point, the derivatives of the experimental activity coefficients with respect to composition must be calculated by interpolation of the data. Exact calculation of the derivatives requires many data points with small steps in composition. This experimental effort is not justified. After all, a plot of the activity coefficients as shown in Figure 2.1b provides a visual test for the symmetric and asymptotic behaviour.

To overcome the interpolation issue, Van Ness [24] and Fredenslund et al. [25] proposed the use of inherently consistent g^E-models. This way, the data is not directly tested for consistency, nevertheless the compliance with one or more consistent models is tested. Therefore, this method can deliver a statement about the consistency of the data, even though failed test results might also be due to an inappropriate model. The relations

$$RT \ln \gamma_1 = g^E + x_2 \frac{dg^E}{dx_1} - x_2 v^E \frac{dp}{dx_1} \approx g^E + x_2 \frac{dg^E}{dx_1} \tag{2.39}$$

$$RT \ln \gamma_2 = g^E - x_1 \frac{dg^E}{dx_1} + x_1 v^E \frac{dp}{dx_1} \approx g^E - x_1 \frac{dg^E}{dx_1} \tag{2.40}$$

are used to incorporate the g^E-model parameters into the VLE calculations

$$p = \sum_{i=1}^{K} x_i \gamma_i p_{0i}^{\text{sat}} \frac{\varphi_{0i}^{\text{sat}}}{\varphi_i^V} \exp \left(\int_{p_{0i}^{\text{sat}}}^{p} \frac{v_{0i}^L}{RT} dp \right), \tag{2.41}$$

$$y_i = x_i \gamma_i \frac{p_{0i}^{\text{sat}}}{p} \frac{\varphi_{0i}^{\text{sat}}}{\varphi_i^V} \exp \left(\int_{p_{0i}^{\text{sat}}}^{p} \frac{v_{0i}^L}{RT} dp \right). \tag{2.42}$$

Correlations for the fugacity coefficients of the vapor phase and for the pure liquid volumes are required, e.g. by means of an EoS. Due to the dependency of the fugacity coefficient φ_i^V on the vapor phase composition, the VLE calculations are iterative. The fitting procedure aims at a least-squares optimisation of the bubble-point pressure

$$\min \sum_i \left(p_i^{\text{exp}} - p_i^{\text{calc}} \right)^2. \tag{2.43}$$

Several quantities, such as g^E, y_i, p and $\ln \frac{\gamma_1}{\gamma_2}$, have been proposed as arguments for the evaluation of the residuals

$$\Delta Z_i^{\text{res}} = Z_i^{\text{exp}} - Z_i^{\text{calc}} \tag{2.44}$$

as well as the root mean square (*RMS*) or the absolute average deviation (*AAD*)

$$RMS = \sqrt{\frac{1}{N}\sum_i^N \left(\Delta Z_i^{\mathrm{res}}\right)^2},$$ (2.45)

$$AAD = \frac{1}{N}\sum_i^N \left\|\Delta Z_i^{\mathrm{res}}\right\|.$$ (2.46)

The pure component vapor pressures $p_{0i}^{\mathrm{sat}}(T)$ must be dealt with caution. If the date points have been measured in the same experimental run, they are associated with the same random error induced by pressure measurement uncertainty as all other points $p(T, x_i)$. However, once measured, this random error adds a constant bias to all other data points due to Equation 2.31. To remove this bias, Abott et al. [26] have proposed a two-step procedure: First, the experimental values are used to determine the experimental activity coefficients and to fit the parameters of the g^{E}-model. This way, the general suitability of the g^{E}-model to describe the data within its uncertainty is checked. Then, the previously fixed parameter p_{0i}^{sat} is used as additional variable to regress all experimental data including its experimental value by the constraint

$$\lim_{x_i \to 0} p(T, x_i) = p_{0i}^{\mathrm{sat}}(T) \pm u_{p_{0i}}.$$ (2.47)

If the suitability of the g^{E}-model was not checked beforehand, the pure vapor pressure might act as primary fitting parameter for mixture behaviour instead of the actual mixture model parameters.

Fredenslund et al. [25] proposed to use the following Legendre-polynomial

$$\frac{g^{\mathrm{E}}}{RT} = x_1(1 - x_1) \sum A_k L_k(x_1)$$ (2.48)

where A_k are the parameters to be fitted and L_k the kth Legendre-polynomials. This generic g^{E}-model offers flexibility and can be truncated as soon as the data is sufficiently represented. It is stipulated that an order of 3 to 4 gives a good fit for most systems. The *AAD* of the vapor phase compositions may not exceed the threshold of 0.01 to pass the Fredenslund test. This threshold is a typical value for the sum of vapor and liquid composition uncertainties.

Van Ness et al. [24] have proposed an evaluation of the residuals

$$\Delta \gamma_i^{\mathrm{res}} = \ln \frac{\gamma_{1,i}^{\mathrm{calc}}}{\gamma_{2,i}^{\mathrm{calc}}} - \ln \frac{\gamma_{1,i}^{\mathrm{exp}}}{\gamma_{2,i}^{\mathrm{exp}}}.$$ (2.49)

Both, the *RMS* and a look at the individual data point residuals are required to judge the consistency. To give the test result a more quantitative nature instead of a binary consistent/inconsistent judgement, Van Ness et al. assign a qualitative index between 1 and 10 to the *RMS*. The values and their meaning are listed in Table 2.1. For both tests,

Table 2.1.: Consistency index classification for VLE data according to Van Ness [24].

Index	RMS of $\Delta\gamma_i^{\text{res}}$		Index	RMS of $\Delta\gamma_i^{\text{res}}$	
1	> 0	$\leqslant 0.025$	6	> 0.125	$\leqslant 0.150$
2	> 0.025	$\leqslant 0.050$	7	> 0.150	$\leqslant 0.175$
3	> 0.050	$\leqslant 0.075$	8	> 0.175	$\leqslant 0.200$
4	> 0.075	$\leqslant 0.100$	9	> 0.200	$\leqslant 0.225$
5	> 0.100	$\leqslant 0.125$	10	> 0.225	

the Fredenslund and the Van Ness test, residuals should spread randomly around zero. Next to the stated test criteria, the quality of fit of the total pressure is another important quantity to consider.

Other consistency tests involving fitting parameters of a g^{E}-model have been developed, but they rely on the same basis as the Fredenslund and the Van Ness test. A compilation of other test approaches can be found in the literature [20].

2.3. Thermodynamic consistency at high pressure

The concepts presented above can be applied to binary systems at constant temperature and at low to moderate pressures. For high pressures, the neglect of excess volumes, Poynting corrections and the use of simple correlations for the vapor phase non-idealities are no longer justified. Usually, the two-phase region emerges over the temperature range of the higher-boiling component(s), but at considerably higher pressures up to several hundreds of bar. At these pressures, real gas behaviour is significant and the assumptions

$$\frac{\varphi_i^{\text{V}}}{\varphi_{0i}^{\text{sat}}} \exp\left(\int_{p_{0i}^{\text{sat}}}^{p} \frac{v_{0i}^{\text{L}}}{RT} \mathrm{d}p\right) \approx 1 \tag{2.50}$$

$$\gamma_i \neq f(p) \tag{2.51}$$

no longer stand. Also, calculations of the fugacity coefficients of the vapor phase by virial equations truncated after the second term or by unmodified cubic EoS become questionable and require further analysis. The activity coefficients depend on pressure through

$$\left(\frac{\partial \gamma_i}{\partial p}\right)_{T,x_i} = \frac{v_i}{RT}. \tag{2.52}$$

High pressure phase equilibria usually involve a super-critical component, where the pure vapor pressure in Equation 2.15 is ill-defined and requires application of either the φ-φ-method or the infinite dilution reference in the γ-φ-method.

For application of the φ-φ-method, the Gibbs-Duhem equation is expressed in residual properties

$$\sum_i^K x_i \mathrm{d}g^{\mathrm{res}} = -\frac{h^{\mathrm{res}}}{T}\mathrm{d}T + v^{\mathrm{res}}\mathrm{d}p \tag{2.53}$$

$$\sum_i^K x_i \mathrm{d}\ln\varphi_i = -\frac{h^{\mathrm{res}}}{RT^2}\mathrm{d}T + \frac{v^{\mathrm{res}}}{RT}\mathrm{d}p \tag{2.54}$$

introducing an inter-dependency of the fugacity coefficients analogous to the activity coefficients in Equation 2.30 [27]. For an isothermal binary VLE, Equation 2.53 yields

$$z_1\mathrm{d}\ln\varphi_1 + z_2\mathrm{d}\ln\varphi_2 = \frac{v^{\mathrm{res}}}{RT}\mathrm{d}p = \left(\frac{Z-1}{p}\right)\mathrm{d}p. \tag{2.55}$$

The evaluation of Equation 2.55 requires an EoS for calculation of the fugacity coefficients and compressibility factors. In principle, the EoS parameters are fitted to experimental data and the thermodynamic consistency of the EoS is tested. Valderrama et al. [28] have suggested the evaluation of a cubic EoS for this purpose. Christiansen and Fredenslund [29] and Won and Prausnitz [30] proposed evaluation procedures for the γ-φ-method.

Due to real gas behaviour, thermodynamic consistency tests lose a lot of their value, since their results depend even more on suitable models. Consistency testing of a new high pressure data set without previously measured literature data is hardly possible because the suitability of the EoS and/or g^{E}-model cannot be checked beforehand. Therefore, the use of high-pressure consistency tests based on the Gibbs-Duhem equation is not wide-spread. Instead, other markers of data quality are used. Common markers are the scattering of the data points, consistency test with other mixtures measured with the same equipment, comparison against available literature data of the same or a similar mixture, deviations to a model with predictive capability or the calculation of Henry-coefficients at low solute concentrations or enhancement factors E. Contrary to the activity coefficient, which contains model assumptions, the enhancement factor is a purely experimental quantity, defined by

$$E = \frac{y_2 p}{p_{02}^{\mathrm{sat}}}, \tag{2.56}$$

with 2 being the high-boiling component. Using Equation 2.15, the enhancement factor is expressed as

$$E = \frac{y_2 p}{p_{02}^{\mathrm{sat}}} = \frac{x_2\gamma_2\varphi_{02}^{\mathrm{sat}}\exp\left(\int_{p_{02}^{\mathrm{sat}}}^{p}\frac{v_{02}^{\mathrm{L}}}{RT}\mathrm{d}p\right)}{\varphi_2^{\mathrm{V}}}, \tag{2.57}$$

describing the ratio of liquid phase to vapor phase non-idealities. For the pure substance, the the total pressure approaches the pure component vapor pressure, yielding

$$\lim_{y_2 \to 1} E = 1. \tag{2.58}$$

2.4. Equations of state

Equations of state are based on the premise, that the thermodynamic behaviour of fluids can be described by the same set of equations with different parameters. These parameters are either obtained through physical models based on molecular or atomic properties, such as particle size, dipole moments or molecular mass, or through fitting to experimental data, which usually concerns phase equilibria, heat capacity, density and speed of sound data. In the latter case, parameters are determined by minimisation of the target function

$$Z_{\text{target}} = \sum_X \sum_i \left(\frac{\Delta X_i}{w_{X,i}} \right)^2, \tag{2.59}$$

adding up the deviations between experimental data and the values obtained through the EoS with $w_{X,i}$ being weighting factors of the respective thermodynamic property X_i. The weighting factors are typically associated with the measurement uncertainty, but can also be adjusted to preferably represent a specific thermodynamic property. The relative root mean square error

$$RRMSE = \sqrt{\frac{Z_{\text{target}}}{n-1}} \tag{2.60}$$

is an indicator for the quality of the fit. A value close to unity indicates deviations within the uncertainties defined by the weighting factors.

For mixtures, the EoS parameters of the pure fluids are left constant, while interaction parameters are fitted to the mixture data. Usually, phase equilibrium or speed of sound data are used, as these are sensitive to the interaction parameters. Speed of sound data is of particular interest, as it combines thermal with caloric properties as well as first and second order derivatives of a fundamental potential [31]. In general, both, thermal and caloric properties should be used for parameter fitting in order to represent both property types accurately. Recently, Jaubert et al. demonstrated that inclusion of enthalpy and heat capacity of mixing in the fitting process of a predictive cubic EoS had decreased the total error in these properties by one order of magnitude without affecting the accuracy of vapor pressure calculations [32].

2.5. **Principle of corresponding states**

A common concept for EoS modeling is the principle of corresponding states, stating that fluids show the same behaviour if reduced temperatures, pressures and densities

$$\tau = \frac{T_{\mathrm{crit}}}{T}, \qquad\qquad \delta = \frac{\rho}{\rho_{\mathrm{crit}}}, \qquad\qquad p_{\mathrm{r}} = \frac{p}{p_{\mathrm{crit}}} \qquad (2.61)$$

are used. It stipulates a substance-independent compressibility factor at the critical point. In Figure 2.2 the critical compressibility factor for selected refrigerants is plotted against the respective critical temperatures.

Some general remarks can be concluded from this simple plot:

1. The principle of corresponding states works well with air constituents. Simple thermodynamic models based on ideal spherical particles can be used, although argon is the only real spherical particle.

2. The cryogens helium, hydrogen and neon are the only substances with higher critical compressibility factors than the ideal spherical particles, which indicates higher repulsive forces between the particles and larger zero-point energies. Therefore, they require a different modeling strategy than the other substances.

3. Hydrocarbons (HC) and (partially) fluorinated hydrocarbons (HFC) show negative deviations from the air constituents indicating higher attractive forces. The critical compressibility factors of HC are proportional to the critical temperatures along the homologous series. This behaviour allows to implement scaling parameters representing the chain length, i.e. segment numbers, acentric factors, molecular mass.

4. While the perfluorocarbons R14, R116, R218 show similar behaviour to their corresponding HC, HFCs seriously deviate from them. Different attractive forces are present, for which the chain length based quantities cannot fully account. Influencing parameters are the number of substituents, the configuration and dipole moments.

These conclusions drawn from the critical points are simplistic with regard to the overall fluid behaviour in the sub- and super-critical regions. For instance, cryogens can be treated with similar models as air constituents in their super-critical domain. However, Figure 2.2 shows that theoretical approaches developed for modeling of attractive forces at non-cryogenic conditions might not be easily transferred to the modeling of cryogens.

There is an overwhelming variety of EoS to model the fluid behaviour of pure substances and mixtures. They can be classified into virial EoS, cubic EoS, EoS based on perturbation theory and multi-parameter EoS. They are briefly introduced in the following sections and discussed with regard on their suitability for the description of cryogens and multi-component refrigerant mixtures.
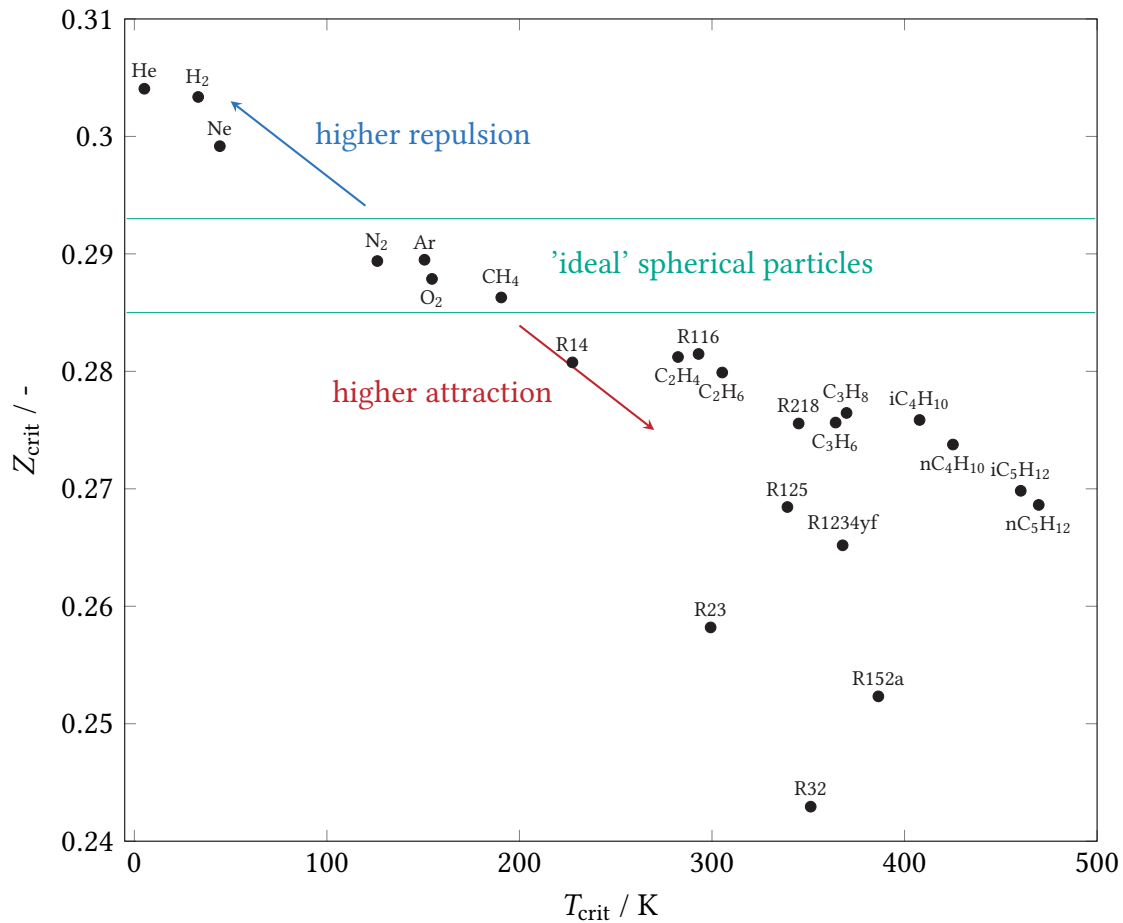
Figure 2.2.: Compressibility factors at the respective critical point of selected refrigerants with data taken from REFPROP 10.0 [33].

2.6. Virial equation of state

The virial EoS is a density- or pressure-explicit expansion of the compressibility factor originating from the ideal gas law

$$Z = 1 + B\rho + C\rho^2 + D\rho^3 + \dots \tag{2.62}$$

$$Z = 1 + B'p + C'p^2 + D'p^3 + \dots \tag{2.63}$$

The second virial coefficient B sufficiently describes the behaviour of low-density real gases. It is widely available for pure substances and can be easily fitted to binary data. It monotonically increases with temperature, passing through the characteristic Boyle temperature, where $B = 0$. Experimentally, it can be accurately determined from speed of sound data [34]. Often, the virial EoS is truncated after the second or third term, which is assumed to be sufficient to account for the real gas behaviour.

The virial EoS can also be derived from statistical mechanics depending on the assumed pair potential $u(r)$ and the probability density function of the particles. For a pure substance obeying the Maxwell-Boltzmann statistics, the second virial coefficient is defined by

$$B(T) = -2\pi \int_0^\infty \left(\exp \frac{-u(r)}{kT} - 1 \right) r^2 \mathrm{d}r. \qquad (2.64)$$

It can be extended to mixtures through

$$B_{\mathrm{mix}} = \sum_i \sum_j z_i z_j B_{ij}, \qquad (2.65)$$

with B_{ii} being the pure component virial coefficients and B_{ij} the interaction virial coefficients. For higher order virial coefficients, the formation of clusters, i.e. many-body interactions, must be taken into account.

The behaviour of low density gases can be accurately described with the first two virial coefficients $\{B, C\}$ close to and above the Boyle temperature. Below the Boyle temperature, the accuracy can be increased for most substances by including higher order terms. Attempts have been made to include quantum effects, i.e. quantised energy states and variations of the particle distribution function, by expansion of the classical limit in powers of Planck's constant h^2 [35]. At low temperatures, the description of the particle distribution with the Maxwell-Boltzmann statistics is no longer valid and it must be distinguished between fermions, behaving according to the Fermi-Dirac statistics, and bosons, following the Bose-Einstein statistics. ^{4}He behaves as boson, while ^{3}He as a fermion. Natural neon is a mixture of two bosonic isotopes ^{20}Ne with 90.9 % and ^{22}Ne with 8.8 % and one fermionic isotope ^{21}Ne with 0.3 % [36]. For a rigid quantum-mechanical derivation of the second virial coefficients for fermions and bosons see [37].

Despite its firm theoretical grounds, the virial EoS has been modified empirically by Benedect, Webb and Rubin (BWR-EOS) by inclusion of reciprocal and exponential terms of temperature and density summing up to 8 fitting parameters [38]. The BWR-EoS has been further modified by Starling (BWRS-EoS) with a total of 11 fitting parameters, which is still available in common simulation software, e.g. Aspen Plus [39]. These modified EoS are rather classified as multiparameter EoS as they are empirically derived.

The virial EoS is suitable do describe the $p\rho T$-behaviour of low to moderate-dense fluid mixtures accurately. By precise measurement of speed of sound, determination of the virial coefficients gives an insight into the underlying pair potentials. The virial EoS cannot describe complex phase equilibria involving fluids at high densities. For these systems, the virial EoS can be used to determine vapor phase fugacities in combination with activity coefficient models for the γ-φ-approach.

2.7. Cubic equations of state

Cubic EoS are based on the two-parameter EoS developed by van der Waals in 1887 [40]. Van der Waals introduced the concept of attractive and repulsive forces into the ideal gas law

$$p = \frac{RT}{V - b_{c,vdW}} - \frac{a_{c,vdW}}{V^2},$$

(2.66)

where $a_{c,vdW}$ denotes the critical attractive parameter accounting for the attractive forces between the particles and $b_{c,vdW}$ the covolume, which reduces the free volume by 4 times the occupied volume of the particles. Solving Equation 2.66 at saturation conditions yields three roots, where the highest volume corresponds to the saturated vapor and the lowest to the saturated liquid.

For mixtures, the parameters $a_{c,vdW}$ and $b_{c,vdW}$ are calculated through the mixing rules

$$a_{c,vdW} = \sum_i \sum_j z_i z_j a_{ij} (1 - k_{ij}), \text{ with } k_{ii} = 0, \ k_{ij} = k_{ji}$$

(2.67)

$$b_{c,vdW} = \sum_i z_i b_i \left(1 - l_{ij}\right),$$

(2.68)

with the combining rule

$$a_{ij} = \sqrt{a_i a_j}.$$

(2.69)

The vdW EoS was the first equation to qualitatively describe the two-phase regions, even though it has major shortcomings for quantitative description. Therefore, Equation 2.66 has inspired a variety of modifications and semi-empirical derivatives concerning

1. modifications of the attractive term,
2. modifications of the repulsive term,
3. volume shifts and
4. mixing and combining rules.

The most commonly used derivatives of the vdW EoS are the Soave-Redlich-Kwong (SRK) [41] and the Peng-Robinson (PR) EoS [42], which are widely available in calculation and process simulation software. The modifications can be expressed by

$$p = \frac{RT}{V - b} - \frac{a_c \alpha\left(T\right)}{\left(V + q_1 b\right)\left(V - q_2 b\right)} \text{ with}$$

(2.70)

$$\alpha\left(T\right) = \left(1 + m\left(1 - \sqrt{\frac{T}{T_c}}\right)\right)^2.$$

(2.71)

The respective parameters a_c, b, m, q_1, q_2 are defined in Table 2.2. As can be seen from Equation 2.70, the flexibility of the equation is increased by introducing a temperature-dependence in the attraction term $\alpha(T)$ and different parameters in the polynomial in the denominator. Most published α-functions are designed for specific fluids and aim at

Table 2.2.: Parameters for the vdW, SRK and PR EoS.

EoS	$a_c / \frac{R^2 T_c^2}{p_c}$	$b / \frac{RT_c}{p_c}$	m	q_1	q_2
vdW	0.42188	0.125	0	0	0
SRK	0.42747	0.08664	$0.48 + 1.574\omega - 0.176\omega^2$	1	0
PR	0.45724	0.07780	$0.37464 + 1.54229\omega - 0.26992\omega^2,\ \omega \leq 0.491$ $0.379642 + 1.48503\omega - 0.164423\omega^2,\ \omega > 0.491$	$1 + \sqrt{2}$	$1 - \sqrt{2}$

accurate representations of either phase boundaries or p, v, T-behaviour. Le Guennec et al. have developed a consistency test for α-functions to guarantee results in sub-critical as well as super-critical states to be physically meaningfull [43]. They stipulate the following criteria:

$$\alpha (T) > 0 \text{ and continuous,} \tag{2.72}$$

$$\frac{\mathrm{d}\alpha (T)}{\mathrm{d}T} < 0 \text{ and continuous,} \tag{2.73}$$

$$\frac{\mathrm{d}^2 \alpha (T)}{\mathrm{d}T^2} > 0 \text{ and continuous,} \tag{2.74}$$

$$\frac{\mathrm{d}^3 \alpha (T)}{\mathrm{d}T^3} \leq 0 \tag{2.75}$$

The original α-function from Soave (see Equation 2.71), which is used in the SRK and PR EoS, fails this consistency test, because it does not monotonically decrease (violation of second criterion). Among others, the α-function from Twu (1991)

$$\alpha (T) = \left(\frac{T}{T_c} \right)^{N(M-1)} \exp \left[L \left(1 - \left(\frac{T}{T_c} \right)^{MN} \right) \right], \tag{2.76}$$

which is widely available in simulation programs, has been found to be consistent, while still offering flexibility thanks to three parameters L, M, N [43]. It combines a polynomial term, which has been shown to yield good results in sub-critical regimes, with an exponentially decreasing term, which gives a good representation of the super-critical domain. However, some constraints apply for the choice of parameters, which are given in [43].

Modifications of the repulsive term are based on the hard-sphere fluid proposed by Carnahan and Starling (CS) [44]

$$Z_{\mathrm{HS}} = \frac{1 + \eta + \eta^2 - \eta^3}{(1 - \eta)^3} \text{ with } \eta = \frac{b}{4V}, \tag{2.77}$$

which is based on the infinite square well potential

$$u (r) = \begin{cases} \infty & \text{for } r \leq r_{\mathrm{particle}} \\ 0 & \text{for } r > r_{\mathrm{particle}}. \end{cases} \tag{2.78}$$

As such, it is a purely repulsive EoS, which can be combined with an attractive term yielding the Carnahan-Starling-van-der-Waals (CSvdW) EoS

$$Z = \frac{1 + \eta + \eta^2 - \eta^3}{(1 - \eta)^3} - \frac{a}{RTV}. \tag{2.79}$$

The modification of the repulsive term by introducing the hard-sphere concept from Carnahan and Starling has a firm thermodynamic background and shows good representation of hydrocarbon systems [45]. However, it is not implemented in commercial process engineering softwares.

Péneloux et al. noticed that the difference between experimental liquid densities and the ones calculated by the SRK EoS is approximately constant [46]. Therefore, they introduced a temperature-independent volume shift $c_{\text{Péneloux}}$ to exactly determine the saturated liquid density at a reduced temperature of $T_r = 0.7$

$$c_{\text{Péneloux}} = v^{\text{L,sat, calc}} (T_r = 0.7) - v^{\text{L,sat, exp}} (T_r = 0.7). \tag{2.80}$$

Later, Le Guennec et al. have found a reduced temperature of $T_r = 0.8$ to be optimal for most fluids [47]. Jaubert et al. have shown, that a temperature-independent volume shift does not affect heat capacities, vapor pressures and entropies [48]. The fitting of the EoS parameters to vapor pressures, saturation and super-critical properties can be uncoupled from the fitting to the liquid density. A full list of properties affected by a temperature-independent volume shift was published by Jaubert et al. [48]. For mixtures, they have found that a linear mixing rule for the Péneloux parameter

$$c_{\text{Péneloux}} = \sum_i z_i c_{\text{Péneloux},i} \tag{2.81}$$

had preserved the properties of mixing and the phase envelopes. Other authors have proposed temperature-dependent volume shifts to increase flexibility in the repulsive term at the cost of potential inconsistencies. Several authors have reported negative heat capacities at high temperatures and crossings of isotherms [47]. Therefore, it must be assured that the p, ρ, T-domain of interest is not affected.

Mixing rules are another possibility to increase the flexibility of an EoS. All mixing rules are to some extend arbitrary, since there is no physically correct way to correlate different thermodynamic properties except a rigorous virial expansion. Popular mathematical expressions are the linear and quadratic mixing rules proposed by van der Waals. For the covolume, he proposed to use a linear mixing rule (Equation 2.68) and for the attraction parameter a quadratic mixing rule (Equation 2.67) with a geometric-mean combining rule (Equation 2.69) complying with the second virial coefficient calculations. Both parameters can be weighed with binary interaction parameters k_{ij} and l_{ij}. Some authors introduced dependencies of temperature into these interaction parameters. Composition dependencies can be obtained from g^{E}-models. This way, the activity coefficient models required for complex liquid mixtures can be incorporated into the EoS and the φ-φ-approach. Such mixing rules are required for accurate modeling of HFCs and their mixtures [49]. Usual

variants are the Huron-Vidal, Wong-Sandler and Orbey-Sandler mixing rules, which are summarised in [37, 50].

In 2016, Le Guennec et al. have published the translated-consistent PR (tc-PR) EoS [47]. Based on the various derivatives discussed above, they use the basic PR EoS with the following modifications:

$$p\left(T, v\right) = \frac{RT}{v - b} - \frac{a_c \alpha \left(T_r\right)}{\left(v + c\right)\left(v + b + 2c\right) + \left(b + c\right)\left(v - b\right)} \text{ with} \tag{2.82}$$

$$\alpha\left(T_r\right) = T_r^{N(M-1)} \exp\left[L\left(1 - T_r^{MN}\right)\right], \tag{2.83}$$

$$c_{\text{Péneloux}} = v^{\text{L,sat,calc}}\left(T_r = 0.8\right) - v^{\text{L,sat,exp}}\left(T_r = 0.8\right), \tag{2.84}$$

$$a_c = 0.45724 \frac{R^2 T_c^2}{p_c}, \tag{2.85}$$

$$b = 0.07780 \frac{RT_c}{p_c} - c_{\text{Péneloux}}. \tag{2.86}$$

A similar approach is used for the RK EoS. Le Guennec et al. have presented parameter sets $\{L, M, N, c\}$ for more than 1000 substances, which they obtained through regression of vapor pressures, heats of vaporisation and isobaric heat capacities at saturation. This EoS is implemented in many simulation softwares.

Computational effort for the solution of cubic EoS is low, allowing quick solutions of complex thermodynamic problems such as fluid dynamic simulations with fine grids or vast chemical processes consisting of several unit operations. Therefore, cubic EoS, and predominantly the PR EoS, are used for MRC design calculations [51]. When setting up a simulation, the accuracy of the tc-PR EoS should be checked against experimental data or more accurate (multiparameter) EoS in the pressure, temperature and composition domain of interest if available for the fluid (mixture). In particular, derivative properties such as heat capacities should be checked against experimental data for consistency and accuracy. Nevertheless, when using multi-component mixtures with few experimental data, calculations with cubic EoS deliver a good first estimate of the behaviour, which is not necessarily worse than more sophisticated EoS. For instance, cubic EoS show a similar accuracy for VLE calculations of binary carbon dioxide mixtures compared to SAFT-type EoS [52]. However, they require larger binary interaction parameters k_{ij} than the SAFT-type EoS, which compromises their predictive capabilities.

2.8. Perturbation-based EoS

Perturbation theory aims at describing macroscopic fluid properties based on microscopic intra- and intermolecular forces. Due to this physical foundation, EoS based on perturbation theory are of particular interest for systems with low experimental coverage implying a certain degree of predictability. If thorough physical models are used, perturbation theory can be expected to yield better results than other EoS types for the extrapolation of data. The EoS are usually based on the Helmholtz energy of a reference system, which

is perturbed by additional terms. Zwanzig expanded the reduced Helmholtz energy a in terms of $\beta = 1/k_\mathrm{B}T$

$$a = a_0 + \beta a_1 + \beta^2 a_2 + \beta^3 a_3 + O\left(\beta^4\right), \tag{2.87}$$

where k_B denotes Boltzmann's constant, a_0 denotes the Helmholtz energy of the reference system and a_i the ith perturbation coefficients [53]. The coefficients depend on the potential $u(r)$ and the distribution of the particles in the system, which is characterized by the radial distribution function (RDF) $g(r)$. The radial distribution function can be interpreted as the probability of finding a particle at distance r from the reference particle at $r = 0$. Similarly to virial EoS, the first perturbation coefficient represents two-body interactions with a pair potential $u_1(r)$ superposing the reference potential $u_0(r)$. Different models are worth considering as reference state. The system of spherical hard spheres

$$u^\mathrm{HS}\left(r\right) = \begin{cases} \infty, & r < \sigma \\ 0, & r \geqslant \sigma \end{cases} \tag{2.88}$$

as described by Carnahan and Starling is a popular choice [44]. The residual Helmholtz energy of the hard-sphere system is given by

$$a = \frac{\eta\left(4 - 3\eta\right)}{\left(1 - \eta\right)^2}, \tag{2.89}$$

with the packing fraction

$$\eta = \frac{\pi \sigma^3}{6 \tilde{\rho}}. \tag{2.90}$$

Radial distribution functions of spherical hard spheres are available, e.g. the solution of the Percus-Yevick equation provided by Wertheim $g^\mathrm{HS}\left(r\right)$ [54, 55, 56, 57]. For higher order perturbations, three- and four-body distribution functions are required. Since these are not as readily available as the RDF from Wertheim, Barker and Henderson have developed approximations for the second perturbation coefficient, which make use of $g^\mathrm{HS}\left(r\right)$ [58, 59]. They have applied Zwanzig's theory to a square-well fluid (SW)

$$u^\mathrm{SW}\left(r\right) = \begin{cases} \infty, & r < \sigma \\ -\varepsilon, & \sigma \leqslant r \leqslant \lambda\sigma \\ 0, & r \geqslant \lambda\sigma, \end{cases} \tag{2.91}$$

with ε being the well depth and λ the well width. They also developed a routine to include soft-core potentials such as the Lennard-Jones potential (LJ)

$$u^\mathrm{LJ}\left(r\right) = 4\varepsilon\left(\left(\frac{\sigma}{r}\right)^{12} - \left(\frac{\sigma}{r}\right)^6\right), \tag{2.92}$$

while still using hard spheres as a reference system. To map the steep potential rise onto the hard sphere reference, they introduced a variable, temperature-dependent diameter

$$d(T) = \int_0^\sigma \left(1 - \exp(-\beta u(r))\right) dr.$$ (2.93)

The resulting equation set for the Barker Henderson perturbation theory is:

$$a = a_0 + \beta a_1 + \beta^2 a_2,$$ (2.94)

$$a_0 = \frac{\eta(4 - 3\eta)}{(1 - \eta)^2}, \text{ with } \eta = f(d(T))$$ (2.95)

$$a_1 = 2\pi\rho \int u(r) g^{\mathrm{HS}}(r) r^2 dr$$ (2.96)

$$a_2 = \frac{\rho}{4} \int u^2(r) k_{\mathrm{B}} T \left(\frac{\partial}{\partial p} \rho g^{\mathrm{HS}}(r)\right) 4\pi r^2 dr.$$ (2.97)

The perturbation theory from Barker and Henderson has been refined by Lafitte et al. [60] by using the generic Mie potential

$$u^{\mathrm{Mie}}(r) = C\varepsilon \left(\left(\frac{\sigma}{r}\right)^{\lambda_{\mathrm{rep}}} - \left(\frac{\sigma}{r}\right)^{\lambda_{\mathrm{att}}}\right), \text{ with }$$ (2.98)

$$C = \frac{\lambda_{\mathrm{rep}}}{\lambda_{\mathrm{rep}} - \lambda_{\mathrm{att}}} \left(\frac{\lambda_{\mathrm{rep}}}{\lambda_{\mathrm{att}}}\right)^{\frac{\lambda_{\mathrm{att}}}{\lambda_{\mathrm{rep}} - \lambda_{\mathrm{att}}}}.$$ (2.99)

They also extended the theory with an empirical third order perturbation term a_3.

A landmark EoS based on Wertheim's contributions is the original SAFT EoS from Chapman et al. [61, 62]. Additionally to the hard sphere and the dispersion terms introduced above, contributions from chain formation and association

$$a = a^{\mathrm{HS}} + \underbrace{a^{\mathrm{disp}}}_{= a_1 + \beta a_2 + \beta^2 a_3} + a^{\mathrm{chain}} + a^{\mathrm{assoc}}$$ (2.100)

are considered. Several derivatives of this original SAFT EoS have been proposed either through modifying the interaction potential (e.g. SAFT-VR [63, 64]) or the reference system (e.g. PC-SAFT [65]) by simplifying complex analytical terms (e.g simplified SAFT [66]) or by including other contributions (e.g. polar soft-SAFT [67]).

For simple, non-associating hydrocarbons, their mixtures and their mixtures with cryogenic fluids, the PC-SAFT EoS represents the state of the art of SAFT-type EoS. It uses a chain of segments as reference potential and requires three parameters, the segment number m, the particle diameter σ and the energy parameter ε to model pure non-

associating fluids. It can be extended to mixtures using the Lorentz-Berthelot combining rules

$$\sigma_{ij} = \frac{\sigma_{ii} + \sigma_{jj}}{2} \tag{2.101}$$

$$\varepsilon_{ij} = \sqrt{\varepsilon_{ii}\varepsilon_{jj}} \left(1 - k_{ij}\right) \tag{2.102}$$

for the mixing rules

$$\sigma_{\text{mix}}^3 = \frac{\sum_i \sum_j x_i x_j m_i m_j \sigma_{ij}^3}{\left(\sum_i x_i m_i\right)^2} \tag{2.103}$$

$$\varepsilon_{\text{mix}}\sigma_{\text{mix}}^3 = \frac{\sum_i \sum_j x_i x_j m_i m_j \sigma_{ij}^3 \varepsilon_{ij}}{\left(\sum_i x_i m_i\right)^2}. \tag{2.104}$$

Despite the physical meaning of the three parameters, care must be taken when using parameters from different SAFT-type EoS. Moreover, parameters are typically fitted to VL(L)E and liquid density data, thereby neglecting caloric properties [68]. When solving a SAFT-type EoS in the two-phase region, more than three volume roots may arise, which must be considered when choosing a solving algorithm [69].

Thus, literature parameters might give a first indication of the physical properties, but should be re-fitted to the respective EoS as well as to the desired physical properties in order to be accurate. Due to a lack of data, verifications of PC-SAFT predictions for caloric properties are rarely addressed. Zhu et al. compared the predictions of pure fluid heat capacities for different SAFT-type EoS [70]. The PC-SAFT EoS showed the best representation for non-associating fluids, i.e. the fluids of interest for MRCs. Alfradique and Castier compared the predictions of the PR EoS and the PC-SAFT EoS for several synthesised natural gas mixtures without using binary interaction parameters [71]. The PC-SAFT EoS proved to yield considerably better predictions of the VLEs than the PR EoS, which is in line with the findings of Diamantonis et al. [52].

Computational effort depends on the complexity of the applied perturbations as well as on the number of components. For non-polar and non-associating fluids, programming effort is moderate compared to cubic EoS [72]. When using reduced variables and the reduced Helmholtz energy, the model equations can be solved with similar algorithms as multiparameter EoS, mostly using successive substitution iteration or Newton-Raphson methods. Conclusively, the PC-SAFT EoS is available in commercial simulation software such as Aspen Plus.

2.9. Multiparameter equations of state

Multiparameter EoS are based on the compressibility factor or the Helmholtz energy. They aim at reproducing experimental data within their measurement uncertainty without depending on a certain physical background. These reference EoS are used to calculate

pseudo-experimental data at the desired condition instead of relying on experimental data tables. The most general form of such an EoS reads

$$Z\left(T, \rho\right) = 1 + Z^{\mathrm{res}}\left(T, \rho\right) \tag{2.105}$$

or equivalently

$$\alpha\left(\tau, \delta\right) = \alpha_0 + \alpha^{\mathrm{res}}\left(\tau, \delta\right). \tag{2.106}$$

The first term on the right hand side of Equation 2.106 refers to the ideal gas state and the second term to residual properties perturbing this ideal reference. Most modern multiparameter EoS are based on the reduced Helmholtz energy instead of the compressibility factor to obtain all properties by differentiation instead of integration. Therefore, the following section focuses on the reduced Helmholtz energy, based on Span [18].

The ideal gas part is based on the thermodynamic expression of the Helmholtz energy

$$a_0\left(T, \rho\right) = u_{0,\mathrm{ref}} - Ts_{0,\mathrm{ref}} + \int_{T_{\mathrm{ref}}}^{T} c_{v,0}\mathrm{d}T - T\int_{T_{\mathrm{ref}}}^{T} \frac{c_{v,0}}{T}\mathrm{d}T + RT\ln\left(\frac{\rho}{\rho_{\mathrm{ref}}}\right). \tag{2.107}$$

Application of the definition of the pressure $p = -\rho^2 \left(\partial a/\partial v\right)_T$ yields a pressure-explicit thermal equation of state, known as the ideal gas law

$$p = RT\rho. \tag{2.108}$$

Caloric properties require information about the temperature dependence of the isochoric heat capacity in order to solve the integrals. In principle, the heat capacity depends on the degrees of freedom c_i of translational, rotational and vibrational modes

$$c_{v,0} = c_{\mathrm{trans}} + c_{\mathrm{rot}} + c_{\mathrm{vib}}. \tag{2.109}$$

Equation 2.109 stands under the assumptions of fully excited modes and no interactions of the movements (e.g. vibrational modes moving the centre of mass). Translational and rotational contributions can be expressed by weighing half the universal gas constant with the degrees of freedom. Heat capacities of mono-atomic gases have a temperature-independent heat capacity of $c_{v,0} = c_{\mathrm{trans}} = 3/2R$. Other molecules, which can rotate around two or three axis contribute $c_{\mathrm{rot}} = 2/2R$ or $c_{\mathrm{rot}} = 3/2R$ to the total heat capacity. Full excitation of the rotational modes can usually be assumed. Vibrational modes are modeled as harmonic oscillators. The frequency distribution of these oscillators follows the Bose-Einstein statistics in terms of temperature

$$c_{\mathrm{vib}} = R\sum_{i=1}^{I_{\mathrm{vib}}} \left(\frac{\Theta_i}{T}\right)^2 \frac{\exp\left(\frac{\Theta_i}{T}\right)}{\left(\exp\left(\frac{\Theta_i}{T}\right) - 1\right)^2} \tag{2.110}$$

and yields the temperature dependence of the heat capacity of the ideal gas.

To incorporate these heat capacity models into an equation of state in terms of the reduced Helmholtz energy

$$c_{v,0} = R\tau^2 \left(\frac{\partial^2 \alpha_0}{\partial \tau^2}\right)_\delta, \tag{2.111}$$

they are integrated twice leading to two temperature-dependent integration constants c_1, c_2. A typical multiparameter ansatz reads

$$\alpha_0 (\tau, \delta) = \ln \delta + c_2 + c_1\tau + c_0 \ln \tau + \sum_{i=3}^{I_{\text{pol}}} c_i\tau^{t_i} + \sum_{k=1}^{K_{\text{PE}}} m_k \ln (1 - \exp(-\vartheta_k\tau)), \tag{2.112}$$

with the first two terms accounting for the density contribution and the next four terms accounting for the temperature-dependence. The last term is a so-called Planck-Einstein (PE) equation based on Equation 2.110. The other temperature-dependent terms account for anharmonicities, interactions and other model weaknesses by a flexible polynomial.

The residual parts accounts for all deviations of the substance from the ideal reference state, particularly the two-phase domain. For this purpose, highly flexible mathematical terms are needed. An ansatz for the residual part reads

$$\alpha^{\text{res}} (\tau, \delta) = \underbrace{\sum_{i=1}^{I_{\text{pol}}} n_i\tau^{t_i}\delta^{d_i}}_{\text{polynomial (pol)}} + \underbrace{\sum_{i=I_{\text{pol}}+1}^{I_{\text{pol}}+I_{\text{exp}}} n_i\tau^{t_i}\delta^{d_i} \exp\left(-\gamma_i\delta^{d_i}\right)}_{\text{exponential-polynomial (exp)}} +$$

$$\underbrace{\sum_{i=I_{\text{pol}}+I_{\text{exp}}+1}^{I_{\text{pol}}+I_{\text{exp}}+I_{\text{gbs}}} n_i\tau^{t_i}\delta^{d_i} \exp\left(-\eta_i (\delta - \epsilon_i)^2 - \beta_i \left(\tau - \gamma_{i,\text{gbs}}\right)^2\right)}_{\text{Gaussian-bell shape (gbs)}}. \tag{2.113}$$

The polynomial term is based on van der Waals' thoughts on using a polynomial to describe the continuity across the phase boundaries, yielding roots at the saturation lines. The exponential-polynomial term adds flexibility, particularly to model the liquid phase properties, which is a weakness of the vdW EoS. The third term is a derivative of a Gaussian bell function in terms of temperature and density, originally introduced by Setzmann and Wagner [73]. This term accounts for the property changes in the vicinity of the critical point, which are drastic, e.g. considering the heat capacity curve.

The presented general equations have been adapted to different pure fluids by regression of the parameters $n_i, t_i, d_i, \gamma_i, \epsilon_i, \gamma_{i,\text{gbs}}, \eta_i, \beta_i$, as well as $I_{\text{pol}}, I_{\text{exp}}, I_{\text{gbs}}$. Thus, a certain bank of terms $\{I_{\text{pol}}, I_{\text{exp}}, I_{\text{gbs}}\}$ as well as parameter intervals have to be defined prior to parameter fitting. These depend on the substance to model, the abundance of experimental data and the optimisation algorithm.

The multiparameter EoS covering the most fluid mixtures is the GERG wide-range EoS for natural gases and other mixtures by Kunz and Wagner [74]. It comprises 21 natural gas components, i.e. methane, nitrogen, carbon dioxide, ethane, propane, n-butane, isobutane,

n-pentane, isopentane, n-hexane, n-heptane, n-octane, n-nonane, n-decane, hydrogen, oxygen, carbon monoxide, water, hydrogen sulfide, helium and argon in a temperature range from 60 K to 700 K and at pressures up to 700 bar. The GERG EoS is not applicable to cryogenic fluid mixtures below 50 K, since the data base does not allow high accuracy descriptions. For these mixtures, specific approaches must be defined.

To extend a multiparameter EoS to mixtures, a departure function

$$\Delta \alpha \left(\tau, \delta, x \right) = \alpha^{\text{res}} \left(\tau, \delta, x \right) - \sum_i x_i \alpha_i^{\text{r}} \left(\tau, \delta \right) \ \text{with} \tag{2.114}$$

$$\Delta \alpha \left(\tau, \delta, x \right) = \sum_i \sum_{j \neq i} x_i x_j F_{ij} \alpha_{ij}^{\text{res}} \left(\tau, \delta \right) \tag{2.115}$$

is used. The term $\alpha_{ij}^{\text{r}} \left(\tau, \delta \right)$ can be expressed by the Lorentz-Berthelot mixing rules, a linear mixing rule or a binary-specific equation. Another option is an adjustment of the pure component functions without defining a departure function, i.e. $F_{ij} = 0$.

The GERG EoS parameters are fitted to binary data as well as some synthetic natural gas mixtures with methane contents around 90 % yielding relative uncertainties below 1 % for most properties except some vapor pressures and heat capacities. However, most multi-component refrigerant mixtures have a methane content ranging from 20 % to 40 % depending on the desired cooling temperature. The extrapolation of the stated GERG EoS uncertainties to these mixtures is not a priori justified. As the current data base for these refrigerant mixtures is scarce, experimental data must be gathered at specific state of points of interest in order to verify the predictions of the GERG EoS. A holistic experimental data base for these refrigerant mixtures is not feasible due do their high numbers of degrees of freedom $\{p, T, z_i\}$.

In general, computational effort for the fitting procedures as well as solving the EoS at the desired state point is large compared to cubic or SAFT-type EoS. For complex simulations, the foreseen phase space should be determined and interpolated instead of using the EoS directly in the iteration steps. However, multiparameter EoS can be a great tool to evaluate the performance and suitability of other (simpler) EoS for a certain phase space and application.

2.10. Considerations for helium, hydrogen and neon

At low temperatures, cryogenic fluids with critical temperatures below 50 K (i.e. helium, hydrogen, neon) behave differently than other noble gases or air constituents, although being equally spherical. As mentioned before, the accurate description of the repulsive forces is crucial at these temperatures. A lot of researchers account these different modeling strategies to quantum effects [75, 15, 17, 76, 77, 78]. A reasonable measure for the implications of quantum effects is the thermal De Broglie wavelength [79]

$$\lambda_{\text{DeBroglie}} = \frac{h}{\sqrt{2 \pi m_{\text{p}} k_{\text{B}} T}} . \tag{2.116}$$

The De Broglie wavelength can be seen as an additional scaling parameter in the context of the corresponding states principle. If the interaction distances between two particles are of the same order as the thermal De Broglie wavelength, quantum statistical mechanics such as Bose-Einstein and Fermi-Dirac statistics replaces the classical Maxwell-Boltzmann statistics. It becomes relevant for low-weight particles (i.e. helium, hydrogen, neon) at low temperatures. Therefore, state-of-the-art EoS, which are based on a high-temperature ideal reference state perturbed by additional attractive forces, are not suited to describe this behaviour and need modifications in the low-temperature domain. There are two objectives for the treatment of these quantum effects:

1. Elimination of the quantum effect contributions induced by low molecular mass and high reduced properties to corresponding state calculations of mixtures at high temperatures,
2. Description of pure substance and fluid mixture properties at cryogenic temperatures by incorporation of quantum effects into existing EoS.

The first approach to eliminate the quantum effect contributions has been developed by Newton in 1935, introducing so-called *classical* critical properties [80]. The main idea is to treat helium, hydrogen and neon as classical fluids obeying the principle of corresponding states if applied in mixtures at moderate to high temperatures. Thus, the fluid behaviour is modeled by classic kinetic particle-particle interactions and the wave behaviour at low temperatures is 'turned of'. Particularly for cubic EoS, which rely on the critical parameters, the small values of the critical properties of the fluids lead to high reduced values, far from the values for which the corresponding states principle accounts for. For instance, helium has a reduced temperature of $\tau = 20$ at 100 K. By trial and error, Newton found that adding 8 K and 8 bar to the true critical temperature and pressure yielded a better representation of high-pressure phase equilibria of mixtures with helium, hydrogen or neon as super-critical components. The designation 'classical' has been introduced later to account for the interpretation of the concept that the critical temperature and pressure would be higher if the fluid was not affected by quantum effects.

The approach has been successfully used by Rowland et al. to calculate VLE of binary and ternary mixtures of helium with other natural gas components with the original PR EoS [81]. However, general judgements cannot be made without consideration of other physical properties or the applicability to other EoS than the original PR EoS. They suggested the use of classical critical properties in multiparameter EoS, such as the GERG EoS, as well. Messerly et al. calculated the critical properties by molecular simulation using a Gibbs ensemble Monte Carlo method for hypothetical classical helium and found similar values to the ones of Newton and Rowland et al. [82]. Kato and Tanaka have used a similar approach using the PR EoS for binary mixtures of helium, hydrogen and neon with higher boiling substances [83]. They made the critical pressure temperature-dependent and reported good results of binary VLEs without the need of binary interaction parameters. Deiters and Sadus give a summary of physical property data of classical helium [84].

While the classical critical properties lead to better representations of mixtures with HCs, phase equilibria below 100 K require quantum corrections to the EoS. Based on

the classical critical property concept of Newton, Gunn et al. proposed *effective* critical temperatures and pressures by making them temperature-dependent

$$T_{\text{crit,eff}} = \frac{T_{\text{crit,class}}}{1 + \frac{c_1}{m_{\text{p}}T}}, \qquad\qquad p_{\text{crit,eff}} = \frac{p_{\text{crit,class}}}{1 + \frac{c_2}{m_{\text{p}}T}}, \qquad (2.117)$$

with the fluid-independent constants $c_1 = 21.8\,\text{K}$ and $c_2 = 44.2\,\text{K}$ [85]. This way, the effective critical temperature is smaller than the real one in the sub-critical domain and asymptotically equals the classical critical temperature at high temperatures. The constants have been obtained through fitting of compressibility factor data to Pitzer's virial correlation yielding *ARD* = 0.85 % for pure helium and *ARD* = 0.29 % for pure hydrogen. Later, Chueh and Prausnitz applied the same concept to mixtures using the RK EoS [76]. The authors could improve the representation at cryogenic conditions, but did not reach the accuracy level of classical fluids. Solen et al. have used these findings to calculate the solubility of helium in several cryogenic solvents and reported good estimates [86]. However, this approach is not found in commercial software except for ASPEN HYSYS, where a *modify critical properties for hydrogen and helium* option exists.

In general, cubic EoS have a lot of flexibility in the attractive term, while the repulsive term stays unmodified in most cubic derivates. For cryogens, this attractive term can become negative (i.e. repulsive) using unconstrained parameter fitting. For instance, the use of the Soave α-function requires negative values for the acentric factors resulting in a negative attraction term. This conclusion has also been made by Le Guennec et al. [47], who failed to find parameters for their α-function for helium and hydrogen which comply with their consistency criteria. Kaviani et al. have fitted 10 parameters of an α-function and a function describing the covolume to model the behaviour of helium at temperatures below 15 K [87]. Despite the high number of parameters, gas densities show an *ARD* of 7 % with respect to the reference EoS. In principle, the covolume should increase when decreasing temperature to introduce higher repulsive forces into the EoS, thereby keeping the α-function positive. However, temperature-dependent covolumes lead to other inconsistencies, for instance negative heat capacities [88]. Aasen et al. have introduced such a temperature-dependent covolume into the tc-PR EoS

$$b_{\text{quantum}}\,(T) = b_{\text{class}}\beta\,(T) \quad \text{with} \qquad\qquad (2.118)$$

$$\beta\,(T) = \frac{\left(1 + \frac{A}{T+B}\right)^3}{\left(1 + \frac{A}{T_{\text{crit}}+B}\right)^3}, \qquad\qquad (2.119)$$

which they derived from their SAFT-type EoS based on a Feynman-Hibbs path integral approach [89]. The covolume has a cubic dependence from the inversed reduced temperature, hence, accounting for quantum swelling while retaining the classical limit at the critical point. This cubic temperature-dependence is derived from a quantum correction to the SAFT-VR Mie EoS [90]. Their cubic EoS shows high accuracy with ARDs of 4 % for the isochoric heat capacity, 1 % for vapor pressure and 1 % to 2 % for density. Isobaric heat capacity deviations range from 8 % to 13 %. Binary VLEs at cryogenic temperatures are well-represented including LLE and azeotropic behaviour. The temperature-dependence

of the covolume does not introduce any inconsistencies within the region of technical interest. Their SAFT-type EoS shows good agreement for the hydrogen-neon mixture but over predicts the critical point of helium-neon and helium-hydrogen mixtures by more than 50 %. Other SAFT-based approaches aim at including the De Broglie wavelength $\lambda_{\text{DeBroglie}}$ as well. In these approaches, $\lambda_{\text{DeBroglie}}$ serves as scaling factor for corrections to the perturbation terms [75, 91] or for modifications of effective particle diameters to account for quantum swelling [92, 93]. Finally, none of the proposed cubic or SAFT-type EoS is able to accurately reproduce experimental data sets $\{\rho, p, T, c_p, w, X_{\text{sat}}\}$ for all three cryogens and their mixtures.

Tkaczuk et al. published a multiparameter EoS for binary cryogenic mixtures [17]. The authors succeeded to represent the experimental data with high accuracy. Claimed uncertainties for the binary systems He-Ne, He-Ar and Ne-Ar are 0.5 % to 3 % for density, 1 % to 10 % for phase envelopes and 5 % for speed of sound. Nevertheless, their results must be taken with care due to the lack of experimental data for the mixtures at cryogenic conditions. Recently, von Preetzmann and Span published density measurements of two helium-neon mixtures at six isotherms ranging from 100 K to 233 K [94]. As Tkaczuk et al. have focused on the VLE representation, deviations to the new density data up to 2.7 % are observed.

Another approach is the multiparameter EoS of Huang et al. [19] for helium-3 which they called the Debye EoS. They stipulate a density-dependent Debye-temperature to model the cubic temperature-dependency of the heat capacity in the low-temperature regime. The terms accounting for the accurate representation of different properties (i.e. very low temperatures, ideal gas limit, second virial coefficient etc.) are turned on and off using Fermi functions $f(x) = (1 - \exp x)^{-1}$. Thus, their EoS is a semi-empirical EoS which has a physical basis in the low-temperature regime. However, a full perturbation theory based on the low-temperature limit, i.e. the third law of thermodynamics

$$\lim_{T \to 0} c_V = 0 \tag{2.120}$$

is yet to be developed.

In conclusion, cubic EoS, multiparameter EoS and EoS based on perturbation theory can be modified to incorporate some but not all effects arising from the quantum behaviour of helium, hydrogen and neon. For their (multi-component) mixtures with higher boiling substances, the use of 'classical' critical parameters is a good option to model the fluid behaviour with classical state-of-the-art EoS. For cubic EoS, established consistency criteria must be breached to reach acceptable representation of available experimental data at cryogenic conditions. Quantum swelling and its influence on perturbation terms have been introduced into 'classical' SAFT-type approaches. Nevertheless, the theories still rely on classical radial distribution functions and classical limits far from cryogenic temperatures. Only multiparameter EoS do not rely on this physical basis, but on a broad experimental data base. All EoS aiming to describe the behaviour of cryogenic mixtures would benefit from more accurate data, particularly from caloric data.

3. Measurement of fluid properties

The development of EoS requires precise data of fluid phase equilibria, densities and caloric properties. Transport property measurements play a tangential role in EoS parametrisation, but they are required for correlations, which are crucial to equipment dimensioning. In this chapter, state-of-the-art measurement methods allowing the measurement of phase equilibria, caloric properties and transport properties are introduced. A focus is set on implications of an operation at cryogenic conditions. Therefore, a literature review of test benches operated at temperatures below 50 K with the cryogens helium, hydrogen or neon is presented.

3.1. Experimental methods for the measurement of fluid phase equilibria

The measurement of phase equilibria comprises determination of pressure, temperature and composition of all but one phases in equilibrium. The composition of the remaining phase can be determined using the Gibbs-Duhem equation. Additional measurement of the remaining phase composition enables thermodynamic consistency tests according to section 2.2. According to Gibbs' phase rule, a system in vapor-liquid equilibrium has as many degrees of freedom as components. For a mixture of constant total composition, i.e. a closed system, either the temperature or the pressure must be set, for the other quantity to follow. For the thermodynamic treatment of the data, isothermal data is advantageous as explained in chapter 2. Fortunately, isothermal methods require less experimental effort than isobaric methods, because no circulation loop is required. Isothermal methods only require to thermally stabilise a closed volume. Therefore, the following section deals with isothermal methods for phase equilibria measurement.

Dohrn et al. have developed a classification for experimental methods for the measurement of fluid phase equilibria [95]. When an equilibrium cell is filled with a mixture of known composition and does not require composition analysis in equilibrium, the experimental method is called synthetic. The mixture is brought to equilibrium conditions and changes in the phases are observed as functions of temperature and pressure. For example, a gas mixture is cooled down until the first liquid drop appears. In this case, the synthesised mixture composition is assumed to represent the vapor phase composition in equilibrium. Since either boiling or dew points are measured, the charged load must either correspond to an equilibrium cell completely filled with vapor or liquid. To allow thermodynamic consistency testing, both points have to be measured, which requires knowledge about the equilibrium composition beforehand. The detection of a phase change can be visual, or by measurement of other quantities such as thermal slope changes during cooling or different kinds of spectra [95].

Experimental methods with initially unknown composition, which require an analysis of the phases in equilibrium, are called analytical. The composition is either analyzed outside of the equilibrium cell after taking samples of the phases, or in-situ by spectroscopic methods. Samples are usually analysed chromatographically. The sampling process must not disturb the established phase equilibrium, which only allows small sample volumes compared to the cell volume. Contrary to synthetic methods, there is not necessarily a dominant phase containing most of the substance. Consequently, the coexisting phases must be brought into contact by agitation in order to reach fast equilibration. For this purpose, stirrers or re-circulation of one or two phases are used. However, stirrers have some disadvantages for low temperature and high pressure test stands:

- abrasion of the stirrer coating blocking sampling capillary entries,
- introduction of heat and
- either a mechanical feedthrough or a high external magnetic field.

Re-circulation introduces heat into the cell as well, though it can be minimised by pre-cooling of the entering fluid. For test benches operated at cryogenic conditions, high magnetic fields can be reached with superconductors. But high currents might interfere with other high accuracy electrical components, such as wiring and temperature sensors, and it makes the test bench more complex than a re-circulation loop.

All experimental methods require a thermally stable environment. Particularly, isothermal methods rely on a controlled environment around the equilibrium cell. The equilibrium cell temperature must be

- controllable within the uncertainty of the temperature sensors,
- stable,
- homogeneous,
- and representative for the fluid temperature.

Test benches which have been operated below the triple point of nitrogen are listed in Table 3.1. The classification of the experimental methods by Dohrn et al. is given in Table 3.2 [95]. Several cooling methods have been used, which mostly rely on a liquid bath of a cryogen below or around the equilibrium cell. Depending on the temperature range, helium, hydrogen, neon can be used. The equilibrium cell is in thermal contact with either the liquid itself (called immersion in cryogen bath in Table 3.1) or its (circulating) vapor. The cryogen bath is kept at ambient pressure (called vapor cooling in Table 3.1) or its temperature is controlled by pressurisation (called vapor pressure control in Table 3.1). The equilibrium cell is equipped with compensation heaters to fine-tune its temperature. There is one test bench whose equilibrium cell has been cooled by a helium refrigerator in a high vacuum cryostat [96]. This set-up enables continuous operation of the test bench without the need of refilling a cryogen bath. The authors reported a temperature stability of ±10 mK, which is comparable to the stabilities reported for the other test benches. However, they observed a vertical temperature gradient of 100 mK in their equilibrium cell. This check for homogeneity was not addressed or not considered necessary in the other publications.

Table 3.1.: Literature review on cryogenic phase equilibria test stands indicating their cooling method, classification, publications, fluid systems and their maximum reported pressure p_{max}.

Test bench location	Cooling method	Classification of Dohrn et al. [95]	Publications	Systems studied	p_{max} in bar
Wayne State University, USA	Vapor cooling	AnT+Cap+MS	Roellig and Giese (1962) [97]	He-H$_2$	7
United States Military Academy, West Point, USA	Vapor pressure control	AnT+Cap+Vcir+TCD	Streett and Jones (1964) [98]	H$_2$-Ne	104
University of Leiden (1), Netherlands	Vapor pressure control	SynVis	Brouwer et al. (1964) [99]	D$_2$-Ne	1
University of Michigan, USA	Vapor pressure control	AnT+Cap+Vcir+MS	Streett et al. (1965) [100] Sonntag et al. (1964) [101] Sneed et al. (1968) [102]	He-nH$_2$ He-H$_2$ He-H$_2$	100
University of Colorado, USA	Vapor cooling	AnT+Cap+Vcir+GC	Heck and Barrick (1966) [13]	He-Ne	201
German Academy of Sciences at Berlin, Germany	Immersion in cryogen bath	AnT+GC	Knorn (1967) [14]	He-Ne	51
University of Leiden (2), Netherlands	Vapor cooling	SynNon	Van't Zelfde and Dokoupil (1974) [103]	H$_2$-Ne	2
National Bureau of Standards, USA	Vapor cooling	AnT+Cap+Vcir+GC	Hiza (1981) [104]	He-nH$_2$ He-nD$_2$	200
Japan Atomic Research Institute, Japan	Cryogen-free refrigerator	AnT+Val+Vcir+GC	Yamanishi et al. (1992) [96]	He-nH$_2$ He-HD He-nD$_2$	6

Table 3.2.: Abbreviations used in the classification of phase equilibria test stands according to Dohrn et al. [95].

Abbreviation	Meaning
AnT	Analytical isothermal method
Cap	Sampling through capillaries
GC	Analysis by gas chromatography
MS	Analysis by mass spectroscopy
SynNon	Synthetic non-visual method
SynVis	Synthetic visual method
TCD	Analysis by thermal conductivity measurement
Val	Sampling using a special valve
Vcir	Vapor phase re-circulation

3.2. Experimental methods for the measurement of caloric properties

For the development of EoS based on fundamental equations for the extensive quantities, such as Gibbs energy or Helmholtz energy, direct measurement of enthalpy and entropy would be ideal. Unfortunately, only derivative properties are accessible through measurement. These caloric properties are the heat capacity, the Joule-Thomson coefficient and the speed of sound. They are defined by the derivatives

$$\tilde{c}_p = \left(\frac{\partial \tilde{h}}{\partial T} \right)_p , \tag{3.1}$$

$$\tilde{c}_V = \left(\frac{\partial \tilde{u}}{\partial T} \right)_{\tilde{V}} , \tag{3.2}$$

$$\mu_{\text{JT}} = \left(\frac{\partial T}{\partial p} \right)_{\tilde{h}} , \tag{3.3}$$

$$w^2_{\text{sound}} = \left(\frac{\partial p}{\partial \tilde{\rho}} \right)_{\tilde{s}} , \tag{3.4}$$

where the tilde denotes mass-specific quantities. In principle, any of these caloric properties can be measured and used for EoS parameter fitting because they depend on each other through derivatives of a thermal EoS

$$\tilde{c}_p = \tilde{c}_V - T \left(\frac{\partial p}{\partial T} \right)_{\tilde{v}}^2 \left(\frac{\partial p}{\partial \tilde{v}} \right)_T^{-1}, \tag{3.5}$$

$$\mu_{\mathrm{JT}} = \frac{1}{\tilde{c}_p} \left(T \left(\frac{\partial \tilde{v}}{\partial T} \right)_p - \tilde{v} \right), \tag{3.6}$$

$$w_{\mathrm{sound}}^2 = \left(\frac{\partial p}{\partial \tilde{\rho}} \right)_T + \frac{T}{\tilde{\rho}^2 \tilde{c}_V} \left(\frac{\partial p}{\partial T} \right)_{\tilde{\rho}}^2. \tag{3.7}$$

However, first and second derivatives of the thermal EoS add uncertainty to the calculated quantity. Therefore, an accurate thermal EoS is as important as a precise caloric property measurement.

3.3. Measurement of speed of sound

Out of the four properties, the speed of sound can be measured with the lowest uncertainty. Depending on the fluid regime, two acoustic experimental approaches can be distinguished: Interferometer and pulse-echo methods [105].

For the interferometer method, a transducer emitting sound waves and a receiver are placed in a certain, precisely known distance. The emitted frequency is adjusted until the incident and the reflected waves interfere forming a standing wave. It is also possible to alter the distance instead of the frequency for a standing wave to form. These resonant states yield the highest signal amplitude on the receiver. The speed of sound is determined from the frequency difference Δf of two adjacent standing wave modes

$$w_{\mathrm{sound}} = 2L\Delta f \tag{3.8}$$

at a distance L. For the pulse-echo-method, the set-up consists of a spherical cell with precisely known dimensions and a piezoelectric crystal disk, which is located off-center in the cell. This piezoelectric crystal serves as emitter and receiver of acoustic waves. It is connected to a wave generator and an oscilloscope. When the disk is excited by a burst, a sound wave is generated on both sides of the disk. Since it is off-centered, the two sound waves have different path lengths and are received at different time instances. The speed of sound is determined through

$$w_{\mathrm{sound}} = \frac{2\Delta L}{\Delta t}, \tag{3.9}$$

with ΔL being the path length difference and Δt the delay in the time of flight.

For both methods, precise measurement of a distance is required. The cell dimensions can be measured manually after manufacture at well known conditions. More precisely, it can be calculated with reference fluids of very precisely known speed of sound, such as

water or argon. Based on the measured dimensions at a parameter set $\{p, T\}$, they can be calculated including thermal expansion and mechanical stress at the desired temperature and pressure.

A key parameter for the choice of method is the acoustic impedance of the fluid. While solids, such as resonator walls or transducers, have a typical acoustic impedance of $10^7\,\mathrm{Ns/m^3}$, liquids have a typical acoustic impedance of $10^6\,\mathrm{Ns/m^3}$ and gases $10^2\,\mathrm{Ns/m^3}$ [106]. The difference of the acoustic impedances at a solid-fluid interface affects the transmission/reflection characteristics of an incoming sound wave. For identical acoustic impedances, the wave is transmitted without reflection loss. Since the pulse-echo method requires a high transmission into the receiver element, it is mainly used for measurements of gases. The interferometer method, which relies on high reflection to build a standing wave, is used for measurements of liquids.

In general, excitation amplitudes and frequencies should be low enough for the acoustic wave propagation to be isentropic [31]. Otherwise, the measured speed of sound does not correspond to the thermodynamic speed of sound defined by Equation 3.4. Experimental challenges arise at low temperatures, because the conversion of electrical to mechanical excitation in piezoelements scales with temperature. Furthermore, the acoustic impedance of the piezoelements and the fluid should match in order to gain high signal-to-noise ratios. The impedances can be matched using different coatings on the element. Similar effects arise for the electrical equipment in the measurement chain requiring electrical impedance matching, i.e. all cables and connectors having the same impedance. For low temperatures, the precise measurement of the cell dimensions is challenging, since the operation temperatures are far from the reference points and the uncertainty of the properties of the cell material increases.

Two authors have measured the speed of sound of cryogenic fluid mixtures. Pashkov et al. have investigated liquid helium-neon mixtures from 27 K to 39 K up to pressures of 148 bar using a pulse-echo based method [107]. The claimed uncertainty of the speed of sound is $\pm 0.1\,\%$. Also, they have investigated the pH_2-He system from 18 K to 27 K up to pressures of 100 bar. Unfortunately, no details about the experimental set-up are given in their publication. Gusewell et al. have measured the speed of sound of liquid neon-hydrogen and neon-deuterium mixtures from 25 K to 31 K with uncertainties ranging from $\pm 0.5\,\%$ to $\pm 1\,\%$ using a pulse-echo based method [108, 109]. They have used two piezoceramic plates inside of an equilibrium cell, which was immersed in liquid hydrogen. They have swept the excitation frequency around the resonance frequency of the piezoelements to obtain a resonance interference.

Another method to measure the speed of sound of fluids is dynamic light scattering (DLS) [110]. This method is introduced in section 3.6.

3.4. Measurement of Joule-Thomson coefficient

The Joule-Thomson coefficient is accessible through measurement of two temperatures and pressures. For small pressure drops, the partial derivatives in Equation 3.3 can be replaced by the measurands at the inlet and the outlet of an adiabatic capillary or orifice

$$\mu_{JT} = \left(\frac{\partial T}{\partial p}\right)_{\tilde{h}} \approx \left(\frac{T_{\text{inlet}} - T_{\text{outlet}}}{p_{\text{inlet}} - p_{\text{outlet}}}\right)_{\dot{Q}_{\text{axial+ambience}}=0}. \tag{3.10}$$

Depending on the experimental set-up, axial heat transfer along the capillary or orifice as well as heat transfer to or from the surrounding must be taken into account. Equation 3.10 does not stand at high pressure drops for two reasons: First, the Joule Thomson coefficient is a (non-linear) function of temperature and pressure $\mu_{JT} = f(p, T)$. Furthermore, high pressure drops induce higher temperature gradients, which might lead to heat transfer violating the isenthalpic condition. The measurement of the Joule-Thomson coefficient cannot be done with sufficient precision in order to fit reliable EoS parameters. Particularly at cryogenic temperatures, thermal effects cause erratic behaviour as can be seen by Tkaczuk, who has measured the Joule-Thomson coefficient of helium-neon and helium-nitrogen mixtures from 50 K to 100 K with an uncertainty of ±9 % and inexplicable deviations to his multiparameter EoS [111]. Nevertheless, the Joule-Thomson coefficient is a crucial parameter for the design of cryogenic mixed refrigerant cycles, since they contain a Joule-Thomson valve. Also, the inversion curve ($\mu_{JT} = 0$) is an important criterion for the feasibility of the process, as it defines the maximum throttle inlet temperature for a cooling effect to take place. Therefore, the derivation of the Joule-Thomson coefficient from an EoS must yield reliable results imposing additional uncertainty requirements on the measurement of other caloric properties.

3.5. Measurement of heat capacity

The measurement of the heat capacity of a fluid involves measurement of the temperature rise induced by a known amount of added energy either under isochoric or isobaric conditions. Isochoric instruments consist of a constant volume cell containing a known amount of fluid. For high accuracy, knowledge of the cell dimensions and the material properties, i.e. thermal expansion and heat capacity, is crucial. The cell must be thermally isolated from any parasitic heat input in order to trace a temperature rise back to a controlled heat input. This input is usually provided by an electrical heater, which is turned on for a specific time

$$\Delta U = M\tilde{c}_v \Delta T = \int \dot{Q} \mathrm{d}t = \int \dot{P}_{\text{electric}} \mathrm{d}t. \tag{3.11}$$

The added energy must be sufficiently low, to correspond to a certain thermodynamic state $\{p, T, z\}$, but sufficiently high to yield temperature increases beyond measurement uncertainty, particularly considering the heat capacity of the cell. For liquids, the temperature increase must not lead to partial evaporation. Instruments for the measurement

of isochoric heat capacities of fluids at cryogenic temperatures have been developed by Hoffer for liquid helium [112] and Gladun for liquid neon [113]. Gladun used a stainless steel cell with a volume of $75\,\mathrm{cm}^3$ suspended in a vacuum container. He calibrated lead temperature sensors using vapor pressure thermometry and the vapor pressure measurements of neon of Grilly [114]. The adiabatic condition is maintained by two surrounding shields operated within $\pm 0.02\,\mathrm{K}$ of the cell. With this set-up, Gladun stipulates relative uncertainties of the specific heat capacity of $0.1\,\%$ to $1\,\%$. Brouwer et al. measured the heat capacity of neon-hydrogen mixtures at cryogenic temperatures [115]. Their set-up consisted of a calorimeter cell suspended in a vacuum container in a liquid hydrogen bath. The cell is equipped with a heating coil, a Germanium temperature sensor and a stirrer. The characteristic heat input by the stirrer is separately measured and considered for the heat capacity calculations. They also considered partial evaporation during the heating steps. An accuracy of $5\,\%$ is estimated.

None of the literature sources report directly measured heat capacities at constant pressure. Reported values are either derived from speed of sound measurements or from isochoric heat capacities using a thermal EoS. In principle, the isobaric heat capacity can be measured by a controlled heat supply into a constant fluid flow and temperature measurements at the inlet and the outlet of the heater element. This measurement principle equals the one of a thermal mass flow meter with the measurement output being the heat capacity instead of the mass flow. Thus, the specific heat capacity at constant pressure can be measured by a combination of a thermal mass flow sensor and another mass flow sensor working independently of heat capacities, e.g. a Coriolis mass flow sensor. The heat capacity at constant pressure is determined through the temperature increase $\Delta T_{\mathrm{thermal}}$ induced by a heat input $\dot{Q}_{\mathrm{thermal}}$ and the mass flow $\dot{M}_{\mathrm{Coriolis}}$

$$\tilde{c}_p = \frac{\dot{Q}_{\mathrm{thermal}}}{\dot{M}_{\mathrm{Coriolis}}\Delta T_{\mathrm{thermal}}}. \qquad (3.12)$$

The obtained specific heat capacity is a function of pressure, temperature and composition of the fluid. With negligible pressure drops along the thermal mass flow sensor and small temperature increases, its accuracy can be correlated to the uncertainties of temperature, pressure and mass flow measurement.

In a previous work at the Institute of Technical Thermodynamics and Refrigeration, a thermal mass flow sensor operating at cryogenic temperatures has been developed based on a publication of Grohmann [116]. It is equipped with a heating element and a temperature sensor at the inlet, the outlet and the heating element itself. Two characteristic temperature differences

$$\Delta T_{\mathrm{in}} = T_{\mathrm{heater}} - T_{\mathrm{inlet}} \qquad (3.13)$$

$$\Delta T_{\mathrm{out}} = T_{\mathrm{heater}} - T_{\mathrm{outlet}} \qquad (3.14)$$

can be defined. As a main feature, it eliminates systematic errors by evaluating the results using the first law of thermodynamics

$$\dot{Q} = \dot{M} c_p \left(\Delta T_{\text{in}} - \Delta T_{\text{out}} \right) \tag{3.15}$$

$$\tilde{c}_p = \frac{\dot{Q}}{\dot{M} \left(\Delta T_{\text{in}} - \Delta T_{\text{out}} \right)} \tag{3.16}$$

in combination with kinetics

$$\dot{Q} = \frac{1}{R_{\text{th}}} \frac{\Delta T_{\text{in}} - \Delta T_{\text{out}}}{\ln \frac{\Delta T_{\text{in}}}{\Delta T_{\text{out}}}} \tag{3.17}$$

$$\tilde{c}_p = \frac{1}{\dot{M} R_{\text{th}}} \frac{1}{\ln \frac{\Delta T_{\text{in}}}{\Delta T_{\text{out}}}} \tag{3.18}$$

If the thermal resistance of the heater R_{th} is independent of heat flow, a step-wise increase of the heater power, resulting in increased temperature differences, allows determination of this resistance [116]. By minimisation of the errors of temperature and power measurement, the systematic errors are eliminated and the resulting heat capacity has an uncertainty in the same range as temperature, pressure and mass flow measurements. Further details on the cryogenic mass flow sensor can be found in [117]. A flow diagram of this measurement concept is shown in Figure 3.1.

3.6. Experimental methods for the measurement of transport properties

The macroscopic measurement of transport properties involves measurement of a flow along a gradient

$$\dot{j}_{\text{mass}} = -\delta \frac{\mathrm{d}n}{\mathrm{d}L}, \tag{3.19}$$

$$\dot{j}_{\text{momentum}} = -\eta \frac{\mathrm{d}w}{\mathrm{d}L}, \tag{3.20}$$

$$\dot{j}_{\text{heat}} = -\lambda \frac{\mathrm{d}T}{\mathrm{d}L}, \tag{3.21}$$

with δ being the diffusivity, η the viscosity and λ the thermal conductivity. Hence, a non-equilibrium state must be created, which is sufficiently disturbed from equilibrium for the macroscopic gradient to be measured. If it is disturbed too far from equilibrium, the integrally measured property can only be assigned to a certain thermodynamic state with poor resolution. Therefore, measurement methods based on microscopic gradients have been developed allowing measurements in macroscopic equilibrium [110].

Every bulk fluid is subjected to microscopic fluctuations in mole fractions, pressure and temperature. The decay process of these fluctuations corresponds to the respective gradient and depends on the respective coefficient. Furthermore, the speed of sound can
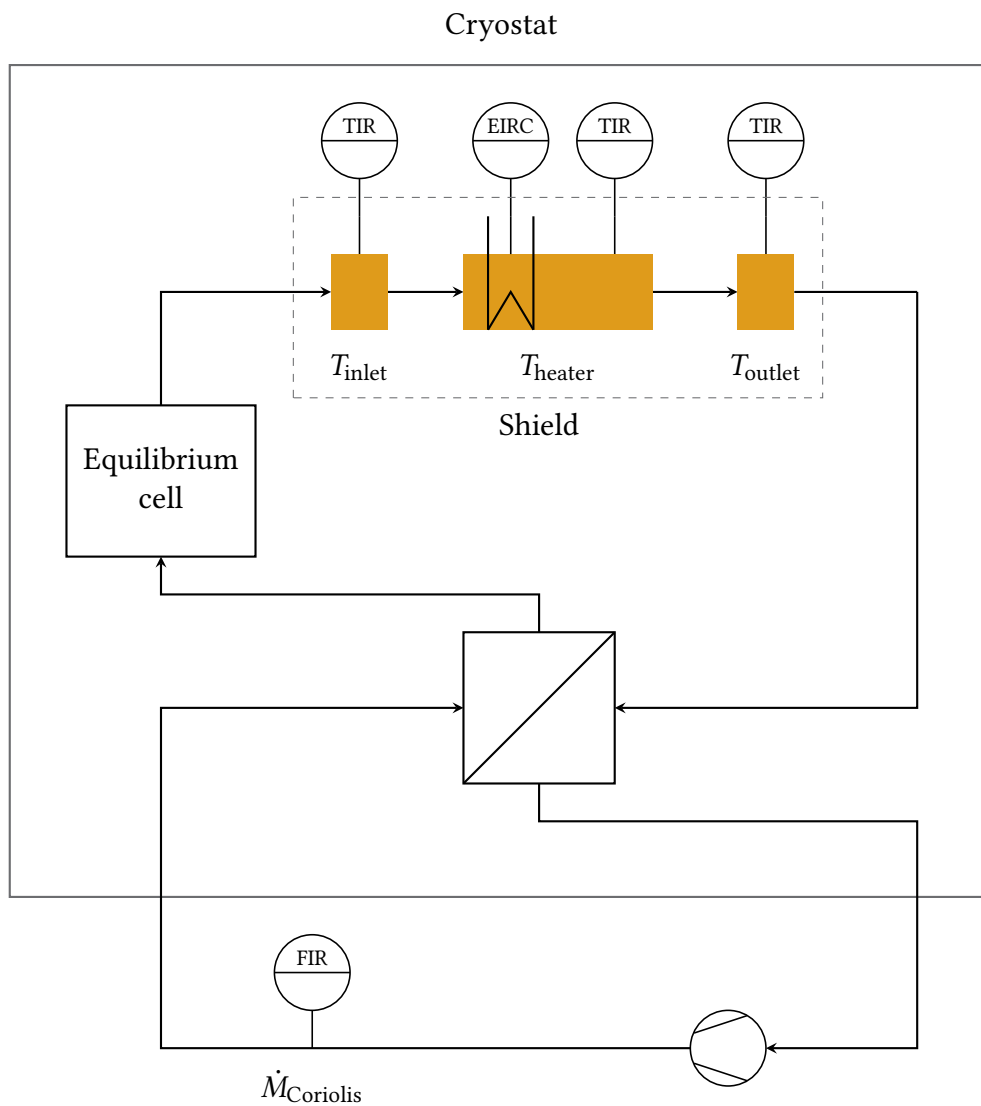
Cryostat

Figure 3.1.: Concept of a measurement method for the heat capacity of the vapor phase combining a cryogenic thermal mass flow sensor with a Coriolis mass flow sensor at ambient temperature in an existing vapor phase re-circulation loop of a phase equilibria test stand.

be obtained from the pressure fluctuations, because it corresponds to the speed of the wave propagation while its decay of the amplitude depends on the viscosity.

The fluctuations cause light scattering, when the fluid is irradiated by coherent laser light. The modulation of the scattered light can be measured and correlated. The correlation functions contain a characteristic correlation time, which corresponds to the thermal diffusivity if the scattered light is superimposed with a coherent reference light source, and to the sound attenuation constant if the scattered light is superimposed with a frequency shifted reference light source. The speed of sound can be obtained from the required frequency shift. These measurements are called dynamic light scattering. If the surface of a liquid is irradiated, the surface waves contain information about the surface tension as well as the kinematic viscosity of the fluid. This method is called surface light scattering. A detailed description of dynamic light scattering methods for the measurement of fluid transport properties is given in [110].

Both methods require measurement of the scattered light under certain angles to the incident laser beam. Therefore, an equilibrium cell must be designed with optical access for the incident beam and the scattered light. The window must be sufficiently wide to allow adjustements of the incident and the observant angles of the beams. The window material must not be birefringent to be independent of the polarization and incident beam orientation. Unfortunately, sapphire glass, which is a popular choice for low-temperature applications due to its high thermal conductivity, is birefringent. Thus, other materials, such as quartz, must be used.

In the literature, only macroscopic measurement methods have been used at cryogenic temperatures. Ubbink and de Haas used a parallel-plate method to measure the thermal conductivity of low-density gases at cryogenic temperatures [118]. Two plates are installed at a distance L from each other and cooled/heated to different temperatures. The space between the two plates is filled with the fluid of interest. The heat required to keep a constant temperature difference between the two plates is measured. Radiation, heat losses from the plate at high temperature, and the Kapitza resistance at the solid-fluid interface affect the accuracy of the experimental results. Diller and Roder used a similar apparatus for the measurement of thermal conductivity of liquid and gaseous hydrogen from 17 K to 198 K [119].

4. Description of the apparatus

The development of a test bench for the measurement of cryogenic fluid properties consists of three work packages:

- Conceptualisation, design, construction and commissioning of a test stand for phase equilibria measurements,
- an upgrade of the test stand with a measurement method for the specific heat capacity of the fluid mixture, and
- an upgrade of the test stand with an optical set-up for dynamic light scattering experiments to measure transport properties.

This thesis deals with the first work package, while making provisions for the other two work packages in the design of the test bench. The main goal is to provide data for reliable modeling of the properties through an EoS and transport property correlations required for the design of cryogenic mixed refrigerant cycles.

4.1. General

Based on the state-of-the-art experimental methods presented in chapter 3, the following concept has been chosen: An equilibrium cell with optical access is cooled down to a constant temperature enabling precise VL(L)E measurements. The cooling power is provided by a pulse-tube cryocooler, allowing experiments independent of liquid cryogen consumption. The operation temperature ranges from the triple point of hydrogen (14 K) to room temperature. The calibration effort for multi-component mixtures makes spectroscopic composition analysis infeasible, although possible with optical access. Therefore, phase composition is determined through sampling and GC analysis. The cryostat shall allow for re-circulation of the vapor phase, whose heat capacity is measured by a combination of a thermal mass flow sensor at cryogenic temperature and a Coriolis mass flow meter at ambient temperature as described in chapter 3. The optical access allows dynamic light scattering experiments to obtain transport properties. The use of a cryocooler is additionally motivated by the absence of evaporating cooling liquid possibly interfering with the DLS experiments.

With this set-up, the test stand allows the measurement of phase equilibria, heat capacities and transport properties. The main concept of the set-up and initial commissioning results have been published in [120, 121]. It cannot provide density or speed of sound data as vapor-phase re-circulation does not allow a precise determination of dimensions/volumes. These two properties are currently subject to experimental investigations by Span and coworkers in the context of EoS development for efficient hydrogen liquefaction [122].

In the following sections, the cryogenic phase equilibria test stand (CryoPHAEQTS) is presented in detail.
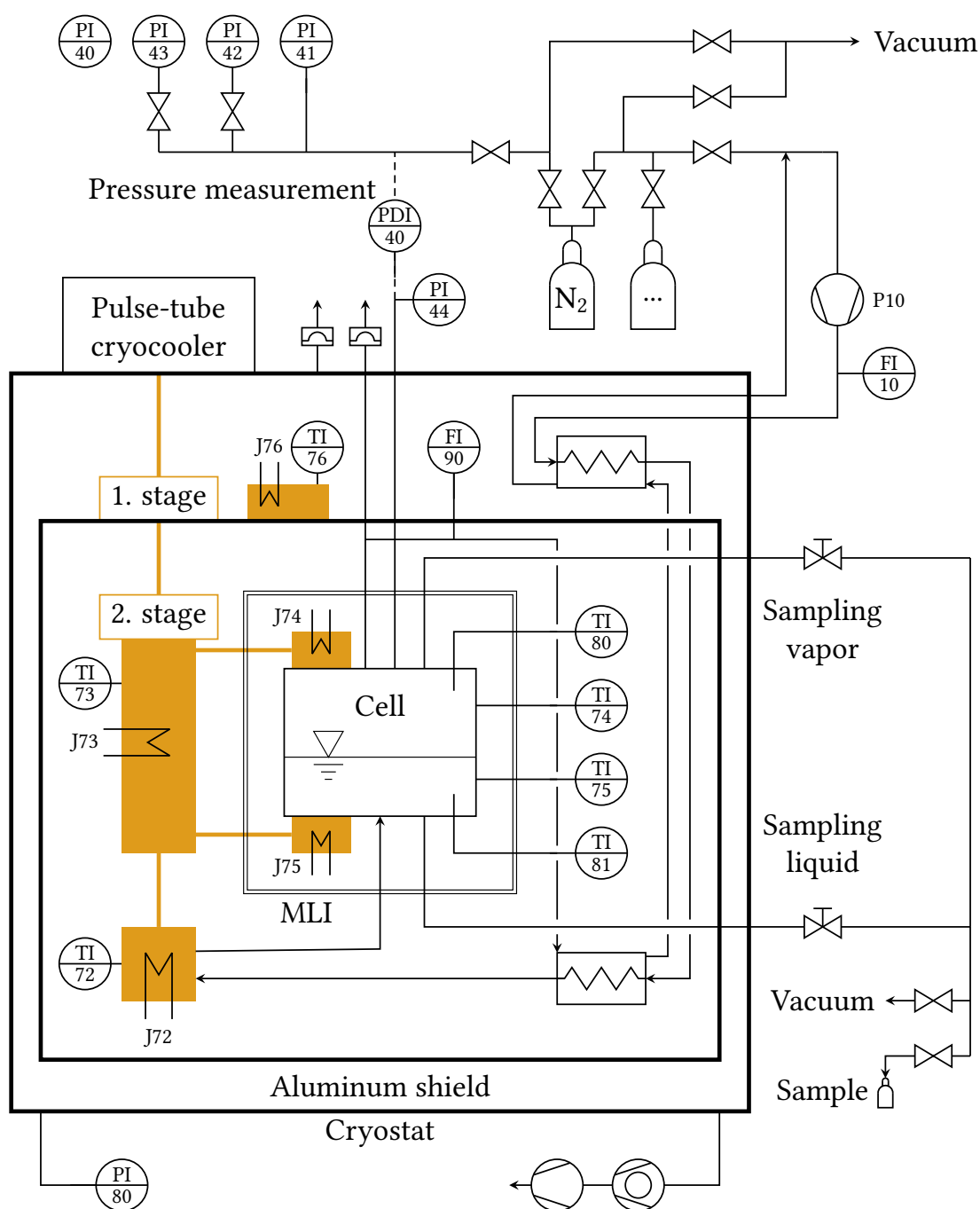
Figure 4.1.: Piping and instrumentation diagram of CryoPHAEQTS adapted from [123].

4.2. Process design

The main components of CryoPHAEQTS are shown in the piping and instrumentation diagram of the test stand in Figure 4.1.

The equilibrium cell is connected to a circulation loop consisting of two tube-in-tube heat exchangers, a gas circulator (P10), a Coriolis mass flow sensor (FI10) and a pre-cooling tube coil around a copper block of E-CU grade (J72). The gas is circulated by a HMZ 020 gas circulator supplied by Fink Chem+Tec offering a maximum flow of $400 \, \mathrm{L \, h^{-1}}$. This gas circulator uses conveyor plates made of graphite. Two filters are installed before and after the gas circulator to prevent the graphite abrasion from entering other equipment. The mass flow is measured by a Mini Cori-Flow M13 mass flow sensor supplied by Bronkhorst AG. It can be adjusted by a frequency inverter in a range from $0 \, \mathrm{Hz}$ to $50 \, \mathrm{Hz}$. The fluid conveyed by the gas circulator enters the cryostat through a high-vacuum feedthrough and is cooled against the fluid in the suction line. The tube-in-tube heat exchangers consist of an outer pipe with 10 mm outer and 8 mm inner diameter and an inner pipe with 6 mm outer and 4 mm inner diameter with a length of 5 m, respectively. Before entering the equilibrium cell, the temperature of the fluid stream is adjusted to about 100 mK above the equilibrium cell temperature to avoid thermal disturbances in the cell. Also, premature condensation of the fluid outside of the equilibrium cell is avoided. The connecting tube from the pre-cooling block to the equilibrium cell is bent in a siphon-like manner to avoid liquid back-flow at stillstand of the gas circulator. At the outlet of the equilibrium cell, there is sufficient space for the future upgrade of the test stand with a cryogenic thermal mass flow sensor (FI90). The other cell outlet is connected to the safety line leading to the bursting disc on top of the cryostat cover.

The circulation loop is connected to a valve panel allowing venting and evacuation of the loop. Gas cylinders are stored in two gas cylinder cabinets in the laboratory. Feedthroughs connect the valve panel with the pressure regulators in the cabinets. For gases, which cannot be stored in the cabinets, the valve panel has an additional coupling.
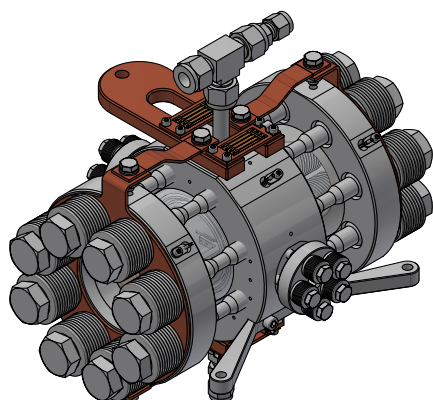
4.3. Equilibrium cell design

The equilibrium cell has been designed with the following constraints:

- Temperature range: 14 K to 300 K,
- Pressure range: 0 bar to 151 bar,
- He-leak tightness: $10^{-8} \, \mathrm{mbar \, L \, s^{-1}}$,
- Thermal access for connection to the cryocooler,
- Three sampling capillaries allowing VLLE measurements (only 2 of them are shown in Figure 4.1 for clarity,
- Optical access by opposing and right-angled windows, and
- Entry and exit apertures for vapor re-circulation.

The cell details have been designed in close collaboration with Michael Stamm, who also provided the mechanical design drawings shown in Figure 4.2.

The cell consists of a main cylinder made of 1.4571 steel with an outer diameter of 130 mm and an inner diameter of 50 mm. Loose flanges press two sapphire windows against the open front sides of the cylinder forming an enclosed volume of 100 mL. To ensure leak-tightness in the whole temperature and pressure range, stress bolts in combination with a plate spring stack of 10 springs are used. Each stack consists of two packs of 5
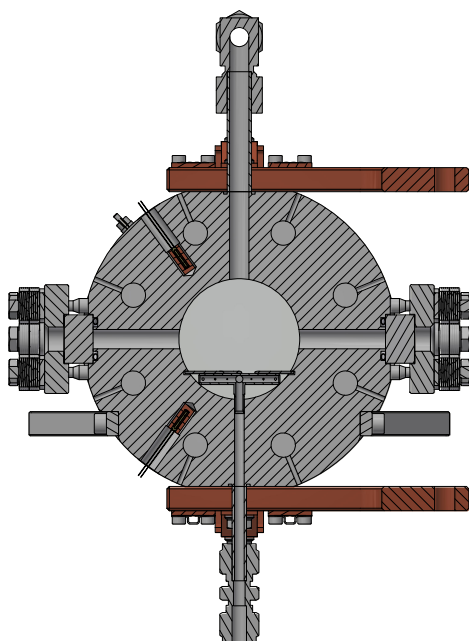
(a) 3D isometrical drawing of the equilibrium cell.
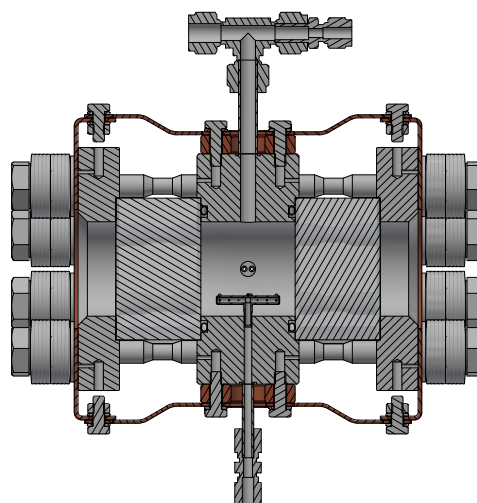
(b) Horizontal cut through the equilibrium cell.

(c) Vertical cut through the equilibrium cell.
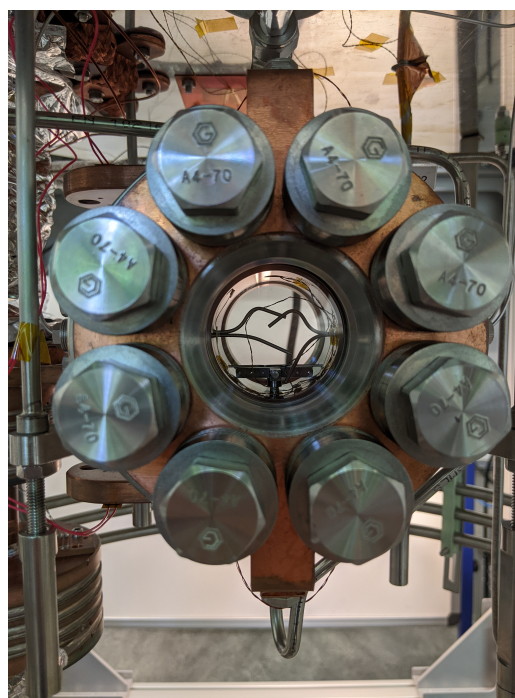
(d) Front side picture of the equilibrium cell.

Figure 4.2.: Equilibrium cell design.

springs each, which are arranged opposite of each other. The interface between the cell and the windows is sealed with Helicoflex® gaskets.

The main cylinder is oblated on 4 sides, allowing the installation of two copper forks on the top and the bottom of the cell, as well as another two sapphire windows, which are right-angled to the front side ones. In the current design, the two small windows

are replaced by capillary feedthroughs for capillaries penetrating into the cell. They are bent to sample from different heights inside the cell. In the initial design, the sampling capillaries were soldered into bore holes through the cell walls. Unfortunately, the solder connections started to leak requiring a re-design without these solder connections. Also, quartz glass windows had been used during the first commissioning, but they could not withstand the thermal stress during warm-up and cool-down. As the thermal conductivity and expansion coefficient of sapphire glass is closer to the values of steel than quartz glass, the window material has been changed. To further reduce thermal stress in the windows, the loose flanges are thermally connected to the copper forks on top and bottom of the cell. The quartz glass windows have not been tested with these thermal connections. Hence, the modified set-up could comply with the requirements of the DLS upgrade of the test stand. The copper forks serve as thermal connectors to the cryocooler via copper braids as well. They can be heated individually by two heating foils. Also, the forks offer a flat surface for thermal anchoring of temperature sensor wiring. Two temperature sensors can be installed in two bore holes in the cell wall, which are representative for the top and bottom cell temperatures.

The four steel bars protruding from the cylinder serve as mount for the suspension of the cell. A pipe with an inner diameter of 4 mm is connected to the entry on the bottom of the cell. Fluid can leave the cell through a pipe with an inner diameter of 8 mm on top of the cell. The larger diameter guarantees a safe discharge of fluid in case of an uncontrolled pressure increase. It also serves as inlet for the wiring of temperature sensors inside the cell. A cross piece is fixed on top of the entry aperture by a clamping bracket to disperse the entering gas in the liquid phase(s).

4.4. Cryostat design

The equilibrium cell is enclosed in a cryostat in order to reach and maintain cryogenic conditions. The cryostat shown in Figure 4.3 consists of a stainless steel vacuum chamber with an outer diameter of 700 mm, a height of 650 mm and a coverflange with a diameter of 950 mm. It offers optical access through four opposing windows on the cylinder. The cover contains all electrical feedthroughs for measurement and control as well as feedthroughs for circulation, sampling, pressure sensing and evacuation piping. The cryostat is protected against over-pressure by a bursting disk set at 1.5 bar. However, the free volume of the cryostat is designed to take up all fluid in case of a burst in the circulation loop without exceeding 1.4 bar.

The equilibrium cell is suspended from the cover by 4 hollow steel rods. It is surrounded by 2 radiation shields: A high-temperature (HT) shield, which is connected to the first stage of the cryocooler by 12 copper braids, and a low-temperature (LT) shield, which is connected to the second stage of the cryocooler by 2 copper braids. Both shields are made of aluminum and have slit openings to allow optical access. The low-temperature shield is mounted on the equilibrium cell suspensions. It is covered in ten layers of super-insulation. The high-temperature shield is suspended from the cover of the cryostat by three fiberglass-reinforced plastic rods. The main cryostat components and shield are shown in Figure 4.4.
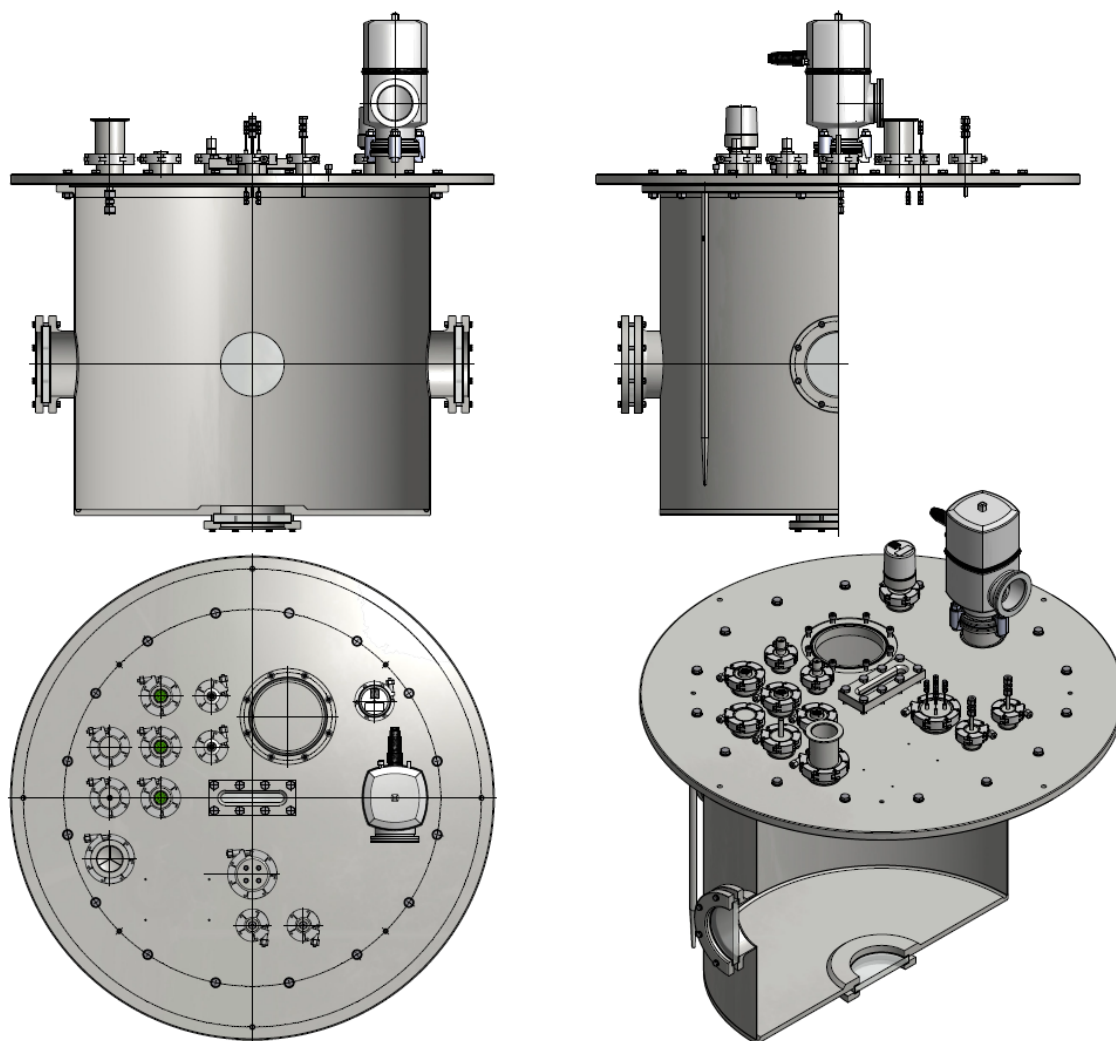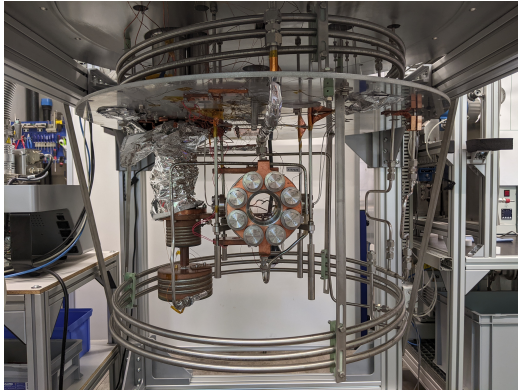
Figure 4.3.: Mechanical design drawing of the cryostat.

(a) Main components inside of the cryostat.

(b) Low-temperature shield covered by multi-layer insulation.

(c) High-temperature aluminum shield.

(d) Vacuum container with guiding rods.

Figure 4.4.: Pictures of the main cryostat components and shields.

4.5. Heat load budget

Cooling power is provided by a two-stage pulse-tube cryocooler PT-810-RM supplied by Cryomech Inc. The zero load temperatures are 30 K for the first and 7 K for the second stage. Assuming a temperature difference of 2 K between the cryocooler and the equilibrium cell, the required temperature of the second stage is 12 K. At this temperature, it provides a cooling power of 10 W, while the first stage offers 50 W at a temperature of 70 K. To assess the thermal feasibility of the chosen cryocooler, the heat loads into the two stages must match the heat load budget defined by the available cooling power.

To avoid convective heat transfer from the cryostat wall at ambient temperature to the equipment at cryogenic temperature, the Knudsen number in the system

$$Kn = \frac{k_B T}{\sqrt{2}\pi\sigma^2 p l_{char}} \tag{4.1}$$

must be greater than 10. With the dimension described above, a pressure of 10^{-4} mbar or lower is sufficient to assume free molecular flow. Thus, the cryostat is evacuated to high vacuum conditions using a Leybold Turbolab 80i vacuum pump system. It consists of a backing pump connected in series with a turbo-molecular pump, which is automatically turned on when the pressure decreases below the threshold of 10^{-2} mbar. To speed up the evacuation process of the Turbolab backing pump, another backing pump is connected in parallel, using a manual valve on the cryostat cover. The vacuum is measured by a Leybold Penningvac PTR90N sensor, that combines a MEMS-Pirani sensor with a cold cathode ionization sensor. It has a measurement range from 10^3 mbar to 10^{-8} mbar. With this high vacuum set-up, only the heat loads induced by heat conduction through the rods and by thermal radiation have to be considered.

For the heat load on the first stage of the cryocooler, the radiation heat from the cryostat wall onto the high-temperature shield is determined by

$$\dot{Q}_{cryostat\text{-}shield} = \frac{\Gamma A_{shield}\left(T_{cryostat}^4 - T_{shield}^4\right)}{\frac{1}{\varepsilon_{shield}} + \frac{A_{shield}}{A_{cryostat}}\left(\frac{1}{\varepsilon_{cryostat}} - 1\right)}, \tag{4.2}$$

assuming concentric, long cylinders, with Γ being the Stefan-Boltzmann constant, ε the emissivity and A the area. The area of the shield $A_{shield} = 1.32\,\text{m}^2$ has an emissivity of $\varepsilon_{shield} = 0.04$ and the area of the cryostat $A_{cryostat} = 2.20\,\text{m}^2$ has an emissivity of $\varepsilon_{cryostat} = 0.24$ [124]. Assuming a shield temperature of 70 K, the radiation heat load is less than $\dot{Q}_{cryostat\text{-}shield} = 22\,\text{W}$. The remaining margin to the first stage cryocooler power is suficient to account for other effects (windows, G10, MLI spacers, copper, wiring, piping...).

The heat load by conduction through the G-10 fiberglass epoxy suspensions of the outer shield is determined by Fourier's law

$$d\dot{Q} = A_{rod}\lambda_{G\text{-}10}\frac{\partial T}{\partial L}. \tag{4.3}$$

Integration yields $\dot{Q} \approx 0.5\,\text{W}$, which is negligible compared to the radiation heat load.

The heat load on the second stage of the cryocooler has several contributions. Conductive heat loads through the suspensions and the piping add up to 2 W following Fourier's law. An analogous treatment of the radiation load leads to an estimation of 2 W. It can be assumed to decrease by 90 % when using multi-layer insulation on the low-temperature shield.

In summary, the heat loads into the first and second stages of the cryocooler are within the heat load budget with a safety factor of at least 2.

4.6. Pressure measurement

Three of the four capillaries are used for sampling. Figure 4.1 only shows two of them for clarity. The remaining capillary is used for pressure measurement. When connecting cold and warm fluids through capillaries or piping, thermal acoustic oscillations (TAO) might occur. TAO can 'pump' heat into the cryogenic system, hence affecting the thermal stability of the equilibrium cell. The resulting pressure oscillations affect the pressure measurement as well. In a numerical study, Rott has found two major parameters influencing TAOs, i.e. the temperature ratio $T_\mathrm{warm}/T_\mathrm{cold}$ along the capillary and the tube length ratio $\zeta = L_\mathrm{warm}/L_\mathrm{cold}$, with L_cold being the tube length from the lowest temperature to the inflection point of the temperature profile and $L_\mathrm{warm} = L_\mathrm{capillary} - L_\mathrm{cold}$ [125]. Rott [125] found a tube length ratio of $\zeta = 1$ to result in a maximum unstable region. His findings are experimentally verified [126]. In Figure 4.5, the region where TAOs might occur for helium and $\zeta = 2$ is compared against the operation range of CryoPHAEQTS. For some operation states in the temperature range from 20 K to 45 K, there is a risk of TAOs. The tube length ratio in CryoPHAEQTS is $\zeta = 2 \ldots 4$, depending on the capillary. Also, there is no thermal anchoring of the capillaries at an intermediate temperature, which could create a sharp temperature gradient. After commissioning, no measures had to be taken, as TAOs have not been observed.

The capillary is led through a vacuum feedthrough and connected to a Cerabar M PMP51 absolute pressure sensor (PI44) with a measurement range from 0 bar to 151 bar and a Deltabar S PMD75 differential pressure sensor (PDI40) with a measurement range from -50 mbar to 50 mbar. The sensor PI44 is used to get a rough estimate of the equilibrium cell pressure. It can not be used for accurate measurements due to its typical uncertainty of ± 200 mbar. The differential pressure sensor PDI40 is connected to a secondary fluid system. This system is equipped with three pressure sensors (PI41, PI42, PI43), which can be switched according to their respective measurement ranges. The sensors PI42 and PI43 are part of a PACE1003 measurement system supplied by Baker Hughes, which accurately measures the ambient pressure as well (PI40). A universal pressure module (PI41) extends the available pressure ranges to 200 bar. The pressure sensors are summarised in Table 4.1.

The pressure of the secondary system can be adjusted in the range from 0 bar to 151 bar using a needle valve for nitrogen gas dosing and another valve for venting or evacuation. The equilibrium cell pressure is determined by

$$p_\mathrm{equilibrium} = p_i + p_\mathrm{ambience} - p_\mathrm{PDI40}, \text{ with } i = \{\text{PI42, PI43}\} \text{ and} \tag{4.4}$$

$$p_\mathrm{equilibrium} = p_\mathrm{PI41} - p_\mathrm{PDI40}. \tag{4.5}$$

Table 4.1.: Pressure sensors used in CryoPHAEQTS and their respective measurement ranges and typical uncertainties ($k = 2$).

| Tag	Supplier	Model	Measurement range	Typical uncertainty
PDI40	Endress+Hauser	Deltabar S PMD75	-50 mbar to 50 mbar	< 0.1 mbar
PI40	GE Sensing	Pace1003 IRS0	750 mbar to 1150 mbar	0.1 mbar
PI41	GE Sensing	UPMP	0 bar(a) to 200 bar(a)	20 mbar
PI42	GE Sensing	Pace1003 IPS2	-1 bar(g) to 70 bar(g)	10 mbar
PI43	GE Sensing	Pace1003 IPS2	-1 bar(g) to 10 bar(g)	2 mbar
PI44	Endress+Hauser	Cerabar M PMP51	0 bar(a) to 150 bar(a)	200 mbar
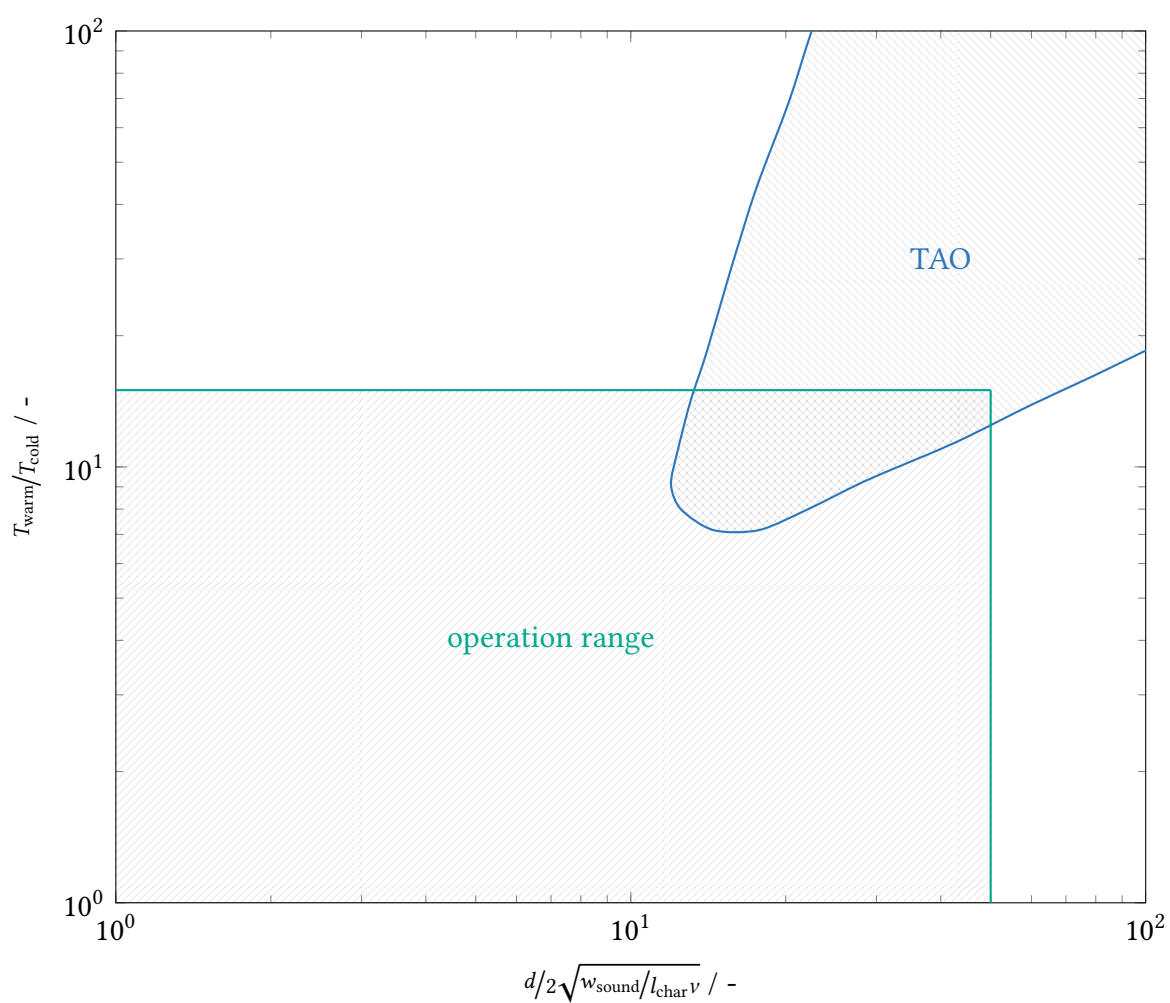
Figure 4.5.: Region of thermal acoustic oscillations (—) for helium and for a ratio of warm to cold capillary length of $\zeta = 2$ according to Rott [125] compared to the operation range of CryoPHAEQTS (—).

4.7. Temperature measurement and control

For all temperature measurements below 77 K, CERNOX® sensors supplied by Lakeshore Inc. are used. Pt100 sensors are used for the high-temperature shield and the vacuum pump temperature monitoring only. CERNOX® sensors are made of zirconium oxy-nitride, which is a thermistor element with negative temperature coefficient (NTC)

$$\frac{\partial R}{\partial T} < 0. \tag{4.6}$$

Contrary to Pt100-sensors, which have a positive temperature coefficient (PTC), their resistance increases by some orders of magnitude when cooling from ambient to cryogenic temperatures. This temperature coefficient can also be expressed as dimensionless temperature sensitivity

$$S_{T\text{-measurement}} = \frac{T}{\partial T}\frac{\partial O}{O(T)}, \tag{4.7}$$

with $O(T)$ being the measurand, i.e. electrical resistance for resistance temperature detectors.

The CERNOX® sensors have been chosen due to their high sensitivity in the temperature range below 100 K, while covering the whole temperature range of 10 K to 300 K. At a reference temperature of 20 K, they have a dimensionless sensitivity of -1.5 compared to 0.74 for Pt100 sensors, -0.29 for silicon diodes and 0.11 for capacitance sensors. They offer low uncertainty ($u_{\text{sensor}}(T) < \pm 20\,\text{mK}$) and good repeatability, particularly below 70 K. Also, different bands, where the highest sensitivity of the sensor is adjusted to the desired temperature range, and different packages are available, which ease installation in different environments. A literature review has shown, that this type of sensor has not been used for phase equilibria measurements yet, as most measurements took place before commercial availability. However, they require intensive calibration since there is no standard curve. The sensors including their bands, calibration, installation place and packages are listed in Table 4.2.

Also, the excitation current must be adjusted to the temperature to limit self-heating of the sensor. If the same constant excitation current of 1 mA were used on a typical CERNOX® sensor at cryogenic temperatures, the dissipated power at the sensing element would exceed 1 mW leading to destruction or loss of calibration. Therefore, the excitation current is adjusted to yield a temperature-independent voltage drop of about 2 mV, which is also used for calibration by Lakeshore Inc. This voltage drop range is considered a good trade-off considering self-heating on the one hand and measurement resolution and signal-to-noise ratio on the other hand.

While self-heating can be kept below 1 mK by variable excitation currents, other types of heat input must be avoided as well. In high-vacuum environments, the sensors must not be exposed to thermal radiation and should be covered to be representative of the surface temperature that they are mounted on. Another issue is the sensor wiring. At the electrical feedthrough of the cryostat, the wiring has ambient temperature and induces a conductive heat along the wires into the sensor. This heat load can be avoided by using wiring with

Table 4.2.: Temperature sensors used in CryoPHAEQTS. The package MT is a SD-sensor mounted on a screw with M3 thread; the package AA is a cylindrical copper pin to be placed in bore holes; the package SD is a hermetically sealed cuboid, which can be glued or pressed onto a surface.

Tag	Type and band	Package	Calibration	Installation place
TI72	CX-1070	MT	4–325 K	Pre-cooling block
TI73	CX-1070	MT	4–325 K	Cryocooler block
TI74	CX-1070	AA	4–325 K	Cell wall (top)
TI75	CX-1070	AA	4–325 K	Cell wall (bottom)
TI76	Pt100	wire-wound	class B standard curve	HT-shield
TI77	Pt100	wire-wound	class B standard curve	HT-shield
TI80	CX-1080	SD	20–325 K	Vapor phase
TI81	CX-1080	SD	20–325 K	Liquid phase

high thermal resistance (i.e. manganine or phosphor-bronze) and small diameters (e.g. AWG 36). Additionally, the wiring must be thermally anchored to an object at a similar temperature as the one to be measured. The residual conductive heat load as well as the Joule heating produced by the wiring resistance can dissipate into the object rather than the sensor. Since this object has a considerably higher thermal mass than the sensor, the thermal anchoring leaves the temperature measurement unaffected. In CryoPHAEQTS, all sensor wiring is made of phosphor bronze with either AWG 32 or AWG 36 dimensions. The wiring is thermally anchored at the high-temperature shield and at the respective installation place. For this purpose, film conductors are used. A picture of such a film conductor is shown in Figure 4.6, which depicts the thermal anchoring of the bottom temperature sensor of the equilibrium cell. The two sensors which are immersed in the fluid in the equilibrium cell dissipate their heat loads into the fluid along the outlet tube.

The exact temperature of the high-temperature shield does not affect the accuracy of the phase equilibrium measurement. The temperature should be as low as possible, but some K higher than the equilibrium cell temperature to avoid condensation or even freezing of the circulating fluid. Therefore, PT100 sensors without additional calibration are used for measurement of the high-temperature shield temperature. At 70 K, they have an uncertainty of ±2 K. The wire-wound sensors with a diameter of 2 mm are installed in small copper blocks mounted on the bottom side of the shield cover. The temperature of the low-temperature shield is not monitored, as the shield is regularly dismounted during maintenance on the equilibrium cell

All wiring consists of a twisted strand of pairwise-twisted wires. This design hinders electromagnetic radiation from affecting the measurement results. The wiring is led to ambience through electrical vacuum feedthroughs on the cryostat cover. The wiring of the two fluid temperature sensors is connected to two high-pressure electrical feedthroughs. Twisted pair cables connect the atmospheric side of the feedthroughs with the electrical cabinet, where they are either plugged into a model 224 temperature monitor supplied by Lakeshore Inc, or a model 26 temperature controller supplied by CryoCon Inc.
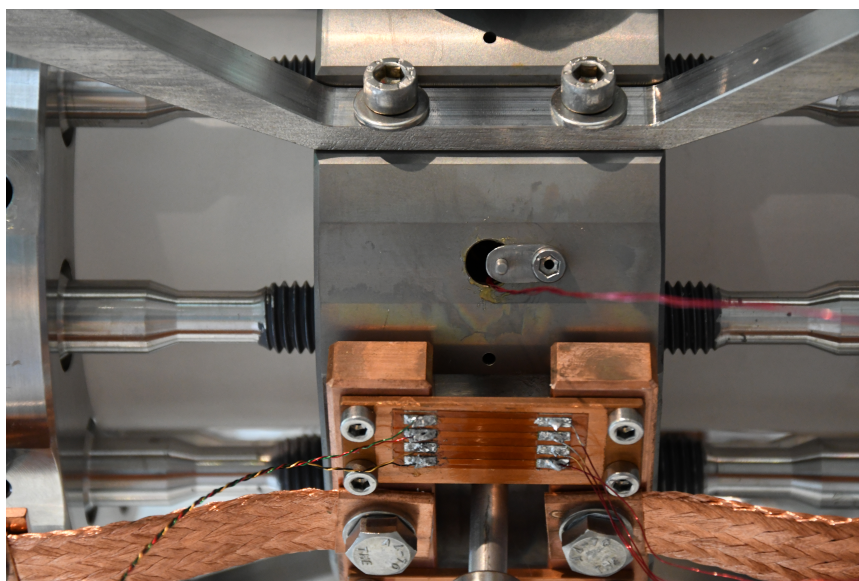
Figure 4.6.: Thermal anchoring of the temperature sensor at the bottom of the equilibrium cell.

The temperature monitor is used for temperature measurement of the high-temperature shield as well as the fluid in the equilibrium cell. The temperature controller offers 4 sockets for temperature sensor input, 2 powered outlets and 2 analogue outlets with a 0–10 V signal. The two analogue outputs are connected to two Z20-10 programmable power supplies supplied by TDK Lambda. These power supplies are used to power two heating foils supplied by Minco. These heating loops allow to fine-tune the wall temperature at the top and at the bottom of the equilibrium, individually. In principle, the wall temperatures can be set to different set points to align the two fluid temperatures in the cell.

A third 0–10 V outlet would have been ideal to control the output of a Z36-12 programmable power supply connected to the compensation heater below the second stage of the cryocooler. Since only two powered outlets are available, the 0–100 mW option is used in combination with a 1 kΩ resistor. The voltage drop along the resistor is used as analogue 0–10 V signal to control the power supply. While this solutions works, it makes the PID control of the loop more complex, because a linear power increase of the temperature controller induces a parabolic increase in the 0–10 V signal. In practice, this has never been an issue. Another two programmable power supplies are used to power a heating cartridge of 50 Ω in the pre-cooling block and two parallel Widap WD300 load resistances placed on top of the high-temperature shield. All heaters are protected by relays of the temperature controller and monitor, which break the connection in case of a high-temperature alarm, which is set at 310 K. The heaters, their connections and control modes are summarised in Table 4.3.

Initial PID parameters have been found by the method of Ziegler-Nichols at liquid nitrogen temperatures, as presented in [127]. They have been adjusted by using the auto-tune feature of the model 26 temperature controller. Further adjustments have been made by simple trial-and-error. Different optimal parameter sets have been obtained for liquid neon and liquid nitrogen temperatures due to the drastic changes of thermal conductivity

Table 4.3.: Overview of the heating and temperature control concept of CryoPHAEQTS. The power supply models indicate their maximum voltage and current. The given heater powers are the threshold values of over-voltage protection of the power supplies.

Tag	Control mode	Signal	Power supply	Heater	Power / W	Place
JI72	Manual	USB	Z60-3.5	50 Ω cartridge	50	Pre-cooling
JI73	PID	transformed 0–10 V	Z36-12	Brazed heating conductor	300	Cryocooler
JI74	PID	0–10 V	Z20-10	12 Ω heating foil	12	Top of cell
JI75	PID	0–10 V	Z20-10	12 Ω heating foil	12	Bottom of cell
JI76	Manual	USB	Z60-20	2 parallel 7 Ω load resistances	300	HT-shield

and heat capacity in this temperature range. Nevertheless, the following parameter set $\{k_\mathrm{P}, t_\mathrm{I}, t_\mathrm{D}\}$ has been found to be a good compromise in the temperature range from 20 K to 120 K:

- Cryocooler: {0.075, 150, 30},
- Cell wall: {50, 250, 50}.

Measurement campaigns at temperatures above 120 K require finding new suitable PID parameters for the three PID loops. Typical stabilities are ±1 mK for the equilibrium cell temperatures and ±10 mK for the cryocooler temperature. The determination of the temperature measurement uncertainty is described in the section A.3.

4.8. Software program

The test stand is controlled and monitored by a program in a LabVIEW 2019 environment. The computer communicates with the measurement and control equipment through USB- or LAN-connections. All temperatures, which are controlled, are connected to a model 26 temperature controller supplied by CryoCon Inc. All temperatures, which are measured only, are connected to a model 224 temperature monitor supplied by Lakeshore Inc. The mass flow sensor and all pressure sensors not belonging to the PACE1003 system are connected to a 34972 multiplexer data acquisition system supplied by Keysight Inc. This data acquisition system serves as highly accurate a/d converter from the 4 mA to 20 mA signal of the sensors to digital output processed by the software. While the programmable power supplies, which are used in PID loops, are directly connected to the temperature controller, the power supplies for the high-temperature shield heaters and the pre-cooling heater are controlled by the LabVIEW program. This way, in case of a computer or software crash, the temperature controller is able to work self-sufficiently and the conditions in the equilibrium cell remain unaffected. All received sensor values as well as all commands sent to the control equipment are logged in a TDMS file. All data relevant to phase equilibria data is logged in a separate file for post-measurement processing.

4.9. Sampling and composition analysis

The equilibrium cell offers access for sampling at three different heights in the cell volume to measure the compositions of the vapor as well as up to two liquid phases. The sampling capillaries are connected to manual valves, which are connected to a valve panel allowing to measure the pressure and to evacuate the capillary system. To account for the different flow velocities due to the pressure range of 0 bar to 150 bar, the flow can be reduced by a needle valve in the sampling line. The samples are drawn into sampling cylinders with a volume of 150 mL, which have been evacuated at 60 °C. The sample pressure in the cylinders ranges from 100 mbar to 500 mbar.

Another valve panel is installed close to the gas chromatograph. Its diagram is shown in Figure 4.7. It is used to evacuate and bake out the sampling bottles at a temperature of 60 °C. Further, it has a connection to the carrier gas of the GC allowing dilution of the samples. The sampling bottles can either be connected directly for evacuation or by using an interjacent check valve, allowing the carrier gas to enter the bottle but preventing the sample from leaving it. The check valve connection is used, when diluting the sample.

The panel is also used for mixture preparation for gravimetric GC calibration. For this calibration method, a baked-out sampling bottle is weighed on a comparator scale. It is filled with one of the two components of interest and weighed again. Then, the check valve system is applied to make sure that the first component does not escape from the bottle when filling it with the second component. Afterwards, the bottle is weighed a third time. The mixture is diluted with carrier gas and agitated for at least 10 min. Finally, the ratio of peak areas of the GC analysis is assigned to the mass fraction ratio. This procedure can be repeated at different mass fraction ratios in order to construct an accurate calibration curve. Usually, a linear relation can be assumed and the calibration points are regressed orthogonally, taking into account the uncertainties of the peak area ratios and the mass fraction ratios. For non-linear relations, a piecewise defined calibration curve is used.

The samples are analysed using an Agilent 7890B series gas chromatograph. It is equipped with two switching valves to control the flows through the chromatographic columns. Natural gas components, i.e. low boiling natural refrigerants, are separated in a GS Gaspro column. Noble gases, air constituents and methane are separated in a 5 Å molecular sieve column with a length of 30 m and an inner diameter of 0.53 mm supplied by RESTEK. Peaks are detected in two thermal conductivity detectors. The oven temperature can be adjusted from −30 °C to 300 °C using internal heating and cooling by liquid carbon dioxide evaporation. The schematics of the gas chromatograph system are shown in Figure 4.8. The GC test bench is shown in Figure 4.9.

In standby mode, the sample loop with a volume of 100 μL is filled with air and both columns and detectors are purged with carrier gas. With activated valve 8, the sample loop is purged with the sample. Then, switching valves 1 and 2 are activated and the sample is pushed into the oven by the carrier gas flow. It can be split up to 1:10 to increase detector sensitivity. The sample is separated in the GS Gaspro column at constant temperature. After the retention time of methane, valve 2 is deactivated to avoid hydrocarbon deposition in the molecular sieve column. This way, only gases that have passed the GS Gaspro column faster than methane enter the molecular sieve. These gases are detected in the front detector; heavier hydrocarbon gases are detected in the back detector.
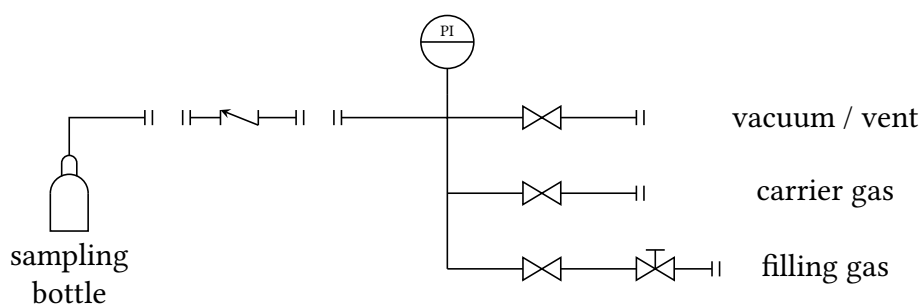
Figure 4.7.: Valve panel for sample preparation before GC analysis.
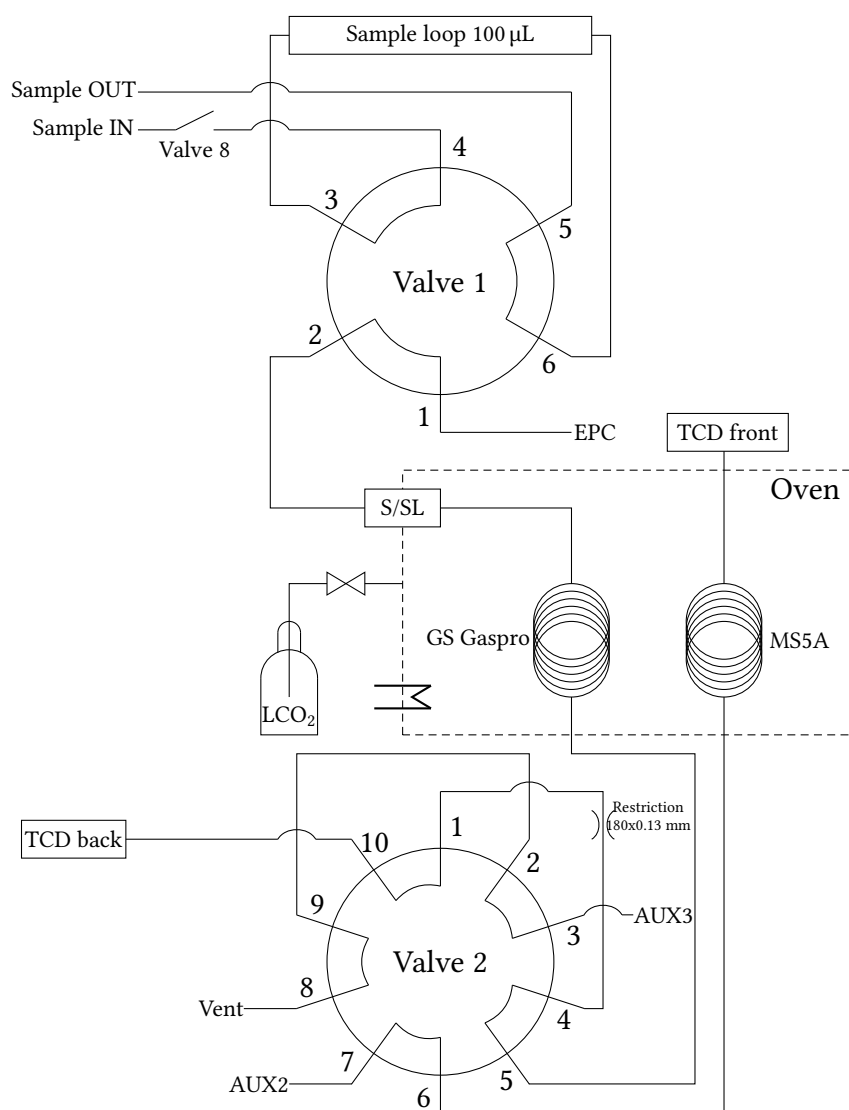

Figure 4.8.: Valve schematics of the gas chromatograph system.

Figure 4.9.: Gas chromatograph bench and valve panel for sample preparation.

As most GC parameters depend on the fluid system under investigation, they are given for each system individually in chapter 5.

4.10. Health, safety and environmental measures

The operation of a test stand in Germany requires compliance with several regulations and standards, which are listed in Table 4.4. The regulations ArbSchG, ArbStättV, BetrSichV, GefStoffV and BImSchG build the framework for safety measures concerning operation of plants. Specific safety issues are delegated to standards, such as TRBS or TRGS, and norms corresponding to the technical state of the art.

The main requirement defined by the regulations is a risk assessment which contains all plausible hazards as well as measures to avoid them. It is demanded by §3 BetrSichV concerning the safe use of equipment, by §6 GefStoffV concerning handling of hazardous substances, §3 ArbStättV concerning the layout and equipment of the workplace, §§5 and 6 ArbSchG concerning health and protection of the workers. In TRBS 1111, a classification of hazards is given. It groups them into

- mechanical hazards, such as moving machine parts,
- electrical hazards, such as electric shock,
- hazardous substances,
- biological hazardous substances,
- fire and explosion hazards,
- thermal hazards, such as hot or cold surfaces,
- special physical effects, such as noise, radiation or vibration,
- workplace conditions, such as ventilation,

- physical stress, such as heavy lifting,
- mental stress, and
- other hazards.

The main health, safety and environmental measures that had to be implemented are presented using this classification. By law (§4 BetrSichV), risks have to be avoided by suitable technical measures. If these are not implementable or unreasonably complex, organisational measures may be defined, i.e. operation instructions. Personal safety measures, such as safety goggles and gloves, may only be enjoined if the residual risk cannot be further reduced by technical or organisational measures.

Mechanical hazards

The test stand is designed without sharp or potentially hazardous surfaces. All piping and wiring is installed above head height, thereby avoiding bumping or tripping. If the pressure in the equilibrium cell rises above the allowable working pressure, a burst disc serves as pressure relief device. It is safely enclosed, preventing detached parts from harming people. In case of an unforeseen event, such as an equilibrium cell rupture, the aluminum shield as well as the cryostat hold back detached parts.

Electrical hazards

The equipment inside of the cryostat is subject to regular maintenance and modifications, involving touching of electrical equipment. Therefore, all electrical equipment is designed to operate with voltages below $60\,\text{V(DC)}$, which is the maximum allowed voltage to be considered non-hazardous. Other electrical equipment requiring higher voltages is not accessible, or access is restricted or prohibited by markings. The switch cabinet has been designed in cooperation with an electrical engineer and has been constructed by a contractor, thereby bearing a CE mark. It is only subject to minor modifications, when adding or replacing sensor wiring. It is inspected every 4 years, while the other electrical equipment in the laboratory is inspected once a year, as required by DGUV Vorschrift 3. The whole test bench and peripheral parts are grounded to avoid electrostatic charge.

Hazardous substances

Substances are considered hazardous if at least one of the following criteria is met. They cause harm when they are

- in contact with skin,
- inhaled,
- swallowed,
- flammable or lead to a potentially explosive atmosphere,
- oxidising,
- under pressure, or
- liquefied gases.

Table 4.4.: Relevant legislation and standards, which must be complied with for test stand operation in Germany.

Regulation or standard	Abbreviation	Last update	Main aspects
Arbeitsschutzgesetz	ArbSchG	2022	Occupational safety
Arbeitsstättenverordnung	ArbStättV	2020	Occupational safety
Betriebssicherheitsverordnung	BetrSichV	2021	Operational and process safety
Gefahrstoffverordnung	GefStoffV	2021	Handling of hazardous substances
Bundes-Immissionsschutzgesetz	BImSchG	2022	Emission control
Tätigkeiten mit Gasen - Gefährdungsbeurteilung	TRGS 407	2016	Risk assessment for handling of gases
Ortsbewegliche Druckgasbehälter	TRGS 510 & 745	2021	Handling of gases in cylinders
Ortsfeste Druckanlagen für Gase	TRGS 746	2016	Plants for pressurised gases
Gefährliche explosionsfähige Gemische	TRGS 720–727	2022	Dealing with potentially explosive atmospheres
Brandschutzmaßnahmen	TRGS 800	2011	Fire protection
Gefährdungsbeurteilung	TRBS 1111	2019	Risk assessment
Instandhaltung	TRBS 1112	2019	Maintenance
Sicherheitsrelevante Mess-, Steuer- und Regeleinrichtungen	TRBS 1115	2021	Protective measurement and control equipment
Prüfung überwachungsbedürftiger Anlagen	TRBS 1201 1–3	2022	Mandatory inspections
Mechanische Gefährdungen	TRBS 2111	2014	Mechanical hazards
Gefährdungen durch Dampf und Druck	TRBS 2141	2021	Hazards caused by steam and pressurised gas
Lärm- und Vibrations-Arbeitsschutzverordnung	TRLV	2017	Noise hazards
Sicherheits- und Gesundheitsschutzkennzeichnung	ASR A1.3	2022	Safety markings and labels
Verkehrswege	ASR A1.8	2022	Escape routes

Due to their toxicity, experiments involving carbon monoxide and fluorine are not allowed.

All gases in operation are under pressure and thereby considered hazardous. Due to the low refrigerant charge at the maximum design pressure, the test bench does not need to be considered a plant requiring inspections as defined by BetrSichV. However, it must be designed and constructed according to best engineering practice. Therefore, the wall thickness of all piping, capillaries, valves, sensors, feedthroughs and the equilibrium cell are designed according to DIN EN 13445 or procured with corresponding certificates. DIN EN 13445-2 proposes austenitic steels for cryogenic systems due to their tensile strength and ductility at these conditions. For hydrogen operation, austenitic steels with a molybdenum content above 0.5 % are stable to hydrogen embrittlement. For oxygen operation, BG Merkblatt M034 only allows austenitic steels with a combined chromium and nickel content above 22 %. The austenitic steel 1.4571 (316Ti) meets both requirements and has been used for all mechanical components exposed to cryogenic temperatures.

This way, it is assured that hazardous substance is released only during evacuation of the test stand, or in case of an uncontrolled rise of pressure. For controlled release, a vent line as well as the vacuum pump exhaust line is led outside of the laboratory. For uncontrolled release, a burst disc is connected to the equilibrium cell, whose exhaust pipe leads outside as well. It has been designed to burst at the allowable working pressure of 151 bar, using the worksheets DIN EN 13445. The maximum mass flow has been calculated according to DIN EN ISO 21013-3 leading to a design diameter of 6 mm [128]. The worksheets require a maximum pressure drop in the connecting piping of 3 % of the design pressure. With a calculated pressure drop of 4 bar, this requirement is met. The venting line is equipped with gratings to avoid insects from nesting.

In case of an unforeseen rupture of the equilibrium cell, the cryostat volume has been designed to hold the maximum inventory of the equilibrium cell. The maximum inventory corresponds to a completely filled cell at the triple point of neon. With a cryostat volume of 200 L, the cryostat pressure cannot exceed 1.5 bar(a). Redundantly, the cryostat is equipped with a burst disc at this pressure. Thus, the release of hazardous substance cannot harm people. There are only minor emissions of low GWP gases into the atmosphere.

Operation with oxygen requires special safety measures. All surfaces, which are in contact with the investigated fluid, must be free of grease, oil and lubricant residues to avoid ignition at high oxygen concentrations. In particular, another circulator pump without lubricant and another vacuum pump using PFPE oil must be installed. In case of a fire in the laboratory, the oxygen inventory in the test stand might act as fire accelerant. Probably, the fire would increase the equilibrium cell temperature and its pressure above burst disc opening pressure and release most of the oxygen. Although the safety concept would allow it, fluid mixtures containing a flammable component together with oxygen are prohibited.

For operation of the GC, liquid carbon dioxide is used from a riser tube bottle. Uncontrolled release has a refrigeration effect that might lead to cold burns. Therefore, a specific operation instruction ensures a tight connection from the cylinder to the GC system.

HCs and hydrogen are flammable and build potentially explosive atmospheres. This hazard is dealt with in the next paragraph.

Fire and explosion hazards

The assessment of fire and explosion hazards requires knowledge about physical properties of substances, which is listed in Table 4.5 for all flammable substances of interest. All of them form a potentially explosive atmosphere when they get in contact with air or pure oxygen. All areas where the release of these substances cannot be avoided must be taken into account for the risk assessment. These areas are the outlet of the vent line and the vacuum pump exhaust line, the interior of the vacuum pump and the outlet of the GC system. The internal parts of the test stand are leak-proof and do not pose a risk. Nevertheless, care has been taken to minimise refrigerant inventory.

The GC system continuously consumes hydrogen carrier gas and releases it into the laboratory. Therefore, a room ventilation and a flammable gas sensor have been installed. If the hydrogen concentration in the room exceeds 20 % of the lower explosion limit (LEL), the ventilation is automatically turned on and a visual warning signal is activated. Furthermore, the hydrogen supply from the gas cylinder cabinet is shut off automatically. However, the GC system emits less than $100\,\mathrm{mL\,s^{-1}}$ leading to an explosive volume below $10\,\mathrm{L}$ assuming natural ventilation in the room. Ignition of such a small amount would only lead to a deflagration instead of an explosion.

On a secondary level, ignition sources must be avoided. There are no ignition sources in the surroundings of the vent and exhaust line. The spread of potentially explosive atmosphere does not reach the lightning rod on top of the roof. For the GC system, no further risk reduction is implemented due to the low risk of a deflagration. The vacuum pump is used to evacuate the equilibrium cell, sampling bottles and capillaries, capillary connections and supporting piping. A simultaneous pumping of flammable media and air cannot be ruled out during regular operation. Therefore, the pump interior is classified as explosion zone 1. This zone classification restricts the choice of equipment to so-called category 1 or category 2 equipment according to GefStoffV, representing the level of fault security. A regular vacuum pump might act as ignition source due to hot surfaces, mechanical or electrical sparking or electrical current, e.g. accidental ground. Other important properties, which affect the choice of equipment, are the temperature class and the explosion group of the medium. The use of hydrogen requires IIC certified equipment and the use of n-butane and ethene requires a temperature class of T2 or higher. Therefore, an ATEX-certified vacuum pump of category 1, explosion group IIC and temperature class of T4 has been installed. The pump itself is designed with class (c), i.e. constructive safety, and the motor with class (e), i.e. increased safety. The supplier demands further requirements, which are:

- automatic shutdown in case of low oil level,
- feed cut off if the entry temperature exceeds a threshold,
- automatic shutdown if the exit temperature exceeds a threshold.

To meet these requirements, a valve, two temperature sensors and a pressure sensor have been installed according to Figure 4.10. The valve and the sensors have ATEX-certified classifications as listed in Table 4.6. The solenoid valve does not allow fluid temperatures above $55\,^\circ\mathrm{C}$. The temperature and pressure sensors are designed as class (ia), i.e. intrinsically safe. They are connected to transmitters, which act as galvanic isolators

Table 4.5.: Property data of selected refrigerants relevant to explosion protection including the lower explosion limit (LEL), the upper explosion limit (UEL) and the maximum experimental safe gap (MESG). Ignition energies are tabulated for mixtures with air. All data is taken from the GESTIS data base [129].

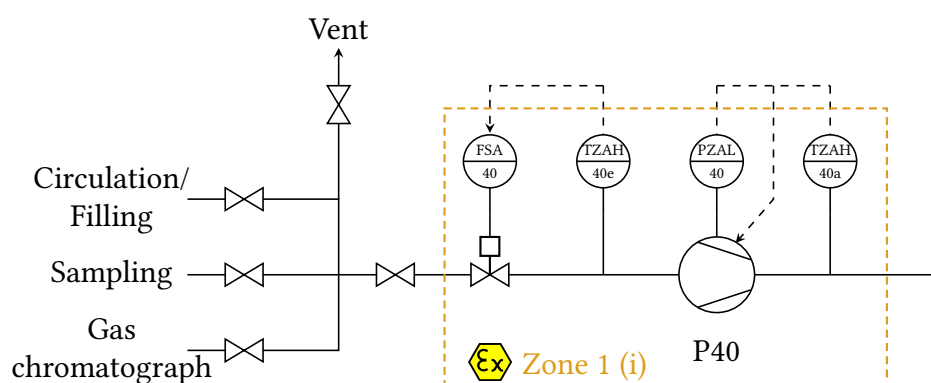| Name	Ignition point / °C	Ignition energy / mJ	Temperature class	Explosion group	LEL / vol-%	UEL / vol-%	MESG / mm
Hydrogen	560	0.02	T1	IIC	4.0	77.0	0.29
Methane	595	0.29	T1	IIA	4.4	17.0	1.14
Ethane	515	0.25	T1	IIA	2.4	14.8	0.91
Ethene	440	0.082	T2	IIB	2.4	32.6	0.65
Propane	470	0.24	T1	IIA	1.7	10.8	0.92
Propene	485		T1	IIA	1.8	11.2	0.91
n–butane	365	0.25	T2	IIA	1.4	9.4	0.98
iso–butane	460		T1		1.5	9.4	

Figure 4.10.: Piping and instrumentation diagram of the ATEX vacuum system.

Table 4.6.: Instruments accounting for protection against potentially explosive atmospheres.

Tag	Description	Supplier	Model	EX-marking
P40	Vacuum pump	Leybold	Trivac D16B ATEX	EX II 1G IIC T4
P40	Motor	EMOD Motoren	EeDA 80L/4A	EX II 2G T4 (e)
MV40	Solenoid valve	Buerkert	Type 6213	EX II 2G IIC T55°C
TI40a	Temperature sensor	WIKA	TR10-C	EX II 2G IIC T1 (ia)
TI40e	Temperature sensor	WIKA	TR10-C	EX II 2G IIC T1 (ia)
PI40	Pressure sensor	WIKA	IS-3	EX II 2G IIC T4 (ia)
	Temperature converter	Pepperl+Fuchs	KFD2-GUT-Ex1.D	EX II 1G IIC (ia)
	Trip value transmitter	Pepperl+Fuchs	KFD2-CRG2-Ex1.D	EX II 1 G IIC (ia)

limiting the energy supply into the sensor circuit. The energy of the electrical circuit of these sensors, which contains inductive and capacitive contributions, must be kept below $2/3$ of the ignition energy of the respective fluid explosion group (here IIC). The requirements for this wiring are defined in VDE 60079-25. In particular, intrinsically safe cables are designed in light blue color and layed in a distance of at least 50 mm to other cables. For each cable, maximum cable lengths to limit the stored energy have been calculated.

With this set-up, the risk is reduced to a level, where no tertiary measures to limit the impact of an explosion must be implemented. The findings of this risk assessment are explained in detail in a mandatory explosion protection document. In this document, the necessary inspection intervals according to BetrSichV are defined. Regular inspections are needed for the gas cylinder cabinets, the gas warning system, the ventilation, the vacuum pump and the corresponding electrical equipment.

Thermal hazards

All potentially hot surfaces are either not accessible or equipped with an appropriate warning sign. This concerns the vacuum pumps and the GC system. The GC system has supplier-installed warnings when opening the oven door.

Cold surfaces inside of the cryostat are not accessible and the exit line to the gas circulator as well as the capillaries are the only accessible potentially cold surfaces. Initially, a protective heater has been foreseen, but the performance of the two tube-in-tube heat exchangers proved to be sufficient to warm up the leaving fluid to room temperature.

Special physical effects

No special physical effects besides noise are expected to be considerable. A sound level measurement during simultaneous operation of the ventilation, the cryocooler and the vacuum pumps showed a sound exposure level below 80 dB, which is the threshold for additional safety measures according to TRLV.

For a future upgrade of the test stand with a DLS system, hazards stemming from optical radiation must be analysed.

Workplace conditions

The laboratory can be heated, lighted, shadowed and ventilated. There are two escape routes with a width allowing safe escape for at least 5 persons. For many tasks, it is possible to remotely control the test stand.

Physical and mental stress

No measures have been implemented.

Other hazards

No measures have been implemented.

4.11. Test stand operation

Prior to any measurement campaign, a thorough leak test is conducted. For this purpose, the test stand is filled with helium to about 100 bar and every fitting as well as the equilibrium cell is investigated using a threshold of 1×10^{-6} mbar L s^{-1}. During evacuation of the circuit, the shields and the cryostat container are mounted. First, the cryostat is evacuated to a pressure of about 10^{-3} mbar using an auxiliary vacuum pump. Once this pressure is reached, the high vacuum pump system is turned on and the auxiliary vacuum pump is disconnected by a hand valve.

During evacuation of the cryostat, the circuit is purged with the highest boiling gas and evacuated again. When the pressure has decreased to 10^{-5} mbar, the LABVIEW program is started and the cryocooler temperature is set to the triple point of the highest boiling gas. Then, the cryocooler is turned on. The set-point of the cryocooler is usually reached over night. The voltage of the pre-cooling heater is adjusted until its temperature has exceeded the equilibrium cell temperature. For measurement campaigns, whose temperature is above 70 K, the voltage of the aluminum shield heaters can be adjusted for the shield temperature

to roughly equal the equilibrium cell temperature. The pure gas (in case of a subsequent mixture measurement the highest boiling component) is slowly dosed into the circuit, while trying to avoid sudden temperature increases of several degrees. The gas supply is shut when the liquid filling level of the equilibrium cell is about 70 mL corresponding to about 2/3 of the height of the cell window. The cryocooler temperature is decreased until a solid phase has formed in the equilibrium cell. Then, the circuit is evacuated for about 30 min in order to eliminate traces of any low boilers. Then, the cryocooler set-point is increased to 3 K below the desired measurement temperature. When the equilibrium cell temperature has increased to about 200 mK below the desired measurement temperature, the fine-tuning heaters on top and on the bottom of the cell are turned on. The set-points of these temperatures can be set individually for the two fluid temperature sensor readings to overlap within their uncertainties.

When the two fluid temperatures and the pressure have settled to ±2 mK and ±0.1 %, respectively, at least 200 data points are recorded in LABVIEW. These data points are written in a separate file from the continuous log file. By default, a data point is taken every 3 s. The temperatures and pressures of the relevant sensors are continuously plotted in the user interface to assess stability, particularly during measurement data recording. After the 200 points have been taken, the record file can be used for post-processing and uncertainty analysis.

Measurement campaigns can either consists of several isochores, which is the case for vapor pressure measurements of different pure fluids, or isotherms, which is the case for VLE measurements of a fluid system. In the isochoric case, the cryocooler temperature is raised by the desired temperature difference to the next measurement point (usually 0.5 K to 1 K). The equilibrium cell set-points must not be adjusted until the equilibrium cell temperature has increased to about 200 mK below the desired measurement temperature. A premature adjustment might make the power supplies go into over-voltage protection mode, which is set at 12 V to protect the heating elements. This over-voltage protection disturbs the PID control and the power supplies must be reset manually. In the isothermal case, the low boiling component is dosed into the equilibrium cell after the vapor pressure of the higher boiling fluid has been measured. Care must be taken to thoroughly evacuate all piping connected to the dosing line. The added fluid leads to a peak in temperature, which is then compensated by the PID control. The temperature decrease after the peak can cause a similar issue, if the PID control of the equilibrium cell heaters over-compensates. Therefore, the fine-tuning heaters should be turned off and not re-activated until the equilibrium cell temperature has increased to about 200 mK below the desired measurement temperature. Depending on the fluid system, the gas circulator is turned on for some time at a frequency enabling a thorough mixing of the phases. The level of agitation can be assessed visually through the windows. When the pressure has settled, the gas circulator is turned off and phase equilibrium is awaited. Again, at least 200 data points are taken.

For sampling, an evacuated sampling bottle is connected to the sampling valve panel. Before opening the valve of the bottle, the sampling capillary is purged for some time to get rid of any residue. In particular, the liquid phase capillary requires purging to avoid sampling of the vapor phase that has built up in the capillary. The purging duration depends on absolute pressure, but should not exceed 5 s in order to keep the phase equilibrium undisturbed. After purging, the valve of the sampling bottle is opened. Depending on the

fluid system, its pressure and its expected composition, 200 mbar to 600 mbar are sampled. The sampling bottle is disconnected from the sampling valve panel and re-connected to the valve panel at the GC. The couplings allow air to enter the connecting tube of the bottle. Therefore, this tube is evacuated before the bottle is filled with carrier gas to about 8 bar. After agitation for at least 10 min, the bottle is connected to the GC and the corresponding GC method can be loaded and started. The exact procedure depends on the fluid system and might involve cooling of the GC oven. In this case, the riser tube bottle of liquid carbon dioxide must be connected to the designated capillary extending from the GC. After the GC analysis, the sampling bottle can be disconnected and vented using a venting line leading to the room ventilation system. It can be evacuated and baked out using heating sleeves at the GC valve panel.

During this process, the disturbed phase equilibrium has time to settle. Again, 200 data points are taken, before the second phase is sampled. These points are used to assess, whether the prior sampling led to a disturbance beyond experimental uncertainty. This process is repeated for up to three occurring phases. Along the isotherm, it must be assured, that the sampling capillaries extend into their corresponding phases. Particularly for VLLE measurements, the phase separation line adjustments through evacuation and gas addition can be tedious. The amount of the added fluid can only be adjusted roughly through revolutions of the dosing needle valve, back pressure and time. For the future, an optional pressure vessel is to be installed for repeatable fluid dosing.

After the measurement campaign, the equilibrium cell is evacuated through the needle valve and/or the sampling valves. The equilibrium cell heaters are turned off during the evacuation process, but the cell temperature is kept above the triple point. When the cell pressure has decreased below 0.1 bar, the PID control and all heaters as well as the cryocooler are turned off. The turbo-molecular pump is kept running until the system has warmed up above the ambient air dew point. The line to the high vacuum pump system can be disconnected with a pneumatic angle valve, which is controlled from the high vacuum pump stand. The warm-up process usually takes 4 d. It can be accelerated by use of the heaters below their respective over-voltage protection thresholds. To avoid thermal stress in the system, the warm-up rate should not exceed $1\,\mathrm{K\,min^{-1}}$. The warm cryostat can be vented through a hand valve.

5. Experimental results

Before hitherto unpublished data is measured, the test stand has been commissioned using a nitrogen-argon mixture at 100 K. The nitrogen-argon system is chosen as reference fluid mixture due to its ideal behaviour close to Raoult-Dalton's law. Furthermore, the mixture is well-studied, because the phase separation emerges at comparatively high cryogenic temperatures enabling simple LN_2 bath cryostat technologies. Also, the two gases are cost-efficient and available in a purity of 99.999 % or higher. The VLE is measured at 100 K, because this isotherm offers the most available literature data to compare against. The total available literature data is listed in Table 5.1. The isotherm has been measured by Mair within his Bachelor's thesis [123] an the commissioning results are published in [130].

Several optimisation steps have been deduced from these commissioning results. Then, the vapor pressure of neon has been measured, since there are some discrepancies in the literature data. The vapor pressure of neon is also a pre-requisite for post-measurement processing of binary data involving neon, e.g. calculation of Henry coefficients. The results of these measurements have been published in [131]. Finally, the measurement results of the vapor-liquid equilibrium of the neon-helium system are presented and discussed.

5.1. VLE of the nitrogen-argon system

Prior to any fluid property measurement, the accuracy of the temperature measurement and the stability of the temperature control has been checked. As can be seen in Figure 5.1a, the equilibrium cell wall temperatures are set to 99.940 K to reach a mean fluid temperature of 100 K. Thus, the assumption of a uniform temperature in the cell, i.e. using the wall temperatures as representative phase equilibrium temperature, is not justified. The upper cell wall temperature has a higher ripple of about ±5 mK compared to the lower cell wall temperature despite using the same control parameters $\{k_P, t_I, t_D\}$. This ripple propagates into the vapor phase as well. Nevertheless, these low-amplitude fluctuations are acceptable for validation purposes of the test stand, as temperature stabilities of ±10 mK are reported for comparable test stands (see chapter 3).

After the first measurement campaign, the upper cell wall temperature sensor was re-wired, because the wires were incorrectly allocated causing a voltage ripple responsible for the fluctuations. The commissioning of the correct set-up yielded very low-amplitude fluctuations for both cell and fluid temperatures as shown with nitrogen in Figure 5.1b. It also shows that the temperature gradient between the cell wall and the fluid is a function of the absolute temperature (in this case, very close to the vapor phase temperature). This temperature gradient proved to be dependent of the liquid filling level and the charged fluid. It should be noted, that the cell wall temperatures might be shown higher than the

fluid temperatures as well. There is no physical explanation as the cell walls must always be colder than the fluid due to the heat flow orientation. Thus, the sensors must have been insufficiently thermally anchored in the bore holes, probably forming an enclosed vacuum space. The sensors are affected from self-heating and are not representative for the cell wall temperature. However, a possibly erroneous measurement of the wall temperatures does not affect the phase equilibrium measurements, as the fluid temperatures are measured separately. In any case, experimental experience is required to correlate the cell wall temperatures to the desired fluid temperatures.

Eleven data points have been measured along the isotherm at 100 K in the whole composition range. The data is listed in Table 5.2 including the absolute uncertainties of the respective measurands. Temperature and pressure uncertainties are calculated according to [132]. Both gases are supplied in 99.999 % purity by Air Liquide. They are not further purified by pumping on the frozen solid, as the main impurity is water. The composition is analysed in the GC system, which is calibrated using the following procedure defined by Kochenburger [133]. Mixtures of different composition are prepared gravimetrically covering the expected composition range. The mole fractions are determined by weighing of a sampling bottle on a mass comparator scale (PR2003 supplied by Mettler-Toledo). First, the evacuated sampling bottle is weighed. It is weighed again after each component addition into the mixture. Based on the charged masses and the molar masses of the components, the mole fractions are calculated. Then, the sampling bottle is brought to a pressure of 7 bar to 8 bar using the carrier gas hydrogen. After thorough agitation, the prepared sample is led into the GC system for analysis, yielding a certain peak area ratio. In principle, one calibration mixture can be sufficient for the GC calibration using a linear calibration function

$$\frac{y_2}{y_1} = \phi\frac{A_2}{A_1}, \tag{5.1}$$

with ϕ being the slope, y_i the mole fraction of component i and A_i the peak area of component i. By using multiple calibration mixtures, the uncertainty of the slope of the calibration curve can be decreased. For the nitrogen-argon system, 18 calibration mixtures have been prepared. The slope of the calibration curve is determined to $\phi = 1.02860 \pm 0.00962$, using orthogonal distance regression in the software package OriginPro 2018b and taking into account repeated measurements in the GC as well as repeated weighing of the sampling bottles. The calibration curve represents the type B uncertainty of the composition measurement and the repeated GC analysis of a sample from the equilibrium cell represents its type A uncertainty according to GUM [132].

The measurement results are compared against the current reference EoS of Gernert et al. [150] as well as available literature data in Figure 5.2. All literature data has been measured at a temperature of 100.0 K except for the data set of Hiza et al. [147], which has been measured at 99.9 K. The most reliable data set is assumed to be the one of Elshayal and Lu [144], because they use a synthetic method without requiring sampling or in-situ composition analysis. They charge an equilibrium cell with a fluid mixture of precisely known composition at a density corresponding to a resulting vapor fraction of $f \approx 0$. By assuming all the charged fluid occupies the liquid phase, the boiling point is determined
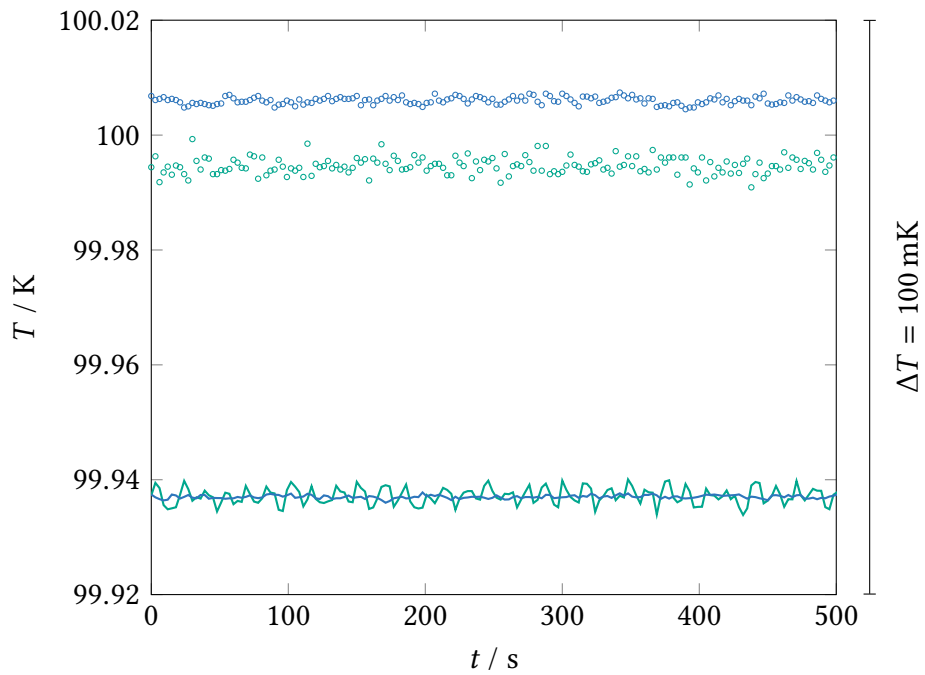
(a) Initial temperature sensor set-up used for the measurement of the Ar-N$_2$ system.
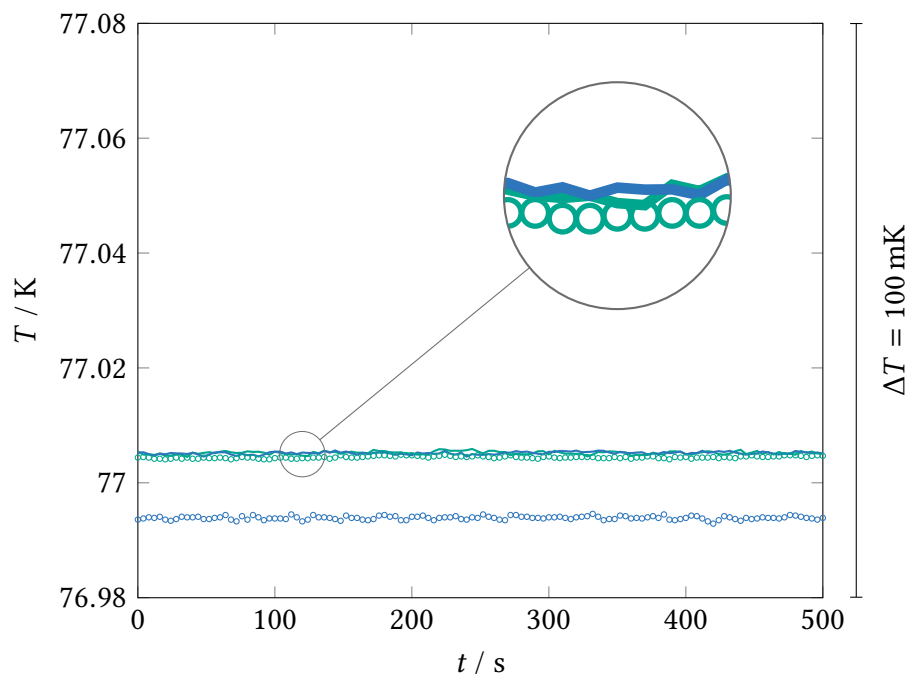
(b) Temperature sensor set-up after electrical optimisation using pure N$_2$.

Figure 5.1.: Typical temperature stability curves during a measurement routine of the top cell wall (—), the bottom cell wall (—), the liquid phase (○) and the vapor phase (○) before and after the electrical optimisation displayed on comparable axes.

Table 5.1.: Experimental VLE data sources for the argon-nitrogen system including their temperature range T, pressure range p and data set type. Literature, which is not compared against, is grayed-out.

Year	Authors	T / K	p / bar	Type
1916	Holst et al. [134]	74-90	0-2	isothermal
1956	Fastovskii et al. [135]	78-103	1-4	p,T,x,y
1962	Pool et al. [136]	84	1-2	isothermal
1965	Wilson et al. [137]	72-134	1-26	isobaric
1966	Narinskii [138]	90-120	1-24	isothermal
1966	Sprow et al. [139]	84	1-2	isothermal
1968	Thorpe [140]	80-115	1-11	p,T,x,y
1973	Massengill et al. [141]	90-113	3-13	p,T,x,y
1973	Miller et al. [142]	112	8-15	isothermal
1975	Lewis et al. [143]	85	1-2	isothermal
1975	Elshayal and Lu [144]	100	3-7	isothermal
1977	Mastera [145]	85-100	1-8	isothermal
1990	Xiao and Liu [146]	100	3-8	isothermal
1990	Hiza et al. [147]	80-100	0-8	isothermal
1993	Jin et al. [148]	123	12-29	isothermal
1999	Baba-Ahmed et al. [149]	95-121	2-27	isothermal

Table 5.2.: Experimental VLE data for the system nitrogen (1) + argon (2) at temperature T, pressure p, liquid mole fraction x and vapor mole fraction y with respective combined uncertainties u (with coverage factor $k = 2$). Uncertainties marked with an asterisk are based on the liquid phase temperature sensor only because the vapor phase temperature sensor failed.

| T / K	p / bar	x_1/ -	y_1/ -	$u(T)$ / mK	$u(p)$ / mbar	$u(x_1)$ / −	$u(y_1)$ / −
100.000	3.225	0	0	15*	2	0	0
100.001	3.782	0.101	0.217	15	2	0.002	0.003
100.002	4.230	0.189	0.356	15	2	0.003	0.004
99.999	4.781	0.303	0.496	15	2	0.004	0.005
100.001	5.258	0.403	0.599	15	2	0.005	0.005
100.001	5.717	0.511	0.689	15	2	0.005	0.004
100.002	6.225	0.630	0.776	15	2	0.004	0.003
100.002	6.699	0.740	0.847	15*	2	0.004	0.003
100.000	7.253	0.873	0.930	15*	2	0.002	0.001
100.001	7.509	0.934	0.964	15*	2	0.002	0.001
100.001	7.778	1	1	15*	2	0	0
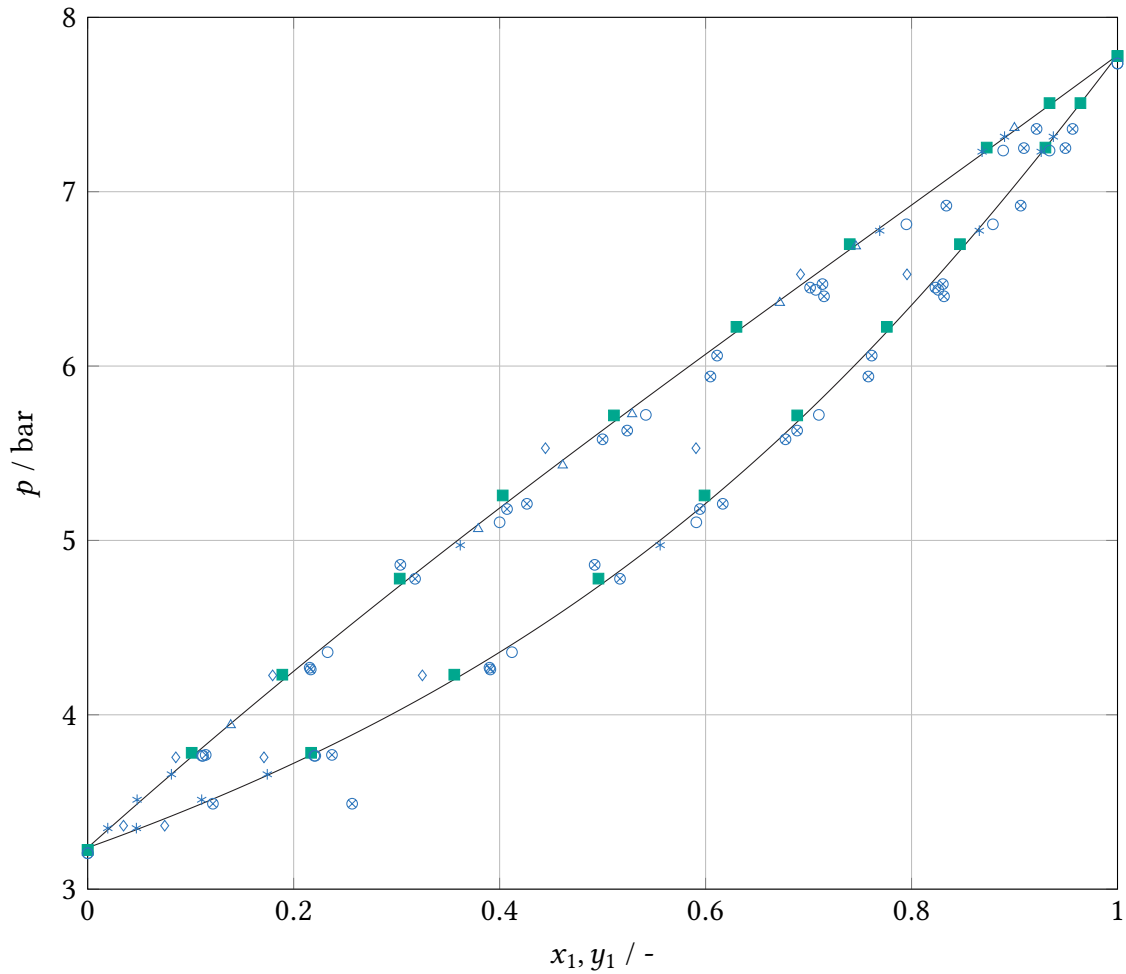
Figure 5.2.: Experimental VLE data of the nitrogen-argon system at 100 K of the data sets from this work (■), Narinskii [138] (∗), Elshayal and Lu [144] (△), Mastera [145] (◇), Xiao and Liu [146] (⊗), Hiza et al. [147] (○), and the reference EoS of Gernert et al. [150] (—).

by temperature and pressure measurement in equilibrium. However, the method does not allow thermodynamic consistency checking, as the vapor phase composition remains unknown. All other data sets use an analytical isothermal approach with sampling from both phases, enabling thermodynamic consistency tests.

To assess all data, the Redlich-Kister test, the Fredenslund test and the Van Ness test are applied according to chapter 2. For the calculation of the experimental activity coefficients, the fugacity coefficients have been calculated with the original PR EoS using the Soave α-function. The parameter m_i of the α-function and the pure component vapor pressure have been fitted to the experimental data sets with $k_{ij} = 0$. For the Redlich-Kister area test, a third-order polynomial is fitted to $\ln\left[\gamma_{\mathrm{exp},1}/\gamma_{\mathrm{exp},2}\right](x_{\mathrm{exp},1})$ and integrated over the whole composition range. The Fredenslund test is performed with Legendre-polynomials of third order as well. For the Van Ness test, the Van Laar g^{E} model is used. The test results are listed in Table 5.3, which also contains the averaged relative deviations of the bubble and

Table 5.3.: *ARD*s of the literature data at about 100 K and our data with respect to the reference EoS [150], as well as results of the Redlich-Kister test (RK) [21], the Fredenslund test (Fr) [25] and the Van Ness test (VN) [24].

Data set	ARD_{bubble} / %	ARD_{dew} / %	RK	Fr	VN
Narinskii [138]	0.29	0.27	fail	pass	non-random
Elshayal and Lu [144]	0.38	-	-	-	-
Hiza et al. [147]	0.62	0.37	fail	fail	non-random
Xiao and Liu [146]	1.94	1.83	fail	pass	non-random
Mastera [145]	2.78	3.13	fail	fail	non-random
This work	0.57	0.46	fail	pass	non-random

dew point pressures to the reference EoS. For the calculation of the *ARD*, the respective measurement temperatures have been used as fixed quantity.

None of the data sets performs well in the consistency tests. All of them fail the area test. However, the area test criterion evaluates the *relative* deviation of the areas above and below the zero base line. As the absolute areas are small due to the small activity coefficients, very small errors, i.e. $\Delta\gamma \leq 0.01$ lead to high relative errors. Hence, the defined test criterion is not met. The Van Ness test is also failed by all data sets, because the defined residuals do not spread randomly around the zero base line. The individual point-by-point residuals for all data sets but the one of Master [145] lie below ±0.08, which are acceptable according to the consistency index classification in Table 2.1. Figure 5.3 shows the experimental activity coefficients of this work as well as the resulting Van Ness residuals. The activity coefficients show symmetrical curves with correct limiting behaviour $\lim_{x_j\to 0} \gamma_i = 1$ and similar γ_i^∞ as is expected for such an ideal mixture. The Van Ness residuals yield a consistency index of 1, but they do not spread randomly around the zero base line. The Fredenslund test checks for an average absolute deviation between calculated and experimental vapor phase compositions, which must be below $\Delta y \leq 0.01$. This test is passed by the data sets of Narinskii [138] with $\Delta y = 0.0047$, Xiao and Liu [146] with $\Delta y = 0.01$ and this work with $\Delta y = 0.0032$. To conclude, the data set of this work performs as good as the other literature data sets in established consistency tests. It can be represented by a third-order g^{E}-model with an *AAD* comparable to the uncertainty of composition measurement. However, due to small activity coefficients, the applicability of the tests to this ideal system is questionable.

Gernert et al. have used the data sets of Narinskii, Elshayal and Lu and Hiza et al. for the development of their reference EoS, which explains their low *ARD*. The data sets of Xiao and Liu, Mastera have not been used in the parameter fitting process. Despite not having been included in the parameter fitting process of the reference EoS either, the data set of this work shows comparable average relative deviations to the considered data sets.

To further evaluate these deviations, they are plotted point-by-point in Figure 5.4 for the dew and bubble point pressures. They form a bell-shaped curve peaking at equimolar composition. Assuming the reference EoS to be accurate, the deviations might originate from temperature, pressure or composition measurement. Since the measurement uncer-
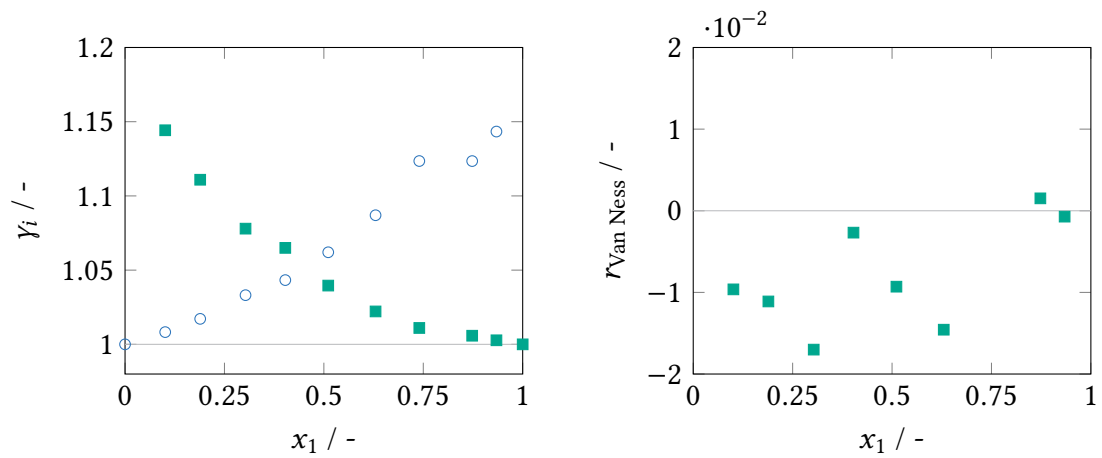
(a) Experimental activity coefficients of the components argon (○) and nitrogen (■).

(b) Distribution of the residuals of the van Ness consistency test.

Figure 5.3.: Experimental activity coefficients of this work used for the consistency tests and residual distribution plot of the Van Ness consistency test.
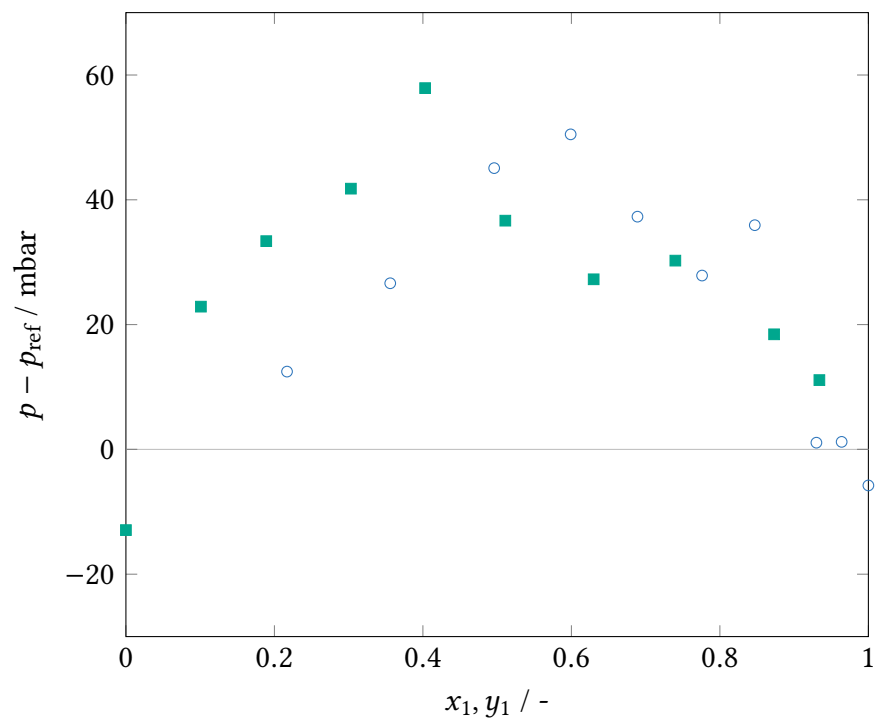

Figure 5.4.: Absolute deviations of the bubble point pressure (■) and the dew point pressure (○) from the reference EoS.

tainty of temperature and pressure is constant, while the composition uncertainty forms a similar bell-shaped curve, the highest optimisation potential can be found in the procedure of composition analysis.

Therefore, the GC calibration is checked with a certified gas mixture of $y_{1,\text{cert}} = 0.510$ supplied by Air Liquide with an uncertainty of 2 % (with $k = 2$). The recovery $F_{\text{recovery}} = x_{1,\text{cal}}/x_{1,\text{cert}}$ yields 97.4 %, which does not meet the target accuracy. Furthermore, repeated measurements show a small dependence from room temperature and pressure. Hence, the composition uncertainties given in Table 5.2 might contain small systematic errors. Ambient conditions during GC analysis aside, the accuracy of the balance, possible dead volumes during filling and evacuation of the sampling bottles and leakage might be affecting the accuracy of the calibration procedure. As a consequence from these findings, future GC calibration is done with several certified calibration mixtures only. The recovery of the calibration is checked once a day.

To conclude, CryoPHAEQTS is successfully validated against the nitrogen-argon system at 100 K. The target measurement uncertainties of temperature and pressure are met. An improved method for the composition analysis is derived from the measurement results. The data can be modeled using the PR EoS and a thermodynamically consistent g^{E}-model. The results show an excellent agreement with the most recent reference EoS and perform similarly to the most reliable data sets found in literature.

5.2. Vapor pressure of neon

The proposed concepts for mixed refrigerant cycles operated at temperatures below 50 K rely on neon as one of the main components [8, 9, 10, 11, 12]. The current reference EoS of Thol et al. has been developed using the complete data base shown in Table 5.4 [151]. Thol et al. replaced the former multiparameter reference EoS of Katti et al. [152] from 1986, altering some key parameters. Unfortunately, their EoS is yet to be published, but the parameters can be accessed through the REFPROP 10.0 software [33]. While the modifications of the triple point are minor, Thol et al. reduce the critical temperature from $T_{\text{crit, Katti}} = 44.49$ K to $T_{\text{crit, Thol}} = 44.4$ K as listed in Table 5.5. The near-critical domain is modeled by state-of-the-art Gaussian terms. The critical pressure and density are reduced by 0.2 bar and 0.2 mol L^{-1} respectively. There is only one reliable experimental data source for the critical point of neon of Grilly, who published values of (44.40 ± 0.07) K and (26.54 ± 0.24) bar [114]. As the quality of the current data base for the vapor pressure of neon is low compared to other fluids, speed of sound measurements have been included in the fitting process of the parameters of the critical and the vapor pressure curve [153].

The experimental data sources, which are grayed-out in Table 5.4, are based on non-standardised temperature scales, for which no rigorous conversion to the current temperature scale ITS-90 exists. The two publications dating from 1969 and 1974 are assumed to be measured on the IPTS-68. Data measured on the IPTS-68 or NBS-55 can be converted to the ITS-90, hence the different temperature scale does not add unknown uncertainty to the temperature measurement. Most data points have been contributed by Gibbons [154] and Grilly [114] with stipulated uncertainties of ±10 mK and ±2.5 mK respectively. Gibbons uses Germanium temperature sensors which are highly sensitive at cryogenic

Table 5.4.: Literature data sources of the vapor pressure curve of neon. Sources dating from before 1962 are grayed-out since they are based on individual temperature scales, which are not internationally recognised.

Year	Authors	Range / K	Scale	Reference
1978	Ancsin	20–27	IPTS-68	[156]
1974	van't Zelfde and Dokoupil	24–27	not reported	[103]
1972	Furukawa	24–27	NBS-55	[36]
1969	Gibbons	32–44	not reported	[154]
1966	Heck and Barrick	26–42	NBS-55	[13]
1965	Streett and Jones	24–34	NBS-55	[100]
1962	Grilly	24–44	NBS-55	[114]
1960	Bigeleisen and Roth	24–30	no standard	[157]
1936	Henning and Otto	24–27	no standard	[158]
1928	Verschaffelt	24–44	no standard	[159]
1927	Crommelin and Gibson	24–44	no standard	[160]
1919	Crommelin et al.	24–27	no standard	[161]
1917	Cath and Kamerlingh Onnes	24–44	no standard	[162]

Table 5.5.: Triple point and critical point data used for the reference EoS by Katti et al. [152] and Thol et al. [151].

Parameter	Katti et al. (1986)	Thol et al. (2018)
T_{trip} / K	24.56	24.556
p_{trip} / bar	0.4338	0.43355
T_{crit} / K	44.49	44.4
p_{crit} / bar	26.8	26.6163
ρ_{crit} / $^{\text{mol}}/_{\text{L}}$	23.88	24.1

temperatures. Germanium temperature sensors have a negative temperature coefficient which limits the applicability at high temperatures, i.e. $T > 100$ K. Hence, the stipulated uncertainty in the temperature range of the vapor pressure curve of neon is reasonable. Grilly uses a Platinum resistance temperature sensors, whose sensitivity at cryogenic temperatures is poor. His uncertainty statement should probably be one order of magnitude higher. Gibbons uses neon with impurities lower than 33 ppm, while Grilly uses relatively impure neon with a stated purity of 99.9 %. Heck and Barrick [13] and Streett and Jones [155] contribute few data points within their publications for binary mixtures with temperature uncertainties of ±50 mK and ±20 mK respectively. Based on this literature review, it would be beneficial to have high quality vapor pressure measurements of neon, based on the ITS-90 temperature scale.

The vapor pressure of neon is measured at 40 temperatures evenly distributed between 25 K and 44 K. The results are published in [131]. The natural mixture of neon isotopes, which has been supplied by Air Liquide, has a purity of 99.999 mol − %. About 50 % of
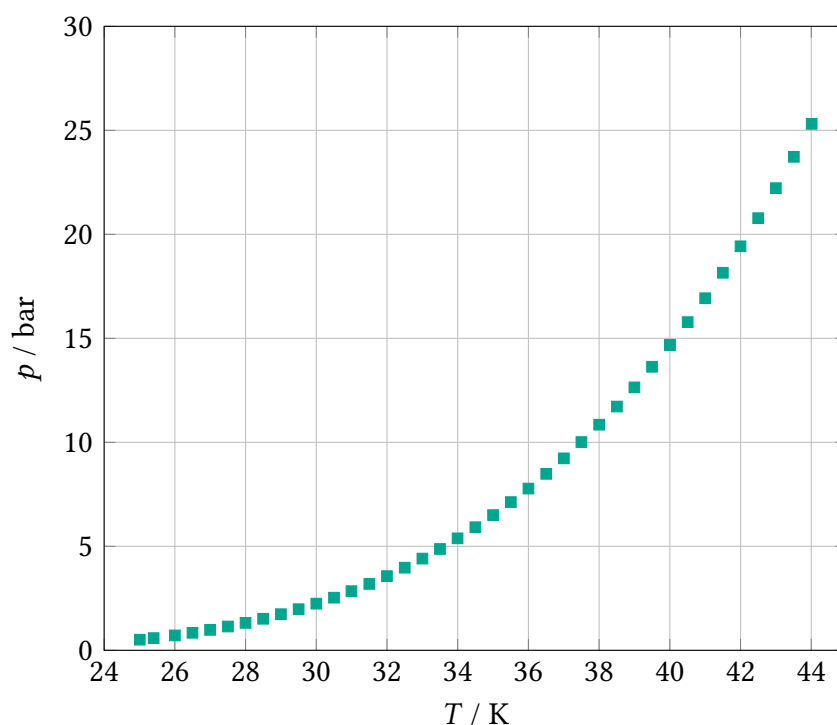
Figure 5.5.: Vapor pressure measurements of neon from 25 K to 44 K.

the impurities are helium, which have been removed by pumping on the frozen solid in the equilibrium cell. Neither the GC analysis before nor the one after impurity removal showed a second peak.

The results including measurement uncertainties are listed in Table 5.6 and plotted in Figure 5.5. The uncertainties have been determined by the equations derived in chapter 4. The temperature difference between the two sensors in the equilibrium cell ranges from 1 mK to 12 mK with an average difference of 6 mK. However, these differences are random and do not follow the increase of the expanded uncertainty of temperature, which can be seen in Table 5.6. The uncertainty of pressure increases linearly until the full-scale range of the low-pressure sensor is reached. The sudden increase is caused by the higher uncertainty of the mid-pressure sensor. At a temperature of 40 K, the phase separation line was no longer visible due to low liquid level in the equilibrium cell. Therefore, the cell has been re-filled and the data point has been re-measured in order to guarantee that the filling level has no impact on the measurement. The added gas has not been further purified, but all piping has been thoroughly evacuated and purged.

To put the new experimental data into context of the literature, the current reference EOS of Thol et al. is used as baseline. The deviations of selected literature data and the data of this work to the reference EoS are plotted in Figure 5.6. Also, the former reference EoS of Katti et al. [152] is included in the plots.

The new data set has low scattering, particularly when compared to other experimental data sets. The negative deviation of the data set of Grilly at temperatures ranging from 35 K to 44 K is not affirmed by the new data, neither is the data set of van't Zelfde and

Table 5.6.: Experimental results of the measurement of the vapor pressure of neon with the combined uncertainties $u_{\mathrm{abs}}(T, p)$ (with coverage factor $k = 2$).

T / K	p / bar	$u_{\mathrm{abs}}(T)$ / mK	$u_{\mathrm{abs}}(p)$ / mbar
25.008	0.511	13	1
25.400	0.586	13	1
26.000	0.716	13	1
26.499	0.842	13	1
26.997	0.984	13	1
27.501	1.145	13	1
28.000	1.319	14	1
28.497	1.517	14	1
28.999	1.736	14	1
29.501	1.976	14	1
30.001	2.244	14	1
30.501	2.530	15	1
30.995	2.844	15	2
31.500	3.192	15	2
31.998	3.565	15	2
32.502	3.972	15	2
33.002	4.410	16	2
33.499	4.871	16	2
33.996	5.384	15	2
34.499	5.918	15	2
35.001	6.499	16	2
35.502	7.125	16	3
36.001	7.776	16	3
36.504	8.485	16	3
37.002	9.230	17	3
37.499	10.010	16	3
38.001	10.848	16	10
38.503	11.721	16	10
38.998	12.641	17	10
39.497	13.633	17	10
40.000	14.680	17	10
40.001	14.680	17	10
40.505	15.778	17	10
41.000	16.927	17	10
41.499	18.152	18	10
41.999	19.424	18	10
42.499	20.776	18	10
42.999	22.219	18	10
43.507	23.727	18	10
44.012	25.312	19	10
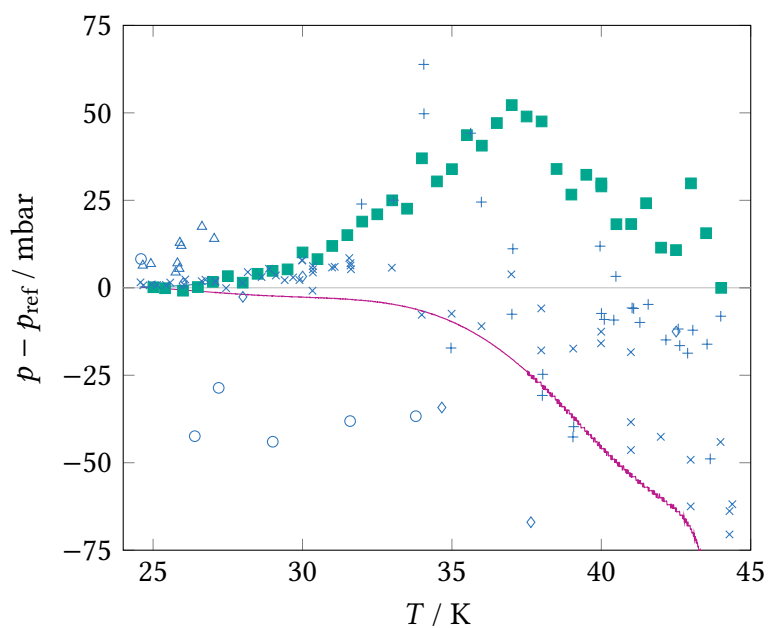
(a) Absolute pressure deviations of selected data to the reference EoS.
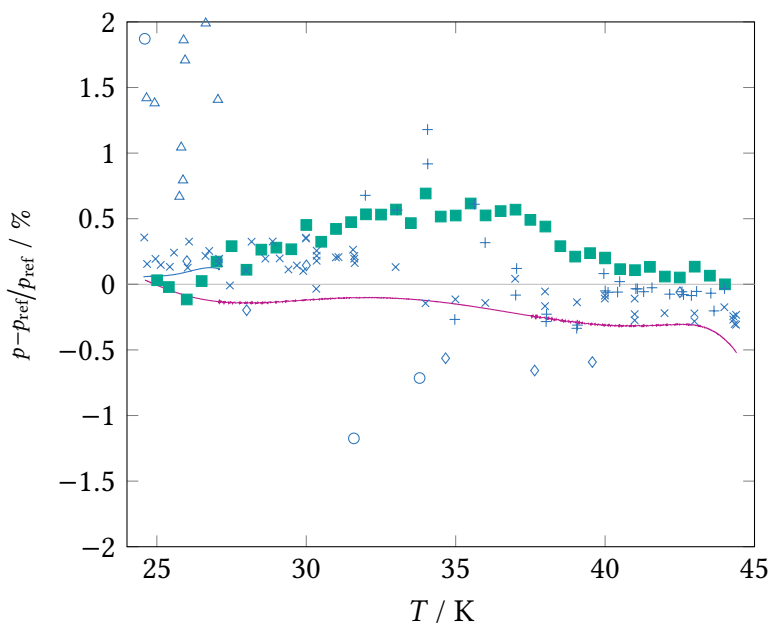
(b) Relative pressure deviations of selected data to the reference EoS.

Figure 5.6.: Deviations of experimental data sets (this work (■), Grilly [114] (×), Gibbons [154] (+), Heck and Barrick [13] (◇), Streett and Jones [100] (○), van't Zelfde and Dokoupil (△) [103]), Furukawa [36] (—) and the EoS of Katti et al. [152] (—) to the reference EoS of Thol et al. [151].

Dokoupil [103] at temperatures below the normal boiling point. It rather agrees with the data set of Gibbons and the high-quality data set of Furukawa [36].

The new data shows good agreement with the reference EoS close to the triple point and the critical point. The agreement close to the triple point proves accurate measurement, as the triple point of neon is a fix point. At intermediate temperatures, the new data has a slightly less pronounced curvature of the vapor pressure curve, i.e. slightly higher vapor pressures at fixed temperature or lower boiling temperatures at fixed pressure. The average absolute deviation is 20.4 mbar and the average relative deviation is 0.3 % with the highest deviation being 52.2 mbar and 0.57 % respectively.

Finally, the development of the current reference EoS of Thol et al. has significantly improved the description of the vapor pressure of neon, particularly above 35 K. Including the new data in future multiparameter modeling developments can likely further reduce the deviations.

5.3. VLE of the neon-helium system

The VLE of the neon-helium system is measured at two isotherms at 32.9 K and at 35.9 K up to pressures of 95 bar. Additionally, two data points are taken at 27.0 K. These temperatures are chosen for a direct comparison with available literature data from Knorn [14] and Heck and Barrick [13]. The new data has been measured by Frank within her Bachelor's thesis [163]. It is listed in Table 5.7 and plotted in Figure 5.7, which contains the VLE data of the two literature sources of Heck and Barrick [13] and Knorn [14] as well. A total of 28 data points are recorded, of which 11 are measured at 35.9 K, 14 at 32.9 K and only 3 at 27.0 K due to time constraints. The majority of the data consists of a complete set of $\{p, T, x, y\}$, while some liquid phase compositions are below the threshold of quantitative composition analysis. The uncertainty calculations for temperature, pressure and composition are described in section A.2, section A.3 and section A.4, respectively.

The three isotherms shown in Figure 5.7 neither indicate the occurrence of a LLE nor a gas-gas-equilibrium (GGE), although the pressure range of the experimental data is not sufficient to exclude the possibility of GGE formation. Considering that CryoPHAEQTS is the first test bench offering optical access to the VLE of the neon-helium system, LLE formation is not observed visually, either. Thus, at least in the temperature and pressure domain of technical interest, the neon-helium system behaves as type I mixture according to the classification of Konynenbourg and Scott [164]. Solving algorithms for EoS modeling the neon-helium system do not need to account for LLE and EoS (parameters), which predict LLEs at liquid neon temperatures, are not applicable.

Figure 5.7 cannot provide insights into the deviations between the three experimental data sources and the reference EoS due to the large scale of the plot. Figure 5.8 shows the boiling point and dew point curves of the two isotherms at 35.9 K and 32.9 K in separate plots including the uncertainty of the data of this work. Gibbs ensemble Monte Carlo (GEMC) simulations by Aasen et al. [15] and the current reference EoS of Tkaczuk et al. [17] are included in the plots as well. To evaluate deviations, a comparison of the dew point and boiling point pressures at constant composition is not of high significance, as the relative uncertainty of composition is at least one order of magnitude higher than
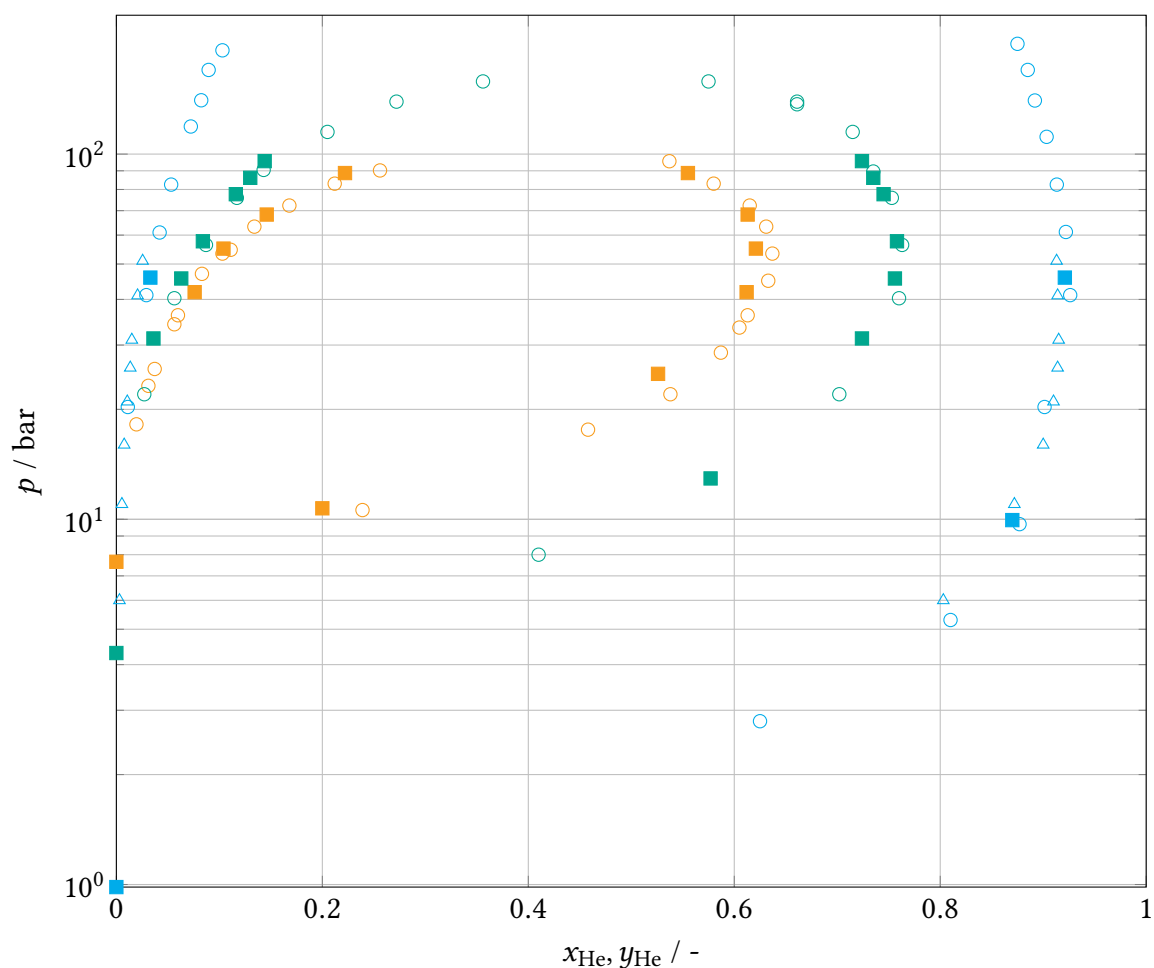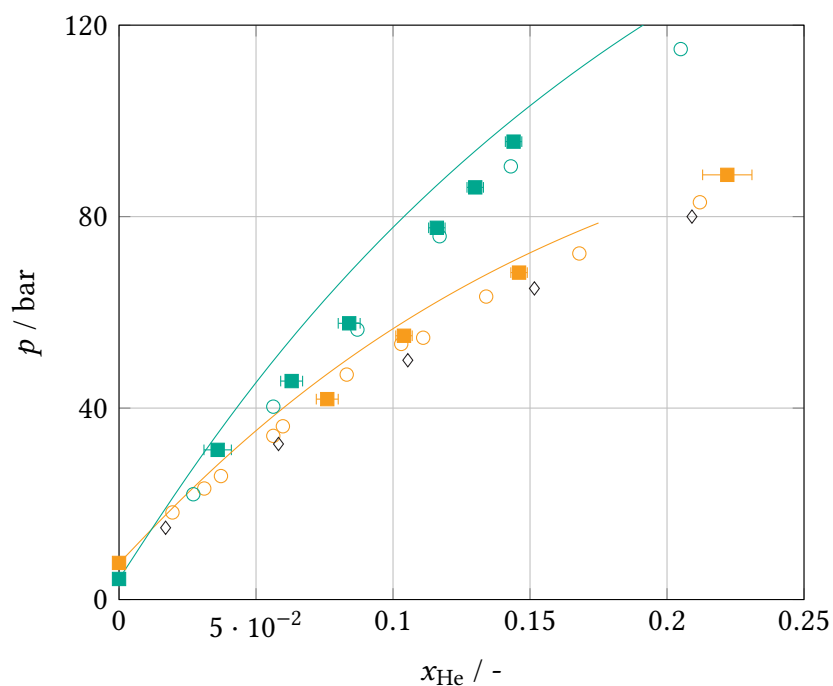
Figure 5.7.: Experimental VLE data at 35.9 K (orange), 32.9 K (green) and 27.0 K (blue) of Heck and Barrick (○), Knorn (△) and this work (■).

the pressure and temperature uncertainties. Therefore, the helium contents in the vapor and liquid phase at constant temperature and pressure should be used for comparison. Despite showing similar trends and a good overall agreement, the data of this work and the data of Heck and Barrick show systematic deviations of the helium content. In both, the liquid and the vapor phase, helium contents are lower than the data of Heck and Barrick. However, when assuming similar composition uncertainties, most of the deviations are not statistically significant. The pressure measurement cannot cause the systematic deviations as the stipulated uncertainties would need to be several orders of magnitude higher. The temperature measurement might represent an error source, e.g. by insufficient thermal contact or self-heating. However, it cannot cause a shift of the two-phase region to lower helium contents, as a temperature-induced decrease of the helium content in the liquid phase necessarily results in an increase of the helium content in the vapor phase. Hence, only a systematic error in the composition analysis can cause the deviations of the data of this work to the data of Heck and Barrick. It can either originate from the sampling process or from the calibration and analysis procedure in the GC system.

Table 5.7.: Experimental VLE data for the system helium (1) + neon (2) at temperature T, pressure p, liquid mole fraction x and vapor mole fraction y with respective combined uncertainties u (with coverage factor $k = 2$). Compositions, which are not quantitatively analysed are left empty. The pressure uncertainties according to GUM should be replaced by a systematic relative uncertainty of $u_{\mathrm{rel,\,syst}} = -0.1\,\%$ induced by the sampling process.

T / K	p / bar	x_1 / –	y_1 / –	$u(T)$ / mK	$u_{\mathrm{GUM}}(p)$ / mbar	$u(x_1)$ / –	$u(y_1)$ / –
35.915	7.652	0.000	0.000	16	1	0.000	0.000
35.924	10.718		0.200	16	1		0.005
35.911	25.021		0.526	16	1		0.005
35.886	41.871	0.076	0.612	16	3	0.004	0.014
35.892	55.114	0.104	0.621	16	3	0.003	0.013
35.882	68.305	0.146	0.613	16	5	0.003	0.014
35.879	88.728	0.222	0.555	16	8	0.009	0.006
32.902	4.304	0.000	0.000	15	1	0.000	0.000
32.895	12.939	0.036	0.577	15	1	0.005	0.005
32.896	31.275	0.063	0.724	15	3	0.004	0.005
32.881	45.646	0.084	0.756	15	4	0.004	0.004
32.886	57.713	0.116	0.758	15	7	0.004	0.004
32.876	77.667	0.130	0.745	15	15	0.003	0.005
32.871	86.113	0.144	0.735	15	11	0.003	0.005
32.855	95.669		0.724	15	9		0.005
27.018	9.950		0.870	13	1		0.008
26.985	45.903	0.033	0.921	13	2	0.006	0.002

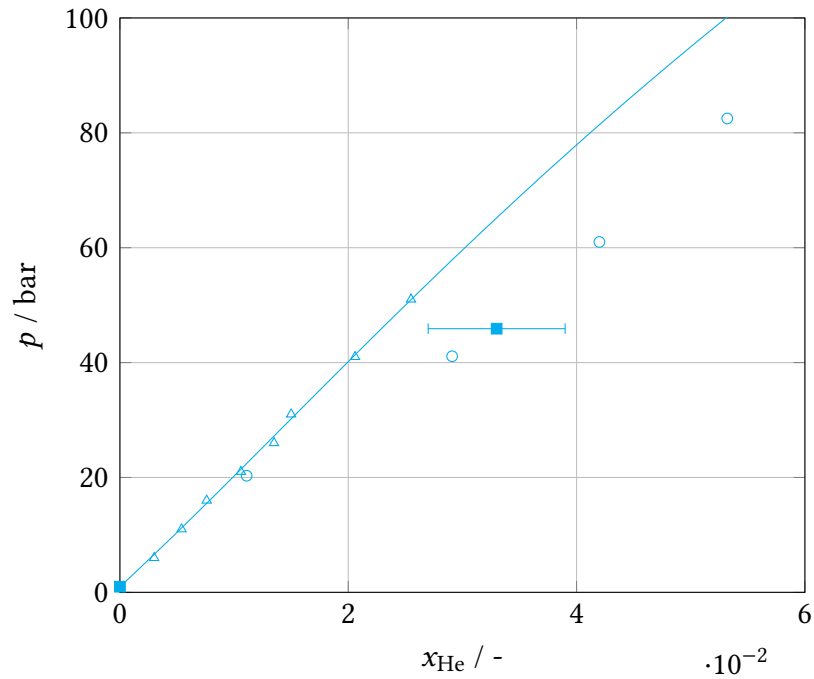(a) Enlarged section of Figure 5.7 with a focus on the boiling point curves.
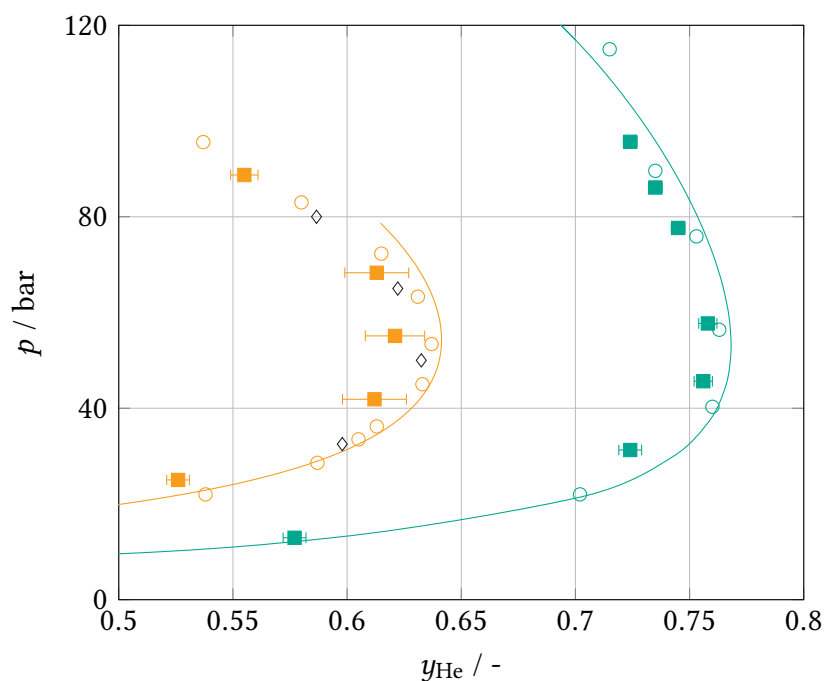
(b) Enlarged section of Figure 5.7 with a focus on the dew point curves.

Figure 5.8.: Experimental VLE data at 35.9 K (orange) and 32.9 K (green) of Heck and Barrick (∘) and this work (■) compared to the current reference EoS of Tkaczuk et al. (solid lines) and Gibbs ensemble Monte Carlo simulations of Aasen et al. (◇) [15].

(a) Boiling-point data.
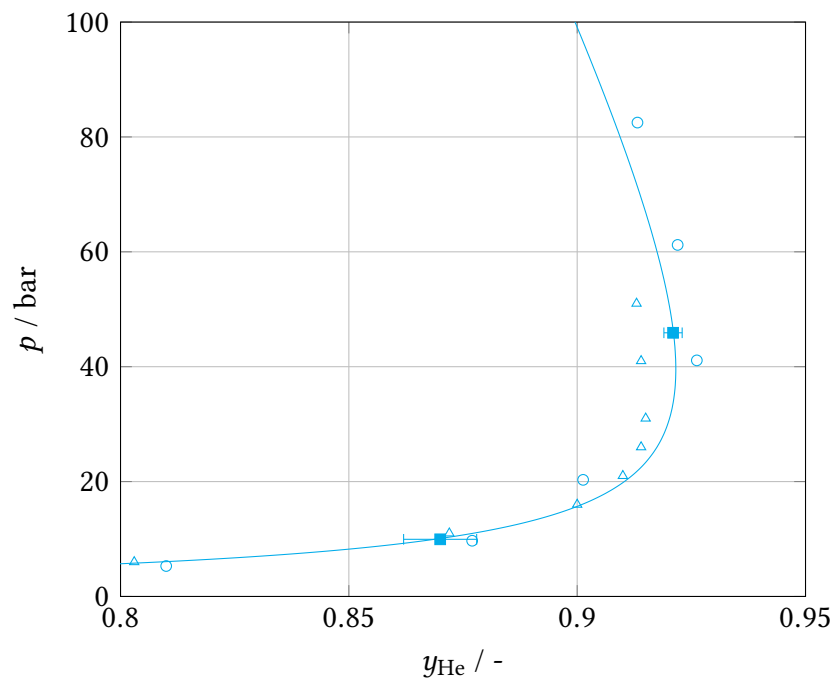
(b) Dew-point data.

Figure 5.9.: Discrepancies between the three experimental VLE data sets of Heck and Barrick (○), Knorn (△) and this work (■) at 27.0 K compared to the reference EoS of Tkaczuk et al. (solid lines) [17].

The isotherm at 27.0 K allows to compare the two data sets to a third one, which published by Knorn [14]. As this isotherm has a steep slope, it is enlarged in separate plots shown in Figure 5.9. Except for the data point at 20 bar, the data set of Heck and Barrick systematically deviates from the data set of Knorn to higher helium contents. Figure 5.9a shows that the EoS development of Tkaczuk et al. favours the data set of Knorn in this domain. Tkaczuk et al. and Aasen et al. argue that the linear extrapolation of a thermodynamically consistent boiling curve must result in the vapor pressure of pure neon, according to Henry's law. This consistency criterion is only met by the data set of Knorn. As the new data of this work only provides one data point, no definitive statement can be made, although it seems to agree with the data set of Heck and Barrick. When assuming a similar uncertainty of their data set to the uncertainty of this work, Henry's law might stand as well. As the new data at 27.0 K is scarce, it cannot reconcile the different shapes of the dew point curves shown in Figure 5.9b. It agrees well with the reference EoS of Tkaczuk et al. All data points of Knorn and about half of the data of Heck and Barrick has been used for parameter fitting. For the two isotherms at 35.9 K and 32.9 K, the reference EoS shows a slightly wider two-phase region, while the consideration of the data of Knorn leads to a shift to lower helium contents at 27.0 K. The GEMC simulation results of Aasen et al. indicate a slightly narrower two-phase region. In the following, some insights into the experimental methods and procedures of the three VLE data sources are given.

Experimental details of the data of this work

At the begin of the measurement campaign, pure neon is filled into the cell and its vapor pressure is measured. For the other data points on the isotherm, helium is added to the system leading to a small temperature peak of about 0.2 K and a pressure increase according to the charged amount of helium. Then, the gas circulator is turned on for 1 d to accelerate phase equilibration. After the gas circulator has been turned off, it takes another 1 d to 2 d for the temperature and the pressure to stabilise. Due to failure of the gas circulator, it could only be used for the isotherm at 35.9 K. For the other two isotherms, equilibration times up to 4 d were required. During the equilibration period, the excess helium in the vapor phase condenses into the liquid phase leading to a continuous pressure decrease. As only the cell wall temperatures are held constant, the two fluid temperatures may vary according to the filling level of the cell. In principle, the cell wall temperatures can be adjusted to yield constant fluid temperatures, but the equilibration times are too long to efficiently manipulate the set-points. Therefore, there is a temperature difference of up to 50 mK between the highest and the lowest temperature of an isotherm, as shown in Table 5.7.

Before sampling one of the phases, temperature and pressure data is recorded and their uncertainties are analysed. These values correspond to the table entries in Table 5.7. About (0.25 ± 0.10) bar are withdrawn from the vapor phase, while for the liquid phase, samples up to (1.0 ± 0.2) bar are necessary for quantitative analysis of the helium content. Both sampling procedures, as well as the initial purging of the sampling capillaries, lead to a considerable disturbance of the phase equilibrium up to pressure drops of 1 bar. The data is accepted, if the pressure increases to within $\pm 0.1\,\%$ of the initially recorded pressure after the sampling. Data with a higher pressure loss is discarded. As the sampling process

induces a non-constant, systematic error to the data, the stated pressure uncertainties according to GUM of the unperturbed system should be replaced by a relative systematic uncertainty of $u_{\text{rel, syst}} = -0.1\,\%$.

To tackle this disturbance issue, a buffer vessel, installed at ambient temperature, could increase the charged fluid amounts. Hence, the pressure drop induced by the removal of mass during sampling would be smaller. The influence of a higher fluid charge of the system on the equilibration time should be investigated beforehand. Another possibility is the use of rapid on-line sampler-injectors (ROLSI) [165]. ROLSI valves enable small sampling volumes, which are directly fed into a carrier gas stream leading to the GC system. Hence, five small samples can be withdrawn from the equilibrium cell and be analysed once in the GC instead of taking a bigger sample and analysing it five times. However, considerable leakage has been observed for operation with helium, which could not be resolved in maintenance. Therefore, the ROLSI valves have been replaced by a combination of a ball valve with a capillary restriction, a filter element and a needle valve to slow down gas flow during sampling. Nevertheless, the sample gas flow in the capillaries is still to high at elevated pressures, causing unrepeatable sample pressures.

Experimental details of the data of Heck and Barrick

Heck and Barrick have measured 6 isotherms (41.9 K, 38.9 K, 35.9 K, 32.9 K, 29.9 K, 26.9 K) up to pressures of 200 bar. An analytical method with vapor phase re-circulation is used. The equilibrium cell is cooled by the evaporation of a liquid hydrogen bath. The pressure is measured by two Heise gauges with respective measurement ranges of 100 bar and 300 bar. They claim uncertainties of 0.1 bar for pressures up to 100 bar and 0.3 bar for pressures above 100 bar. The temperature is measured at the top of the cell using a platinum resistance thermometer, which is calibrated on the NBS-55 scale. The temperature difference between the top of the cell and the fluid inside the cell is measured with a thermocouple. All sensor wiring is thermally anchored at a length of 3 m. Temperature uncertainties are stipulated to be within ±0.05 K. No statement is given about neither the composition uncertainty nor sampling amounts and equilibration times. Neon with impurities lower than 80 ppm and helium with impurities lower than 20 ppm is used, with most of the impurities being helium or neon, respectively. A special valve is used for sampling the respective phases and lead the samples into a GC system. Instead of an independent third gas, the major mixture component is used as carrier gas and the single resulting peak of the minor component is analysed. Thus, no separation of the two components is required. Three certified calibration mixtures are used for calibration of the GC system, which are claimed to be accurate within ±1 %. In a linear calibration curve domain, this peak is correlated to a composition through

$$x_{i,\text{sample}} = \frac{A_{i,\,\text{sample}}}{A_{i,\text{cert}}} x_{i,\text{cert}}, \tag{5.2}$$

with *i* being the minor component. However, the calibration curves are reported to be non-linear. Heck states that the non-linearity is corrected, but it is not clear, how this correction is achieved with only three available calibration mixtures. To judge the consistency of

the data, it has been smoothed and the scattering of the individual data points around the smooth curve has been evaluated yielding an *ARD* of ±3 %.

Experimental details of the data of Knorn

Knorn has focused on solubility measurements in the low temperature domain and reports 3 isotherms, ranging from 24.71 K to 27.03 K up to pressures of 51 bar with helium contents in the liquid phase up to $x_1 < 0.0256$. Cooling is provided by a cryogenic liquid bath. The temperature is measured by a platinum resistance thermometer, but no information about calibration or sensor location is given. The measurement interval to obtain one data point is given as 1 h. Author claimed uncertainties are ±0.02 K for temperature measurement, ±0.02 % and ±0.1 % for the liquid and vapor phase composition, respectively.

In conclusion, both, the data set of this work and the data set of Heck and Barrick are affected by possible systematic errors during sampling, equilibration or GC analysis. The data set of Knorn is thermodynamically consistent, but too little information is given to assess the validity of the uncertainty statement. The proposed optimisations of CryoPHAEQTS can reduce the systematic uncertainties and hence, provide reliable data. In particular, complete measurement of the isotherm at 27 K is beneficial for the reconciliation of the other two literature data sets.

6. Summary and outlook

The aim of this work is to provide precise physical property data of cryogenic fluid mixtures, which are crucial to the design of cryogenic mixed refrigerant cycles applied in hydrogen liquefaction or cooling of superconducting applications. Based on a literature review, state-of-the-art thermodynamic EoS for refrigerant mixtures are discussed. Particularly, the lack of property data for mixtures below 50 K is identified as a major obstacle for EoS development. This lack of data motivates the development of a test stand for the measurement of phase equilibria, the specific heat capacity of the vapor phase and transport properties with operation temperatures from 14 K to 300 K. In a first step, the cryogenic phase equilibria test stand CryoPHAEQTS is developed, set-up and commissioned with considerations for future upgrades with measurement methods for the heat capacity and transport properties.

First, the thermodynamic fundamentals are layed-out, which are necessary for the interpretation and modeling of the experimental data. A focus is set on phase equilibrium calculations and the thermodynamic treatment of experimental VLE data using consistency tests. EoS for property calculations of MRCs operated above 77 K are readily available and include cubic EoS, EoS based on perturbation theory and multiparameter EoS. Particularly for multi-component mixtures, the PC-SAFT EoS represents a good compromise between computing effort and accuracy.

Current EoS are not able to accurately describe cryogenic fluid mixtures below 50 K, which is commonly attributed to quantum effects arising at low temperatures. Except for the multiparameter EoS of Tkaczuk et al, none of the available EoS is able to accurately model the near-critical domain. The accuracy of caloric data cannot be judged, as only few VLE and density measurements and no caloric data is available for cryogenic fluid mixtures. By considering state-of-the-art experimental methods, the cryogenic phase equilibria test stand CryoPHAEQTS has been developed to provide such data.

For this purpose, an equilibrium cell is designed to withstand pressures up to 150 bar from room to cryogenic temperatures. It offers optical access, apertures for vapor phase re-circulation, pressure sensing and 3 sampling capillaries for VLLE measurements. Contrary to most phase equilibria test stands in the literature, the equilibrium cell is cooled by a pulse-tube cryocooler with compensation heating instead of an cryogenic liquid bath. The first stage of the cryocooler provides cooling power for an aluminum thermal radiation shield and the second stage of the cryocooler serves as constant temperature heat sink enabling fine-tuning of the upper and lower cell wall temperatures. A temperature control set-up is installed enabling thermal stabilities in the range of ± 2 mK. Temperatures are measured by CERNOX® sensors providing high sensitivity at cryogenic temperatures. A vapor phase re-circulation loop consisting of two double-pipe heat exchangers and a pre-cooling stage allows fast equilibration while minimising thermal disturbances. The safety

concept allows investigations of all non-toxic refrigerant mixtures, including flammable or oxidising.

CryoPHAEQTS is successfully validated against available literature data for the nitrogen-argon system with an *ARD* of 0.57 % for the bubble point and 0.46 % for the dew point to the current reference EoS. The target uncertainties of ±20 mK for temperature measurement, ±0.1 % for pressure measurement and ±1 % for composition analysis are reached. First measurement results are presented for the vapor pressure of neon, which considerably improve the existing data base. Particularly, the excellent agreement close the the triple point, which is temperature scale fix point, and the thermodynamically consistent curvature of the vapor pressure curve with low scatter of the data points indicates high quality data.

Finally, the VLE of neon-helium is investigated at two isotherms up to 95 bar. Next to two previous studies by Knorn and Heck and Barrick, the test stand provides a third data set, which is the first on the ITS-90 and with traceable uncertainty calculations. The absolute temperature uncertainties are below ±20 mK, the relative pressure uncertainties are below ±0.1 % and the relative composition uncertainties are below ±2 %. Due to systematic errors induced by the sampling process, the new data set cannot reconcile the discrepancies between the literature data sets. For a definitive evaluation, the three isotherms of Knorn should be investigated with a focus on the isotherm at 27.0 K, where data of Heck and Barrick is available as well.

Based on the commissioning and measurement experience, CryoPHAEQTS should be updated with the following features in order to further increase the accuracy of phase equilibrium measurements:

- A buffer vessel should be installed into the circulation loop at ambient temperature to increase the fluid charge and reduce relative sample volumes.
- A buffer vessel should be installed into the dosing system to allow reproducible mixture component addition.
- The influence of the carrier gas on the peak detection and resolution of neon-helium mixtures should be systematically investigated to allow composition analysis of neon-rich samples. Also, a replacement of hydrogen as carrier gas in the GC system allows the composition analysis of the ternary system He-Ne-H_2.

Additionally to VLE measurements, CryoPHAEQTS allows VLLE measurements as well. The knowledge of LLE formation of a refrigerant mixture is crucial because LLEs can lead to pinch points when they occur within the internal heat exchanger of an MRC. However, LLEs can be advantageous when they emerge within the evaporator offering a constant cooling temperature. As the test bench has optical access, crystallisation within a liquid phase, i.e. SLE, can be observed visually providing information of the minimal cooling temperature of a certain mixture.

In a second step, CryoPHAEQTS will be upgraded with the cryogenic thermal mass flow sensor for the measurement of the specific heat capacity of the vapor phase. As there are no caloric measurements of cryogenic fluid mixtures, this data is crucial to fit EoS parameters yielding consistent caloric property calculations.

In a final third step, the test stand will be equipped with a laser-optical system for the measurement of transport properties through DLS experiments. As this optical equipment

will be placed outside the cryostat, neither the scattered nor the incident light beam must be affected by the window material. While the cryostat is equipped with the required quartz glass windows, the sapphire glass windows of equilibrium cell must be replaced. The influence of the cool-down and warm-up processes on the thermal stress in the windows should be investigated with the current equilibrium cell design as it has not been tested with the additional thermal contacts of the loose flanges, yet. Also, one of the capillary feedthroughs must be replaced by a quartz glass window. With this final evolution step, CryoPHAEQTS will provide all necessary data for the design and development of (cryogenic) mixed refrigerant cycles.

Bibliography

[1] Saif ZS. Al Ghafri et al. "Hydrogen liquefaction: a review of the fundamental physics, engineering practice and future opportunities". In: *Energy & Environmental Science* 15.7 (2022), pp. 2690–2731. ISSN: 1754-5692. DOI: 10.1039/d2ee00099g.

[2] Wonsub Lim, Kwangho Choi, and Il Moon. "Current Status and Perspectives of Liquefied Natural Gas (LNG) Plant Design". In: *Industrial & engineering chemistry research* 52.9 (2013), pp. 3065–3088. ISSN: 0888-5885. DOI: 10.1021/ie302877g.

[3] Prue Hatcher, Rajab Khalilpour, and Ali Abbas. "Optimisation of LNG mixed-refrigerant processes considering operation and design objectives". In: *Computers & Chemical Engineering* 41 (2012), pp. 123–133. ISSN: 00981354. DOI: 10.1016/j.compchemeng.2012.03.005.

[4] Zbigniew Rogala. "Composition optimization method for mixed refrigerant MR JT cryocooler". In: *Cryogenics* 113 (2021), p. 103223. ISSN: 00112275. DOI: 10.1016/j.cryogenics.2020.103223.

[5] N. S. Walimbe, K. G. Narayankhedkar, and M. D. Atrey. "Experimental investigation on mixed refrigerant Joule–Thomson cryocooler with flammable and non-flammable refrigerant mixtures". In: *Cryogenics* 50.10 (2010), pp. 653–659. ISSN: 00112275. DOI: 10.1016/j.cryogenics.2010.06.002.

[6] Mikhail Boiarski, Oleg Podtcherniaev, and Kevin Flynn. "Comparative Performance of Throttle Cycle Cryotiger Coolers Operating with Different Mixed Refrigerants". In: *Cryocoolers 13*. Ed. by Ronald G. Ross. Boston, MA: Springer US, 2005, pp. 481–488. ISBN: 978-0-387-23901-9. DOI: 10.1007/0-387-27533-9{\textunderscore}61.

[7] European parliament. *Regulation (EU) No 517/2014 of the European parliament and of the council of 16 April 2014 on fluorinated greenhouse gases and repealing Regulation (EC) No 842/2006: EU517/2014*. 2014. URL: https://eur-lex.europa.eu/legal-content/DE/TXT/?uri=celex%3A32014R0517 (visited on 11/14/2022).

[8] D. Berstad et al. "Efficient Liquefaction of Hydrogen: Results of the IDEALHY Project". In: *Energire-Symposium, Stralsund/Germany*. 2013.

[9] Hans Quack et al. "Nelium, a Refrigerant with High Potential for the Temperature Range between 27 and 70 K". In: *Physics Procedia* 67 (2015), pp. 176–182. ISSN: 18753892. DOI: 10.1016/j.phpro.2015.06.031.

[10] S. Kloeppel et al. "Neon helium mixtures as a refrigerant for the FCC beam screen cooling: comparison of cycle design options". In: *IOP Conference Series: Materials Science and Engineering* 101 (2015), p. 012042. DOI: 10.1088/1757-899X/101/1/012042.

[11] F. Millet et al. "Preliminary Conceptual design of FCC-hh cryoplants: Linde evaluation". In: *IOP Conference Series: Materials Science and Engineering* 502 (2019), p. 012131. DOI: 10.1088/1757-899X/502/1/012131.

[12] Øivind Wilhelmsen et al. "Reducing the exergy destruction in the cryogenic heat exchangers of hydrogen liquefaction processes". In: *International Journal of Hydrogen Energy* 43.10 (2018), pp. 5033–5047. ISSN: 03603199. DOI: 10.1016/j.ijhydene.2018.01.094.

[13] C. K. Heck and P. L. Barrick. "Liquid-Vapor Phase Equilibria of the Neon-Normal Hydrogen System". In: *Advances in Cryogenic Engineering*. Ed. by K. D. Timmerhaus. Boston, MA: Springer US, 1966, pp. 349–355. ISBN: 978-1-4757-0524-9. DOI: 10.1007/978-1-4757-0522-5{\textunderscore}38.

[14] M. Knorn. "Vapour—liquid equilibria of the neon—helium system". In: *Cryogenics* 7.1-4 (1967), p. 177. ISSN: 00112275. DOI: 10.1016/S0011-2275(67)80063-8.

[15] Ailo Aasen et al. "Accurate quantum-corrected cubic equations of state for helium, neon, hydrogen, deuterium and their mixtures". In: *Fluid Phase Equilibria* 524 (2020), p. 112790. ISSN: 03783812. DOI: 10.1016/j.fluid.2020.112790.

[16] Georgios M. Kontogeorgis et al. "Industrial Requirements for Thermodynamic and Transport Properties: 2020". In: *Industrial & engineering chemistry research* 60.13 (2021), pp. 4987–5013. ISSN: 0888-5885. DOI: 10.1021/acs.iecr.0c05356.

[17] Jakub Tkaczuk et al. "Equations of State for the Thermodynamic Properties of Binary Mixtures for Helium-4, Neon, and Argon". In: *Journal of Physical and Chemical Reference Data* 49.2 (2020), p. 023101. ISSN: 0047-2689. DOI: 10.1063/1.5142275.

[18] Roland Span. *Multiparameter Equations of State: An Accurate Source of Thermodynamic Property Data*. Springer eBook Collection. Berlin and Heidelberg: Springer, 2000. ISBN: 978-3-642-08671-7. DOI: 10.1007/978-3-662-04092-8.

[19] Yonghua Huang, Guobang Chen, and Vincent Arp. "Debye equation of state for fluid helium-3". In: *The Journal of Chemical Physics* 125.5 (2006), p. 054505. ISSN: 0021-9606. DOI: 10.1063/1.2217010.

[20] Jaime Wisniak, Alexander Apelblat, and Hugo Segura. "An Assessment of Thermodynamic Consistency Tests for Vapor-Liquid Equilibrium Data". In: *Physics and Chemistry of Liquids* 35.1 (1997), pp. 1–58. ISSN: 0031-9104. DOI: 10.1080/00319109708030571.

[21] Otto Redlich and A. T. Kister. "Algebraic Representation of Thermodynamic Properties and the Classification of Solutions". In: *Industrial & Engineering Chemistry* 40.2 (1948), pp. 345–348. ISSN: 0019-7866. DOI: 10.1021/ie50458a036.

[22] E. F. G. Herington. "A thermodynamic test for the internal consistency of experimental data on volatility ratios". In: *Nature* 160.4070 (1947), p. 610. ISSN: 0028-0836. DOI: 10.1038/160610b0.

[23] Hendrick C. van Ness, Stanley M. Byer, and Richard E. Gibbs. "Vapor-Liquid equilibrium: Part I. An appraisal of data reduction methods". In: *AIChE Journal* 19.2 (1973), pp. 238–244. ISSN: 0001-1541. DOI: 10.1002/aic.690190206.

[24] Hendrick C. van Ness. "Thermodynamics in the treatment of (vapor + liquid) equilibria". In: *The Journal of Chemical Thermodynamics* 27.2 (1995), pp. 113–134. ISSN: 00219614. DOI: 10.1006/jcht.1995.0011.

[25] Aage Fredenslund, Jürgen Gmehling, and Peter Rasmussen. *Vapor-liquid equilibria using UNIFAC: A group-contribution method.* Amsterdam: Elsevier, 1977. ISBN: 0-444-41621-8.

[26] M. M. Abbott and H. C. van Ness. "An extension of Barker's method for reduction of VLE data". In: *Fluid Phase Equilibria* 1.1 (1977), pp. 3–11. ISSN: 03783812. DOI: 10.1016/0378-3812(77)80021-6.

[27] Alberto Bertucco, Massimiliano Barolo, and Nicola Elvassore. "Thermodynamic consistency of vapor-liquid equilibrium data at high pressure". In: *AIChE Journal* 43.2 (1997), pp. 547–554. ISSN: 0001-1541. DOI: 10.1002/aic.690430227.

[28] José O. Valderrama and Claudio A. Faúndez. "Thermodynamic consistency test of high pressure gas–liquid equilibrium data including both phases". In: *Thermochimica Acta* 499.1-2 (2010), pp. 85–90. ISSN: 00406031. DOI: 10.1016/j.tca.2009.11.006.

[29] Lars J. Christiansen and Aage Fredenslund. "Thermodynamic consistency using orthogonal collocation or computation of equilibrium vapor compositions at high pressures". In: *AIChE Journal* 21.1 (1975), pp. 49–57. ISSN: 0001-1541. DOI: 10.1002/aic.690210105.

[30] Kwang W. Won and John M. Prausnitz. "High-Pressure Vapor-Liquid Equilibria. Calculation of Partial Pressures from Total Pressure Data. Thermodynamic Consistency". In: *Industrial & Engineering Chemistry Fundamentals* 12.4 (1973), pp. 459–463. ISSN: 0196-4313. DOI: 10.1021/i160048a011.

[31] S. Kabelac. "Die Schallgeschwindigkeit als thermodynamische Zustandsgröße". In: *Forschung im Ingenieurwesen* 64.3 (1998), pp. 47–54. ISSN: 0015-7899. DOI: 10.1007/PL00010851.

[32] Jean-Noël Jaubert et al. "The impressive impact of including enthalpy and heat capacity of mixing data when parameterising equations of state. Application to the development of the E-PPR78 (Enhanced-Predictive-Peng-Robinson-78) model". In: *Fluid Phase Equilibria* 560 (2022), p. 113456. ISSN: 03783812. DOI: 10.1016/j.fluid.2022.113456.

[33] E. W. Lemmon et al. *NIST Standard Reference Database 23: Reference Fluid Thermodynamic and Transport Properties-REFPROP, Version 10.0, National Institute of Standards and Technology.* 2018. DOI: 10.18434/T4/1502528. URL: https://www.nist.gov/srd/refprop.

[34] J. P. M. Trusler, W. A. Wakeham, and M. P. Zarari. "Model intermolecular potentials and virial coefficients determined from the speed of sound". In: *Molecular Physics* 90.5 (1997), pp. 695–704. ISSN: 0026-8976. DOI: `10.1080/002689797172057`.

[35] Erdogan Kiran, ed. *Supercritical fluids: Fundamentals and applications ; Proceedings of the NATO Advanced Study Institute on Supercritical Fluids - Fundamentals and Applications, Kemer, Antalya, Turkey, July 12-24, 1998.* Vol. 366. NATO science series Series E, Applied sciences. Boston: Kluwer Acad. Publ, 2000. ISBN: 978-0-7923-6236-4. URL: `http://www.loc.gov/catdir/enhancements/fy0814/00028028-d.html`.

[36] George T. Furukawa. "Vapor Pressures of Natural Neon and of the Isotopes 20 Ne and 22 Ne from the Triple Point to the Normal Boiling Point". In: *Metrologia* 8.1 (1972), pp. 11–27. ISSN: 0026-1394. DOI: `10.1088/0026-1394/8/1/004`.

[37] *Equations of state for fluids and fluid mixtures.* Vol. 5. Experimental thermodynamics. Amsterdam: Elsevier, 2000. ISBN: 0-444-50384-6.

[38] Manson Benedict, George B. Webb, and Louis C. Rubin. "An Empirical Equation for Thermodynamic Properties of Light Hydrocarbons and Their Mixtures I. Methane, Ethane, Propane and n –Butane". In: *The Journal of Chemical Physics* 8.4 (1940), pp. 334–345. ISSN: 0021-9606. DOI: `10.1063/1.1750658`.

[39] K. E. Starling and J. E. Powers. "Enthalpy of Mixtures by Modified BWR Equation". In: *Industrial & Engineering Chemistry Fundamentals* 9.4 (1970), pp. 531–537. ISSN: 0196-4313. DOI: `10.1021/i160036a002`.

[40] Johannes Diderik van der Waals. *Over de Continuiteit van den Gas-en Vloeistoftoestand.* Vol. 1. Sijthoff, 1873.

[41] Giorgio Soave. "Equilibrium constants from a modified Redlich-Kwong equation of state". In: *Chemical Engineering Science* 27.6 (1972), pp. 1197–1203. ISSN: 00092509. DOI: `10.1016/0009-2509(72)80096-4`.

[42] Ding-Yu Peng and Donald B. Robinson. "A New Two-Constant Equation of State". In: *Industrial & Engineering Chemistry Fundamentals* 15.1 (1976), pp. 59–64. ISSN: 0196-4313. DOI: `10.1021/i160057a011`.

[43] Yohann Le Guennec et al. "A consistency test for alpha-functions of cubic equations of state". In: *Fluid Phase Equilibria* 427 (2016), pp. 513–538. ISSN: 03783812. DOI: `10.1016/j.fluid.2016.07.026`.

[44] Norman F. Carnahan and Kenneth E. Starling. "Equation of State for Nonattracting Rigid Spheres". In: *The Journal of Chemical Physics* 51.2 (1969), pp. 635–636. ISSN: 0021-9606. DOI: `10.1063/1.1672048`.

[45] Ya Song Wei and Richard J. Sadus. "Equations of state for the calculation of fluid-phase equilibria". In: *AIChE Journal* 46.1 (2000), pp. 169–196. ISSN: 0001-1541. DOI: `10.1002/aic.690460119`.

[46] André Péneloux, Evelyne Rauzy, and Richard Fréze. "A consistent correction for Redlich-Kwong-Soave volumes". In: *Fluid Phase Equilibria* 8.1 (1982), pp. 7–23. ISSN: 03783812. DOI: `10.1016/0378-3812(82)80002-2`.

[47] Yohann Le Guennec, Romain Privat, and Jean-Noël Jaubert. "Development of the translated-consistent tc-PR and tc-RK cubic equations of state for a safe and accurate prediction of volumetric, energetic and saturation properties of pure compounds in the sub- and super-critical domains". In: *Fluid Phase Equilibria* 429 (2016), pp. 301–312. ISSN: 03783812. DOI: 10.1016/j.fluid.2016.09.003.

[48] Jean-Noël Jaubert et al. "Note on the properties altered by application of a Péneloux–type volume translation to an equation of state". In: *Fluid Phase Equilibria* 419 (2016), pp. 88–95. ISSN: 03783812. DOI: 10.1016/j.fluid.2016.03.012.

[49] Dirk Winkelmann. "Experimentelle Untersuchungen von Tieftemperatur Phasengleichgewichten von Kältemittelgemischen". Dissertation. Karlsruhe: Karlsruhe Institute of Technology, 2013.

[50] Hasan Orbey and Stanley I. Sandler. *Modeling vapor-liquid equilibria: Cubic equations of state and their mixing rules*. 1. publ. Cambridge series in chemical engineering. Cambridge: Cambridge Univ. Press, 1998. ISBN: 0-521-62027-9.

[51] Vineed Narayanan and G. Venkatarathnam. "Prediction of vapour-liquid equilibria of neon-nitrogen, neon-oxygen and neon-argon mixtures used in J-T refrigerators". In: *Cryogenics* 106 (2020), p. 103039. ISSN: 00112275. DOI: 10.1016/j.cryogenics.2020.103039.

[52] Nikolaos I. Diamantonis et al. "Evaluation of Cubic, SAFT, and PC-SAFT Equations of State for the Vapor–Liquid Equilibrium Modeling of CO_2 Mixtures with Other Gases". In: *Industrial & engineering chemistry research* 52.10 (2013), pp. 3933–3942. ISSN: 0888-5885. DOI: 10.1021/ie303248q.

[53] Robert W. Zwanzig. "High–Temperature Equation of State by a Perturbation Method. I. Nonpolar Gases". In: *The Journal of Chemical Physics* 22.8 (1954), pp. 1420–1426. ISSN: 0021-9606. DOI: 10.1063/1.1740409.

[54] M. S. Wertheim. "Fluids with highly directional attractive forces. I. Statistical thermodynamics". In: *Journal of Statistical Physics* 35.1-2 (1984), pp. 19–34. ISSN: 0022-4715. DOI: 10.1007/BF01017362.

[55] M. S. Wertheim. "Fluids with highly directional attractive forces. II. Thermodynamic perturbation theory and integral equations". In: *Journal of Statistical Physics* 35.1-2 (1984), pp. 35–47. ISSN: 0022-4715. DOI: 10.1007/BF01017363.

[56] M. S. Wertheim. "Fluids with highly directional attractive forces. III. Multiple attraction sites". In: *Journal of Statistical Physics* 42.3-4 (1986), pp. 459–476. ISSN: 0022-4715. DOI: 10.1007/BF01127721.

[57] M. S. Wertheim. "Fluids with highly directional attractive forces. IV. Equilibrium polymerization". In: *Journal of Statistical Physics* 42.3-4 (1986), pp. 477–492. ISSN: 0022-4715. DOI: 10.1007/BF01127722.

[58] J. A. Barker and D. Henderson. "Perturbation Theory and Equation of State for Fluids. II. A Successful Theory of Liquids". In: *The Journal of Chemical Physics* 47.11 (1967), pp. 4714–4721. ISSN: 0021-9606. DOI: 10.1063/1.1701689.

[59] J. A. Barker and D. Henderson. "Perturbation Theory and Equation of State for Fluids: The Square–Well Potential". In: *The Journal of Chemical Physics* 47.8 (1967), pp. 2856–2861. ISSN: 0021-9606. DOI: 10.1063/1.1712308.

[60] Thomas Lafitte et al. "Accurate statistical associating fluid theory for chain molecules formed from Mie segments". In: *The Journal of Chemical Physics* 139.15 (2013), p. 154504. ISSN: 0021-9606. DOI: 10.1063/1.4819786.

[61] Walter G. Chapman, George Jackson, and Keith E. Gubbins. "Phase equilibria of associating fluids". In: *Molecular Physics* 65.5 (1988), pp. 1057–1079. ISSN: 0026-8976. DOI: 10.1080/00268978800101601.

[62] Walter G. Chapman et al. "New reference equation of state for associating liquids". In: *Industrial & engineering chemistry research* 29.8 (1990), pp. 1709–1721. ISSN: 0888-5885. DOI: 10.1021/ie00104a021.

[63] Alejandro Gil-Villegas et al. "Statistical associating fluid theory for chain molecules with attractive potentials of variable range". In: *The Journal of Chemical Physics* 106.10 (1997), pp. 4168–4186. ISSN: 0021-9606. DOI: 10.1063/1.473101.

[64] Clare McCabe et al. "Predicting the High-Pressure Phase Equilibria of Binary Mixtures of Perfluoro- n -alkanes + n -Alkanes Using the SAFT-VR Approach". In: *The Journal of Physical Chemistry B* 102.41 (1998), pp. 8060–8069. ISSN: 1520-6106. DOI: 10.1021/jp982331s.

[65] Joachim Gross and Gabriele Sadowski. "Perturbed-Chain SAFT: An Equation of State Based on a Perturbation Theory for Chain Molecules". In: *Industrial & engineering chemistry research* 40.4 (2001), pp. 1244–1260. ISSN: 0888-5885. DOI: 10.1021/ie0003887.

[66] Yuan-Hao Fu and Stanley I. Sandler. "A Simplified SAFT Equation of State for Associating Compounds and Mixtures". In: *Industrial & engineering chemistry research* 34.5 (1995), pp. 1897–1909. ISSN: 0888-5885. DOI: 10.1021/ie00044a042.

[67] Ana M. A. Dias et al. "Vapor−Liquid Equilibrium of Carbon Dioxide−Perfluoroalkane Mixtures: Experimental Data and SAFT Modeling". In: *Industrial & engineering chemistry research* 45.7 (2006), pp. 2341–2350. ISSN: 0888-5885. DOI: 10.1021/ie051017z.

[68] Nicolás Ramírez-Vélez et al. "Parameterization of SAFT Models: Analysis of Different Parameter Estimation Strategies and Application to the Development of a Comprehensive Database of PC-SAFT Molecular Parameters". In: *Journal of Chemical & Engineering Data* 65.12 (2020), pp. 5920–5932. ISSN: 0021-9568. DOI: 10.1021/acs.jced.0c00792.

[69] Romain Privat, Rafiqul Gani, and Jean-Noël Jaubert. "Are safe results obtained when the PC-SAFT equation of state is applied to ordinary pure chemicals?" In: *Fluid Phase Equilibria* 295.1 (2010), pp. 76–92. ISSN: 03783812. DOI: 10.1016/j.fluid.2010.03.041.

[70] Chenyang Zhu et al. "Heat Capacities of Fluids: The Performance of Various Equations of State". In: *Journal of Chemical & Engineering Data* 65.12 (2020), pp. 5654–5676. ISSN: 0021-9568. DOI: 10.1021/acs.jced.0c00649.

[71] M. F. Alfradique and M. Castier. "Calculation of Phase Equilibrium of Natural Gases with the Peng-Robinson and PC-SAFT Equations of State". In: *Oil & Gas Science and Technology - Revue de l'IFP* 62.5 (2007), pp. 707–714. ISSN: 1294-4475. DOI: 10.2516/ogst:2007050.

[72] Alvaro Vidal, Phoevos Koukouvinis, and Manolis Gavaises. "Vapor-liquid equilibrium calculations at specified composition, density and temperature with the perturbed chain statistical associating fluid theory (PC-SAFT) equation of state". In: *Fluid Phase Equilibria* 521 (2020), p. 112661. ISSN: 03783812. DOI: 10.1016/j.fluid.2020.112661.

[73] U. Setzmann and W. Wagner. "A New Equation of State and Tables of Thermodynamic Properties for Methane Covering the Range from the Melting Line to 625 K at Pressures up to 100 MPa". In: *Journal of Physical and Chemical Reference Data* 20.6 (1991), pp. 1061–1155. ISSN: 0047-2689. DOI: 10.1063/1.555898.

[74] O. Kunz and W. Wagner. "The GERG-2008 Wide-Range Equation of State for Natural Gases and Other Mixtures: An Expansion of GERG-2004". In: *Journal of Chemical & Engineering Data* 57.11 (2012), pp. 3032–3091. ISSN: 0021-9568. DOI: 10.1021/je300655b.

[75] S. Kim, D. Henderson, and J. A. Barker. "Perturbation theory of fluids and deviations from classical behavior". In: *Canadian Journal of Physics* 47.1 (1969), pp. 99–102. ISSN: 0008-4204. DOI: 10.1139/p69-012.

[76] P. L. Chueh and J. M. Prausnitz. "Vapor-Liquid Equilibria at High Pressures. Vapor-Phase Fugacity Coefficients in Nonpolar and Quantum-Gas Mixtures". In: *Industrial & Engineering Chemistry Fundamentals* 6.4 (1967), pp. 492–498. ISSN: 0196-4313. DOI: 10.1021/i160024a003.

[77] Kaanapuli Ramkumar, Swati Swagatika Mishra, and Sudeep Bhattacharjee. *Accounting For Quantum Phenomena In Classical Molecular Dynamics Simulations At Cryogenic Temperatures: Diffraction And The Feynman-Hibbs Correction*. 2022. DOI: 10.48550/arXiv.2211.05154.

[78] Long Meng and Yuan-Yuan Duan. "An extended correlation for second virial coefficients of associated and quantum fluids". In: *Fluid Phase Equilibria* 258.1 (2007), pp. 29–33. ISSN: 03783812. DOI: 10.1016/j.fluid.2007.05.010.

[79] J. de Boer. "Quantum theory of condensed permanent gases I the law of corresponding states". In: *Physica* 14.2-3 (1948), pp. 139–148. ISSN: 00318914. DOI: 10.1016/0031-8914(48)90032-9.

[80] Roger H. Newton. "Activity Coefficients of Gases". In: *Industrial & Engineering Chemistry* 27.3 (1935), pp. 302–306. ISSN: 0019-7866. DOI: 10.1021/ie50303a014.

[81] Darren Rowland, Thomas J. Hughes, and Eric F. May. "Effective Critical Constants for Helium for Use in Equations of State for Natural Gas Mixtures". In: *Journal of Chemical & Engineering Data* 62.9 (2017), pp. 2799–2811. ISSN: 0021-9568. DOI: 10.1021/acs.jced.7b00122.

[82] Richard A. Messerly et al. "Molecular Calculation of the Critical Parameters of Classical Helium". In: *Journal of Chemical & Engineering Data* 65.3 (2020), pp. 1028–1037. ISSN: 0021-9568. DOI: 10.1021/acs.jced.9b00443.

[83] Masahiro KATO and Hiroyuki TANAKA. "Vapor-liquid equilibrium prediction with pseudo-cubic equation of state for binary mixtures containing hydrogen, helium, or neon". In: *Journal of The Japan Petroleum Institute* 33.2 (1990), pp. 99–103. ISSN: 0582-4664. DOI: 10.1627/jpi1958.33.99.

[84] Ulrich K. Deiters and Richard J. Sadus. "Ab Initio Interatomic Potentials and the Classical Molecular Simulation Prediction of the Thermophysical Properties of Helium". In: *The Journal of Physical Chemistry B* 124.11 (2020), pp. 2268–2276. ISSN: 1520-6106. DOI: 10.1021/acs.jpcb.9b11108.

[85] R. D. Gunn, P. L. Chueh, and J. M. Prausnitz. "Prediction of thermodynamic properties of dense gas mixtures containing one or more of the quantum gases". In: *AIChE Journal* 12.5 (1966), pp. 937–941. ISSN: 0001-1541. DOI: 10.1002/aic.690120519.

[86] K. A. Solen, P. L. Chueh, and J. M. Prausnitz. "Thermodynamics of Helium Solubility in Cryogenic Solvents at High Pressures". In: *Industrial & Engineering Chemistry Process Design and Development* 9.2 (1970), pp. 310–317. ISSN: 0196-4305. DOI: 10.1021/i260034a025.

[87] Shayan Kaviani, Farzaneh Feyzi, and Bahareh Khosravi. "Modification of the Peng–Robinson equation of state for helium in low temperature regions". In: *Physics and Chemistry of Liquids* 54.4 (2016), pp. 542–551. ISSN: 0031-9104. DOI: 10.1080/00319104.2015.1126836.

[88] Ilya Polishuk. "About the numerical pitfalls characteristic for SAFT EOS models". In: *Fluid Phase Equilibria* 298.1 (2010), pp. 67–74. ISSN: 03783812. DOI: 10.1016/j.fluid.2010.07.003.

[89] Ailo Aasen et al. "Equation of state and force fields for Feynman-Hibbs-corrected Mie fluids. II. Application to mixtures of helium, neon, hydrogen, and deuterium". In: *The Journal of Chemical Physics* 152.7 (2020), p. 074507. ISSN: 0021-9606. DOI: 10.1063/1.5136079.

[90] Ailo Aasen et al. "Equation of state and force fields for Feynman–Hibbs-corrected Mie fluids. I. Application to pure helium, neon, hydrogen, and deuterium". In: *The Journal of Chemical Physics* 151.6 (2019), p. 064508. ISSN: 0021-9606. DOI: 10.1063/1.5111364.

[91] Sergio Contreras, César Serna, and Alejandro Gil-Villegas. "Molecular thermodynamics of a quantum Lennard-Jones fluid using an effective Mie potential and the SAFT-VR-Mie approach". In: *Molecular Physics* 116.21-22 (2018), pp. 3425–3433. ISSN: 0026-8976. DOI: 10.1080/00268976.2018.1510142.

[92] César Serna and Alejandro Gil-Villegas. "Molecular thermodynamics of quantum square-well fluids using a path-integral perturbation theory". In: *Molecular Physics* 114.18 (2016), pp. 2700–2716. ISSN: 0026-8976. DOI: 10.1080/00268976.2016.1173732.

[93] Víctor M. Trejos and Alejandro Gil-Villegas. "Semiclassical approach to model quantum fluids using the statistical associating fluid theory for systems with potentials of variable range". In: *The Journal of Chemical Physics* 136.18 (2012), p. 184506. ISSN: 0021-9606. DOI: 10.1063/1.4712299.

[94] Nils von Preetzmann and Roland Span. "Density Measurements on Binary Helium+ Neon Mixtures over the Temperature Range from (100 to 233) K at Pressures up to 10 MPa". In: *Energy* 2004 (2022), p. 2965.

[95] Ralf Dohrn, José M. S. Fonseca, and Stephanie Peper. "Experimental methods for phase equilibria at high pressures". In: *Annual review of chemical and biomolecular engineering* 3 (2012), pp. 343–367. ISSN: 1947-5438. DOI: 10.1146/annurev-chembioeng-062011-081008.

[96] Toshihiko Yamanishi et al. "Liquid-vapor equilibrium in binary systems for He in n-hydrogen, hydrogen deuteride, and n-deuterium under ordinary pressure". In: *The Journal of Physical Chemistry* 96.5 (1992), pp. 2284–2289. ISSN: 0022-3654. DOI: 10.1021/j100184a048.

[97] Leonard O. Roellig and Clayton Giese. "Solubility of Helium in Liquid Hydrogen". In: *The Journal of Chemical Physics* 37.1 (1962), pp. 114–116. ISSN: 0021-9606. DOI: 10.1063/1.1732930.

[98] W. B. Streett, R. E. Sonntag, and G. J. van Wylen. "Liquid—Vapor Equilibrium in the System Normal Hydrogen—Helium". In: *The Journal of Chemical Physics* 40.5 (1964), pp. 1390–1395. ISSN: 0021-9606. DOI: 10.1063/1.1725322.

[99] J. P. Brouwer et al. "Phase separation in the liquid mixture of neon and deuterium". In: *Physica* 30.7 (1964), pp. 1409–1420. ISSN: 00318914. DOI: 10.1016/0031-8914(64)90089-8.

[100] W. B. Streett and C. H. Jones. "Liquid Phase Separation and Liquid—Vapor Equilibrium in the System Neon—Hydrogen". In: *The Journal of Chemical Physics* 42.11 (1965), pp. 3989–3994. ISSN: 0021-9606. DOI: 10.1063/1.1695872.

[101] R. E. Sonntag, G. J. van Wylen, and R. W. Crain. "Liquid—Vapor Equilibrium in the System Equilibrium Hydrogen—Helium". In: *The Journal of Chemical Physics* 41.8 (1964), pp. 2399–2402. ISSN: 0021-9606. DOI: 10.1063/1.1726277.

[102] C. M. Sneed, R. E. Sonntag, and G. J. van Wylen. "Helium–Hydrogen Liquid–Vapor Equilibrium to 100 atm". In: *The Journal of Chemical Physics* 49.5 (1968), pp. 2410–2414. ISSN: 0021-9606. DOI: 10.1063/1.1670414.

[103] P. Van't Zelfde and Z. Dokoupil. "Some vapour-pressure measurements of the condensed system Ne-H2 near the triple point of Ne". In: *Physica* 74.2 (1974), pp. 423–434. ISSN: 00318914. DOI: 10.1016/0031-8914(74)90135-9.

[104]   M. J. Hiza. "Liquid-vapor equilibria in binary systems containing 4He or 3He with nH2 or nD2". In: *Fluid Phase Equilibria* 6.3-4 (1981), pp. 203–227. ISSN: 03783812. DOI: `10.1016/0378-3812(81)85005-4`.

[105]   *Experimental thermodynamics of non-reacting fluids*. Vol. v. 2. Experimental thermodynamics. London: Butterworths, 1975. ISBN: 0408705663. URL: `https://www.sciencedirect.com/science/book/9780408705660`.

[106]   Kai Zhang et al. "Metagel with Broadband Tunable Acoustic Properties Over Air–Water–Solid Ranges". In: *Advanced Functional Materials* 29.38 (2019), p. 1903699. ISSN: 1616-301X. DOI: `10.1002/adfm.201903699`.

[107]   V. V. Pashkov, E. V. Konovodchenko, and O. V. Evdoklmova. "Velocity of ultrasound propagation in solutions of helium in cryogenic liquids". In: *Journal of Engineering Physics* 51.4 (1986), pp. 1197–1201. ISSN: 0022-0841. DOI: `10.1007/BF00870846`.

[108]   D. Güsewell, F. Schmeissner, and J. Schmid. "Density and sound velocity of saturated liquid neon-hydrogen and neon-deuterium mixtures between 25 and 31 K". In: *Cryogenics* 10.2 (1970), pp. 150–154. ISSN: 00112275. DOI: `10.1016/0011-2275(70)90087-1`.

[109]   D. Güsewell, F. Schmeissner, and J. Schmid. "New data on liquid neon-hydrogen mixtures". In: *Cryogenics* 11.4 (1971), pp. 311–313. ISSN: 00112275. DOI: `10.1016/0011-2275(71)90192-5`.

[110]   A. P. Fröba. "Dynamic light scattering (DLS) for the characterization of working fluids in chemical and energy engineering, Habil". PhD thesis. Thesis, Friedrich-Alexander-University Erlangen-Nuremberg, Erlangen, 2009.

[111]   Jakub Tkaczuk. "Equations of state for the thermodynamic properties of cryogenic mixtures". Theses. Université Grenoble Alpes [2020-....], 2021. URL: `https://theses.hal.science/tel-03729121`.

[112]   James Karl Hoffer. "The Thermodynamic Properties of He4 Near the Melting Line". PhD Thesis. Berkely: University of California, 1968.

[113]   C. Gladun. "The specific heat at constant volume of liquid neon". In: *Cryogenics* 6.1 (1966), pp. 27–30. ISSN: 00112275. DOI: `10.1016/S0011-2275(96)90059-4`.

[114]   E.R Grilly. "The vapour pressure of solid and liquid neon". In: *Cryogenics* 2.4 (1962), pp. 226–229. ISSN: 00112275. DOI: `10.1016/0011-2275(62)90056-5`.

[115]   J. P. Brouwer, C.J.N. van den Meijdenberg, and J.J.M. Beenakker. "Specific heat of the liquid mixtures of neon and hydrogen isotopes in the phase-separation region". In: *Physica* 50.1 (1970), pp. 93–124. ISSN: 00318914. DOI: `10.1016/0031-8914(70)90056-X`.

[116]   S. Grohmann. "A new method for flow measurement in cryogenic systems". In: *Cryogenics* 60 (2014), pp. 9–18. ISSN: 00112275. DOI: `10.1016/j.cryogenics.2014.01.004`.

[117]   Andreas Janzen. "Entwicklung eines neuen Messverfahrens zur Durchflussmessung in der Kryotechnik". Dissertation.

[118] J.B Ubbink. "Pressure dependence of the coefficient of heat conductivity for the gases helium and hydrogen at low temperatures". In: *Physica* 13.10 (1947), pp. 659–668. ISSN: 00318914. DOI: 10.1016/0031-8914(47)90058-X.

[119] D. E. Diller and H. M. Roder. "Thermal Conductivity Measurements on Fluid Hydrogen at 17 to 200°K and Pressures to 10 MN/m2". In: *Advances in Cryogenic Engineering*. Ed. by K. D. Timmerhaus. Boston, MA: Springer US, 1995, pp. 58–64. ISBN: 978-1-4757-0515-7. DOI: 10.1007/978-1-4757-0513-3{\textunderscore}9.

[120] J. Tamson, M. Stamm, and S. Grohmann. "Set-up of the cryogenic phase equilibria test stand CryoPHAEQTS". In: *IOP Conference Series: Materials Science and Engineering* 502 (2019), p. 012087. DOI: 10.1088/1757-899X/502/1/012087.

[121] J. Tamson, P. Blanck, and S. Grohmann. "Commissioning of the Cryogenic Phase Equilibria Test Stand CryoPHAEQTS". In: *IOP Conference Series: Materials Science and Engineering* 755.1 (2020), p. 012150. DOI: 10.1088/1757-899X/755/1/012150.

[122] Julia Weiler. *ERC Advanced Grant: Die Grundlage für eine Wasserstoffwirtschaft legen.* 2022. URL: https://news.rub.de/presseinformationen/wissenschaft/2022-04-26-erc-advanced-grant-die-grundlagen-fuer-eine-wasserstoffwirtschaft-legen (visited on 12/13/2022).

[123] M. Mair. "Messung des Dampf-Fluessig-Gleichgewichts des Stickstoff-Argon-Systems". Bachelor's thesis. Germany: Karlsruhe Institute of Technology, 2021.

[124] VDI e. V. *VDI Heat Atlas.* Berlin, Heidelberg: Springer Berlin Heidelberg, 2010. ISBN: 978-3-540-77876-9. DOI: 10.1007/978-3-540-77877-6.

[125] Nikolaus Rott. "Thermally driven acoustic oscillations. Part II: Stability limit for helium". In: *Zeitschrift für angewandte Mathematik und Physik ZAMP* 24.1 (1973), pp. 54–72. ISSN: 0044-2275. DOI: 10.1007/BF01593998.

[126] Youfan Gu and Klaus D. Timmerhaus. "Experimental Verification of Stability Characteristics for Thermal Acoustic Oscillations in a Liquid Helium System". In: *Advances in Cryogenic Engineering*. Ed. by Peter Kittel. Boston, MA: Springer US, 1994, pp. 1733–1740. ISBN: 978-1-4615-2522-6. DOI: 10.1007/978-1-4615-2522-6{\textunderscore}212.

[127] Christoph Stiller. *Grundlagen der Mess- und Regelungstechnik: Zugl.: Karlsruhe, Univ., Diss, 2006.* Berichte aus der Steuerungs- und Regelungstechnik. Aachen: Shaker, 2006. ISBN: 3832255826.

[128] Deutsches Institut fuer Normung. *DIN EN ISO 21013-3:2016-12, Kryo-Behälter_-Druckentlastungseinrichtungen für den Kryo-Betrieb_- Teil_3: Bestimmung von Größe und Durchfluss (ISO_21013-3:2016); Deutsche Fassung EN_ISO_21013-3:2016.* Berlin. DOI: 10.31030/2400392.

[129] Institut fuer Arbeitsschutz der Deutschen Gesetzlichen Unfallversicherung. *GESTIS-Stoffdatenbank.* 2022. URL: http://www.dguv.de/ifa/stoffdatenbank/ (visited on 12/15/2022).

[130] J. Tamson, M. Mair, and S. Grohmann. "Vapor-liquid equilibrium of the nitrogen-argon system at 100 K". In: *IOP Conference Series: Materials Science and Engineering* 1240.1 (2022), p. 012159. DOI: 10.1088/1757-899X/1240/1/012159.

[131] Jens Tamson and Steffen Grohmann. "Measurement of vapor pressure of neon from 25 K to 44 K". In: *Fluid Phase Equilibria* 565 (2023), p. 113621. ISSN: 03783812. DOI: 10.1016/j.fluid.2022.113621.

[132] International Organisation for Standardisation. *Evaluation of Measurement Data: Guide to the Expression of Uncertainty in Measurement (GUM)*. Geneva, Switzerland, 2008.

[133] Thomas Kochenburger. *Kryogene Gemischkaeltekreislaeufe fuer Hochtemperatursupraleiter-Anwendungen*. 1. Auflage. Verfahrenstechnik. München: Verlag Dr. Hut, 2019. ISBN: 978-3-8439-3987-4.

[134] G. Holst and L. Hamburger. "Untersuchungen über das Gleichgewicht von Flüssigkeit und Dampf des Systems Argon-Stickstoff". In: *Zeitschrift für Physikalische Chemie* 91U.1 (1916). ISSN: 0942-9352.

[135] V. G. Fastovskii, Yu V. Petrovskii, and V. I. Lenin. "Investigation of the argon + nitrogen liquid-and vapor-phase equilibrium. II". In: *Zhurnal Fiz. Khimii* 30 (1956).

[136] R. A. H. Pool et al. "Some excess thermodynamic functions for the liquid systems argon + oxygen, argon + nitrogen, nitrogen + oxygen, nitrogen + carbon monoxide, and argon + carbon monoxide". In: *Transactions of the Faraday Society* 58 (1962), p. 1692. ISSN: 0014-7672. DOI: 10.1039/TF9625801692.

[137] G. M. Wilson, P. M. Silverberg, and M. G. Zellner. "Argon-Oxygen-Nitrogen Three Component System Experimental Vapor-Liquid Equilibrium Data". In: *International Advances in Cryogenic Engineering* 10 (1965).

[138] G. B. Narinskii. "Liquid-Vapour Equilibrium in the Argon-Nitrogen system. I. Experimental Data and their Verification". In: *Russian Journal of Physical Chemistry* 40.9 (1966).

[139] F. B. Sprow and J. M. Prausnitz. "Vapor-Liquid equilibria for five cryogenic mixtures". In: *AIChE Journal* 12.4 (1966). ISSN: 0001-1541.

[140] P. L. Thorpe. "Liquid-vapour equilibrium of the system nitrogen + argon at pressures up to 10 atm". In: *Transactions of the Faraday Society* 64 (1968), p. 2273. ISSN: 0014-7672.

[141] D. R. Massengill and R. C. Miller. "Temperature dependence of excess volumes for simple liquid mixtures: N2 + Ar, N2 + Ar + CH4". In: *The Journal of Chemical Thermodynamics* 5.2 (1973). ISSN: 00219614.

[142] R. C. Miller, A. J. Kidnay, and M. J. Hiza. "Liquid-vapor equilibria at 112.00 K for systems containing nitrogen, argon, and methane". In: *AIChE Journal* 19.1 (1973). ISSN: 0001-1541.

[143] K.L Lewis and L.A.K Staveley. "Excess enthalpies of the liquid mixtures nitrogen + oxygen, nitrogen + argon, argon + ethane, and methane + carbon tetrafluoride". In: *The Journal of Chemical Thermodynamics* 7.9 (1975), pp. 855–864. ISSN: 00219614.

[144] I. M. Elshayal and B. C.-Y. Lu. "Measurement of total pressures for ethylene - propane mixtures". In: *The Canadian Journal of Chemical Engineering* 53.1 (1975), pp. 83–87. ISSN: 00084034. DOI: 10.1002/cjce.5450530114.

[145] Stanislaus-Gottfried J. Mastera. "Dampf-Flüssig-Gleichgewichtsdaten der Systeme Ar-N2, Kr-Ar, Kr-N2 und Xe-Kr sowie Löslichkeitsgrenzen des festen Xenons und des festen Kryptons in flüssigen Luftkomponenten". PhD thesis. Jülich: RWTH Aachen, 1977.

[146] J. Xiao and K. Liu. "Measurement and correlation of vapor-liquid equilibrium data in H2-N2-Ar system". In: *J. Chem. Eng.(China)* 8 (1990), pp. 8–12.

[147] M. J. Hiza, A. J. Kidnay, and W. M. Haynes. *Liquid-vapor equilibria in binary systems containing nitrogen, oxygen, and argon between 63 and 100 K: Preliminary unpublished results.* Boulder, CO, 1990.

[148] Zhangli Jin, Kunyuan Liu, and Wangwang Sheng. "Vapor-liquid equilibrium in binary and ternary mixtures of nitrogen, argon, and methane". In: *Journal of Chemical & Engineering Data* 38.3 (1993). ISSN: 0021-9568.

[149] A. Baba-Ahmed, P. Guilbot, and D. Richon. "New equipment using a static analytic method for the study of vapour–liquid equilibria at temperatures down to 77 K". In: *Fluid Phase Equilibria* 166.2 (1999), pp. 225–236. ISSN: 03783812. DOI: 10.1016/S0378-3812(99)00294-0.

[150] Johannes Gernert and Roland Span. "EOS–CG: A Helmholtz energy mixture model for humid gases and CCS mixtures". In: *The Journal of Chemical Thermodynamics* 93 (2016), pp. 274–293. ISSN: 00219614. DOI: 10.1016/j.jct.2015.05.015.

[151] Thol et al. "Unpublished Helmholtz Equation of State for Neon". In: (2018).

[152] R. Katti et al. "Thermodynamic Properties of Neon for Temperatures from the Triple Point to 700 K at Pressures to 700 MPa". In: *Advances in Cryogenic Engineering.* Ed. by R. W. Fast. Boston, MA: Springer US, 1986, pp. 1189–1197. ISBN: 978-1-4612-9299-9. DOI: 10.1007/978-1-4613-2213-9{\textunderscore}132.

[153] Jens Tamson, ed. *Personal Communication with Monika Thol.* 2022-07-26.

[154] R. M. Gibbons. "The equation of state of neon between 27 and 70 K". In: *Cryogenics* 9.4 (1969), pp. 251–260. ISSN: 00112275. DOI: 10.1016/0011-2275(69)90231-8.

[155] W. B. Streett and C. H. Jones. "Liquid Phase Separation and Liquid—Vapor Equilibrium in the System Neon—Hydrogen". In: *The Journal of Chemical Physics* 42.11 (1965), pp. 3989–3994. ISSN: 0021-9606. DOI: 10.1063/1.1695872.

[156] J. Ancsin. "Vapour Pressures and Triple Point of Neon and the Influence of Impurities on These Properties". In: *Metrologia* 14.1 (1978), pp. 1–7. ISSN: 0026-1394. DOI: 10.1088/0026-1394/14/1/002.

[157] Jacob Bigeleisen and Etienne Roth. "Vapor Pressures of the Neon Isotopes". In: *The Journal of Chemical Physics* 35.1 (1961), pp. 68–77. ISSN: 0021-9606. DOI: 10.1063/1.1731934.

[158] F. Henning and J. Otto. "Vapor-Pressure Curves and Triple Points in the Temperature Range from 14° to 90° Abs". In: *Physik Z* 37.18 (1936), p. 633.

[159] J. E. Verschaffelt. In: *Communs Phys. Lab. Univ. Leiden Suppl.* 64d (1928).

[160] C. A. Crommelin and R. O. Gibson. In: *Commun. Phys. Lab. Univ. Leiden* 185b (1927).

[161] C.A. Crommelin, J. Palacios, H. Kamerlingh Onnes. In: *Proc. Kon. Akad. Amsterdam* 27 (1919), p. 1316.

[162] P. G. Cath and H. K. Onnes. In: *Commun. Phys. Lab. Univ. Leiden* 152b (1917).

[163] N. Frank. "Messung des Dampf-Fluessiggleichgewichts von Helium-Neon-Gemischen". Bachelor's thesis. Karlsruhe, Germany: Karlsruhe Institute of Technology, 2023.

[164] P. H. van Konynenburg and R. L. Scott. *Critical lines and phase equilibria in binary van der Waals mixtures*. Vol. Vol. 2981980,1442. Philosophical transactions of the Royal Society of London A, Mathematical and physical sciences. London: Royal Society, 1980.

[165] P. Guilbot et al. "Rapid on-line sampler-injector: a reliable tool for HT-HP sampling and on-line GC analysis". In: *Analusis* 28.5 (2000), pp. 426–431. ISSN: 0365-4877. DOI: 10.1051/analusis:2000128.

A. Appendix

A.1. Uncertainty calculations according to GUM

In this section, the calculations of the pressure and temperature uncertainties are presented. They are based on [132]. In general, the expanded, combined uncertainty u_C is calculated from the Type A uncertainty u_A and Type B uncertainty u_B with a coverage factor of $k = 2$

$$u_C = k\sqrt{u_A^2 + u_B^2}, \text{ with} \tag{A.1}$$

$$u_A = \sqrt{\frac{1}{n(n-1)} \sum (x_i - \bar{x})}, \tag{A.2}$$

if at least 200 measurement points are recorded.

A.2. Uncertainty of pressure measurement

The pressure in the equilibrium cell is determined by the differential pressure (PDI40) to a secondary system, whose pressure is measured by the relative pressure sensors PI43 and PI42 or the absolute pressure sensor PI43. The ambient pressure p_{ambience} is measured by PI40. Thus, the equilibrium pressure is calculated by

$$p_{\text{equilibrium}} = p_i + p_{\text{ambience}} - p_{\text{PDI40}}, \text{ with } i = \{\text{PI42, PI43}\} \tag{A.3}$$

or

$$p_{\text{equilibrium}} = p_{\text{PI41}} - p_{\text{PDI40}}, \tag{A.4}$$

respectively. All pressure sensors but the differential pressures are calibrated by Druck Standards Laboratory. The stipulated uncertainties, which are listed in Table A.1, include repeatability, sensor uncertainties, the uncertainty of the calibration curve and electrical signal conversion with a coverage factor of $k_{\text{certificate}} = 2$. The uncertainty of the differential pressure sensor and of the ambient pressure sensor are negligible, as all stated combined uncertainties are rounded to ±1 mbar. Hence, the type B uncertainty of the equilibrium cell pressure is calculated by

$$u_B\left(p_{\text{equilibrium}}\right) = \frac{1}{k_{\text{certificate}}} u_B\left(p_i\right). \tag{A.5}$$

Table A.1.: Type B uncertainties of the individual sensors used for pressure measurement with coverage factor $k = 2$.

PI43		PI42		PI41		PI40	
p / bar(g)	$u(p)$ / ± bar	p / bar(g)	$u(p)$ / ± bar	p / bar(g)	$u(p)$ / ± bar	p / mbar(a)	$u(p)$ / ± mbar
0.000	0.0010	0.0000	0.00010	0.0000	0.00005		
-0.901	0.0010	-0.9007	0.00022	-0.9008	0.00010		
0.000	0.0010	0.0000	0.00010	-0.0001	0.00005		
0.000	0.0010	0.0000	0.00010	0.0000	0.00005	754.39	0.035
40.024	0.0019	14.0087	0.00058	2.0013	0.00008	895.03	0.041
80.046	0.0033	28.0169	0.00111	4.0025	0.00014	945.42	0.045
120.067	0.0048	42.0246	0.00165	6.0038	0.00022	995.90	0.046
200.111	0.0079	56.0334	0.00219	8.0052	0.00027	1045.05	0.048
160.087	0.0063	70.0417	0.00274	10.0064	0.00032	1145.85	0.052
120.059	0.0048	56.0341	0.00219	8.0054	0.00027	1045.05	0.048
80.037	0.0033	42.0260	0.00165	6.0042	0.00022	945.42	0.046
40.017	0.0019	28.0184	0.00111	4.0029	0.00016	895.03	0.043
-0.003	0.0005	14.0105	0.00058	2.0015	0.00012	754.39	0.041
		0.0005	0.00005	0.0001	0.00005		0.035

Table A.2.: Typical values for CERNOX®sensor uncertainties at selected temperatures with coverage factor $k = 2$.

T / K	$u_{\text{B,sensor}}(T)$ / mK	
	CX−1070	CX−1080
4.2	4	
10	4	
20	8	8
30	9	9
50	12	11
100	16	14
300	45	36

A.3. Uncertainty of temperature measurement

The temperature of the fluid (mixture) in the equilibrium cell is calculated as arithmetic mean of the two immersed temperature sensors {TI80, TI81}

$$T_{\text{equilibrium}} = \frac{T_{80} + T_{81}}{2}, \tag{A.6}$$

$$u\left(T_{\text{equilibrium}}\right) = k\frac{1}{\sqrt{2}}\sqrt{u^2(T_{80}) + u^2(T_{81})}. \tag{A.7}$$

Both uncertainties consist of the type A uncertainty related to repeated measurements and several contributions to the type B uncertainty, which are:

- the uncertainty of the temperature sensing element $u_{\text{B,sensor}}$,
- the uncertainty of the calibration curve $u_{\text{B,calibration}}$,
- the uncertainty of resistance measurement and data acquisition $u_{\text{B,resistance}}$ and
- the uncertainty induced by self-heating $u_{\text{B, self-heating}}$.

For the temperature measurement of the nitrogen-argon system, two CERNOX$^{®}$ sensors of band 1070 are used, while for the measurement of the vapor pressure of neon and the helium-neon system, band 1080 sensors are used. The respective sensor uncertainties are listed in Table A.2.

The discrete sensor calibration points are interpolated using step-wise defined Chebychev polynomials of type

$$T = \sum_i L_i \cdot \cos\left(i \cdot \arccos\left(\chi\right)\right), \tag{A.8}$$

with individual polynomial coefficients L_i and

$$\chi = \frac{(Z - Z_{\text{low}}) - (Z_{\text{up}} - Z)}{(Z_{\text{up}} - Z_{\text{low}})}, \tag{A.9}$$

Table A.3.: Chebychev polynomial coefficients for temperature sensors relevant to phase equilibrium determination.

Band	CX−1070		CX−1080	
T-range	24 K to 110 K		20 K to 95 K	
Serial No.	X144895	X144896	X166591	X166592
Order i		L_i		
0	64.303396	64.551111	53.520229	53.561482
1	-52.916365	-53.011959	-44.250390	-44.266985
2	11.092537	10.859157	10.322880	10.286012
3	-1.449658	-1.355140	-1.676987	-1.660558
4	0.123984	0.108038	0.217222	0.213431
5	-0.001839	-0.000741	-0.021577	-0.020761
6	0.001266	-0.001892	0.01216	0.001145
7	0	-0.001518	-0.00305	-0.000239
Z_{low}	2.41548614074	2.41306051749	3.15926393235	3.0991045601
Z_{up}	3.28199664886	3.2611467893	4.61400942615	4.50537017428
RMS	1.62 mK	1.58 mK	0.73 mK	0.96 mK

with $Z = \log(R_{\text{Ohm}})$ and $\{Z_{\text{low}}, Z_{\text{up}}\}$ the lower and upper thresholds of the stepwise defined function. The Chebychev parameters are listed in Table A.3. The root mean square of the interpolation deviations is used as $u_{\text{B,calibration}}$. The type B uncertainty of resistance measurement and data acquisition depends on the type B uncertainties of the data acquisition system, which are listed in Table A.4, and the sensitivity coefficients $\partial T / \partial R_{\text{Ohm}}$, which are calculated with the Chebychev polynomials

$$u_{\text{B,resistance}} = \frac{\partial T}{\partial R_{\text{Ohm}}} \cdot u_{\text{B}}(R_{\text{Ohm}}). \tag{A.10}$$

As per supplier information, self-heating is restricted to 1 mK when the excitation currents given in Table A.4 are used. Despite being systematic, it is considered as a random error source $u_{\text{B, self-heating}} = \pm 1$ mK within this uncertainty calculation. Finally, the respective sensor uncertainty $u(T_i)$ is given by

$$u(T_i) = \sqrt{u_{\text{A}}^2 + u_{\text{B,sensor}}^2 + u_{\text{B,calibration}}^2 + \left(\left(\frac{\partial T}{\partial R_{\text{Ohm}}}\right) u_{\text{B}}(R_{\text{Ohm}})\right)^2 + u_{\text{B, self-heating}}^2}. \tag{A.11}$$

A.4. Composition uncertainty for neon-helium mixtures

The measurement of composition requires a different GC calibration method than the one described in chapter 4. First, a carrier gas must be chosen, that has a different thermal conductivity than the mixture components to reach high sensitivity in the TCD. Due to

Table A.4.: Type B uncertainties of resistance measurement u_B (R_{Ohm}) of the Lakeshore model 224 temperature monitor with coverage factor $k = 2$.

Input range / Ω	Excitation current / μA	Electronic accuracy
0−100	100	±0.01 Ω ± 0.04% of rdg
0−300	30	±0.01 Ω ± 0.04% of rdg
0−1,000	10	±0.1 Ω ± 0.04% of rdg
0−3,000	3	±0.1 Ω ± 0.04% of rdg
0−10,000	1	±1.0 Ω ± 0.04% of rdg
0−30,000	0.3	±2.0 Ω ± 0.04% of rdg

constraints imposed by the available infrastructure and cost, hydrogen and nitrogen are the only candidates. For optimal sensor sensitivity, helium-rich samples would require hydrogen as carrier gas, while neon-rich require nitrogen. As the use of two different carrier gases is experimentally infeasible, hydrogen is chosen favoring vapor phase analyses. This choice of carrier gas limits the quantitative determination of the helium content to $x_1 \geq 0.03$.

Preliminary investigations on the GC set-up revealed that the GS Gaspro column has a small opposite separation effect on the neon-helium mixture compared to the molecular sieve column. Thus, the GS Gaspro column is bypassed for the study of this system. Also, an oven temperature of $-30\,°C$ is required to obtain a clear peak separation.

The gravimetric calibration method, which is used for the nitrogen-argon system, imposes additional uncertainty as helium is a very light-weight gas. Therefore, six certified calibration mixtures covering the whole composition range are used. The calibration mixtures are supplied by Air Liquide with a relative molar composition uncertainty of 2 % and a coverage factor of $k = 2$. Before the measurement campaign, the peak area ratios of all calibration mixtures are determined. Then, the sample taken from the equilibrium cell is diluted with hydrogen and its peak area ratio is measured. As illustrated in Figure A.1, the two calibration mixtures A and B, whose peak are ratios are closest to the one of the sample, are used to construct a 2-point calibration curve

$$Y_i = b_0 + b_1 X_i, \tag{A.12}$$

with $Y_i = (A_1/A_2)_i$ being the peak area ratio of components 1 and 2 of calibration mixture $i = \{A,B\}$, $X_i = (x_1/x_2)_i$ being the according composition ratio and $\{b_0, b_1\}$ the calibration parameters. Contrary to the 18-point calibration for the nitrogen-argon system, the calibration curve is not over-determined and the calibration parameters are calculated directly by

$$b_1 = \frac{\bar{Y}_A - \bar{Y}_B}{X_A - X_B}, \tag{A.13}$$

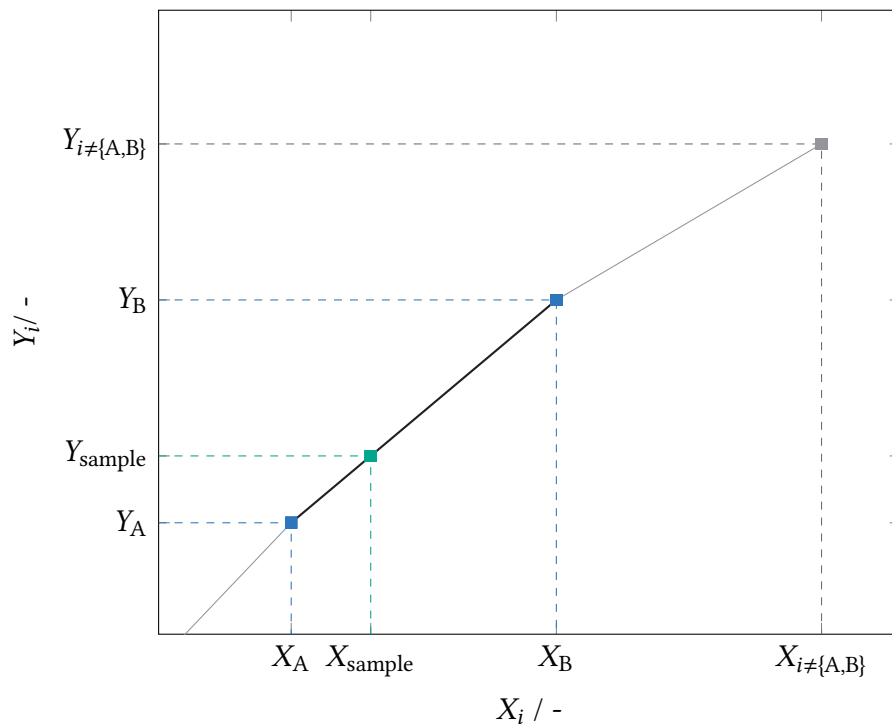$$b_0 = \frac{\bar{Y}_A + \bar{Y}_B}{2} - b_1 \frac{X_A + X_B}{2}. \tag{A.14}$$

Figure A.1.: Qualitative GC calibration curve for the composition analysis of helium-neon samples (green) using two adjacent calibration mixtures for a 2-point calibration (blue). Other calibration mixtures (gray) are not considered.

The uncertainties of the calibration parameters contain the type B uncertainties as stated in the calibration certificates and the type A uncertainty of the peak area ratios, which are measured 5 times. The molar composition of the sample is calculated by

$$x_{1,\text{sample}} = \frac{\bar{Y}_{\text{sample}} - b_0}{b_1 + \bar{Y}_{\text{sample}} - b_0} \tag{A.15}$$

with the uncertainty

$$u\left(x_{1,\text{sample}}\right) = k \cdot \left(\frac{b_1}{\bar{Y}_{\text{sample}} - b_0}\right)^2 \left[\left(\frac{u(b_0)}{b_1}\right)^2 + \left(\frac{\bar{Y}_{\text{sample}} - b_0}{b1^2}u(b_1)\right)^2 + \left(\frac{u(\bar{Y}_{\text{sample}})}{b_1}\right)^2\right.$$

$$\left. + 2\frac{\bar{Y}_{\text{sample}} - b_0}{b_1^3}u(b_0)u(b_1)r_{\text{cor}}(b_0, b_1)\right]^{\frac{1}{2}},$$

$$\tag{A.16}$$

with r_{cor} being the correlation coefficient and $u(\bar{Y}_{\text{sample}})$ being the type A uncertainty of five GC runs.

The reproducibility of the calibration curve is checked by re-measuring one of the calibration mixtures after each sample. The peak area ratios Y_i are updated when they differ more than 1 %. In this study, no updates were necessary.

Own publications

Peer-reviewed journal papers

Jens Tamson and Steffen Grohmann. "Measurement of vapor pressure of neon from 25 K to 44 K". in: *Fluid Phase Equilibria* 565 (2023), p. 113621. ISSN: 03783812. DOI: `10.1016/j.fluid.2022.113621`

Peer-reviewed conference papers

J. Tamson, M. Mair, and S. Grohmann. "Vapor-liquid equilibrium of the nitrogen-argon system at 100 K". in: *IOP Conference Series: Materials Science and Engineering* 1240.1 (2022), p. 012159. DOI: `10.1088/1757-899X/1240/1/012159`

J. Tamson, P. Blanck, and S. Grohmann. "Commissioning of the Cryogenic Phase Equilibria Test Stand CryoPHAEQTS". in: *IOP Conference Series: Materials Science and Engineering* 755.1 (2020), p. 012150. DOI: `10.1088/1757-899X/755/1/012150`

J. Tamson, M. Stamm, and S. Grohmann. "Set-up of the cryogenic phase equilibria test stand CryoPHAEQTS". in: *IOP Conference Series: Materials Science and Engineering* 502 (2019), p. 012087. DOI: `10.1088/1757-899X/502/1/012087`

Posters

Jens Tamson, Michael Stamm, and Steffen Grohmann. "Set-up of the cryogenic phase equilibria test stand CryoPHAEQTS". in: *27th International Cryogenic Engineering Conference (ICEC27-ICMC2018)*, Oxford, UK, 2018

Jens Tamson et al. "CryoPHAEQTS - Cryogenic phase equilibria test stand". in: *2nd International Workshop on Cooling Systems for HTS Applications*, Karlsruhe, Germany, 2017

Presentations

Jens Tamson and Steffen Grohmann. "Referenzmessungen am kryogenen Phasengleichgewichtsprüfstand CryoPHAEQTS". in: *DKV-Tagung*, Magdeburg, Germany, 2022

Jens Tamson and Steffen Grohmann. "New apparatus for the measurement of physical properties pf cryogenic fluids". in: *32nd European Symposium of Applied Thermodynamics (ESAT)*, Graz, Austria, 2022

Jens Tamson, Matthias Mair, and Steffen Grohmann. "Vapor-liquid equilibrium of the argon-nitrogen system at 100 K". in: *Cryogenic Engineering Conference and International Cryogenic Materials Conference (CEC-ICMC)*, Virtual conference, 2021

Jens Tamson, Philipp Blanck, and Steffen Grohmann. "Inbetriebnahme des Cryogenic Phase Equilibria Test Stand CryoPHAEQTS". in: *DKV-Tagung*, Ulm, Germany, 2019

Jens Tamson, Philipp Blanck, and Steffen Grohmann. "Commissioning of the cryogenic phase equilibria test stand CryoPHAEQTS". in: *Cryogenic Engineering Conference and International Cryogenic Materials Conference (CEC-ICMC)*, Hartford, USA, 2019

Jens Tamson, Michael Stamm, and Steffen Grohmann. "Aufbau des Cryogenic Phase Equilibria Test Stand". in: *DKV-Tagung*, Aachen, Germany, 2018